

# System Engineering Analyses for the Study of Future Multispectral Land Imaging Satellite Sensors for Vegetation Monitoring

by

Zhaoyu Cui

B.S. Harbin Institute of Technology, 2011

M.S. Harbin Institute of Technology, 2013

A dissertation submitted in partial fulfillment of the  
requirements for the degree of Doctor of Philosophy  
in the Chester F. Carlson Center for Imaging Science

College of Science

Rochester Institute of Technology

December, 2018

Signature of the Author \_\_\_\_\_

Accepted by \_\_\_\_\_  
Coordinator, Ph.D. Degree Program Date

CHESTER F. CARLSON CENTER FOR IMAGING SCIENCE  
COLLEGE OF SCIENCE  
ROCHESTER INSTITUTE OF TECHNOLOGY  
ROCHESTER, NEW YORK

CERTIFICATE OF APPROVAL

---

Ph.D. DEGREE DISSERTATION

---

The Ph.D. Degree Dissertation of Zhaoyu Cui  
has been examined and approved by the  
dissertation committee as satisfactory for the  
dissertation required for the  
Ph.D. degree in Imaging Science

\_\_\_\_\_  
Dr. John Kerekes, Dissertation Advisor Date

\_\_\_\_\_  
Dr. David Ross, External Chair Date

\_\_\_\_\_  
Dr. Emmett Ientilucci Date

\_\_\_\_\_  
Dr. Carl Salvaggio Date

# System Engineering Analyses for the Study of Future Multispectral Land Imaging Satellite Sensors for Vegetation Monitoring

by  
Zhaoyu Cui

Submitted to the  
Chester F. Carlson Center for Imaging Science  
in partial fulfillment of the requirements  
for the Doctor of Philosophy Degree  
at the Rochester Institute of Technology

## Abstract

Vegetation monitoring is one of the key applications of earth observing systems. Landsat data have spatial resolution of 30 meters, moderate temporal coverage, and reasonable spectral sampling to capture key vegetation features. These characteristics of Landsat make it a good candidate for generating vegetation monitoring products. Recently, the next satellite in the Landsat series has been under consideration and different concepts have been proposed. In this research, we studied the impact on vegetation monitoring of two proposed potential design concepts: a wider field-of-view (FOV) instrument and the addition of red-edge spectral band(s). Three aspects were studied in this thesis:

First, inspired by the potential wider FOV design, the impacts of a detector relative spectral response (RSR) central wavelength shift effect at high angles of incidence (AOI) on the radiance signal were studied and quantified. Results indicate: 1) the RSR shift effect is band-dependent and more significant in the green, red and SWIR 2 bands; 2) At high AOI, the impact of the RSR shift effect will exceed sensor noise specifications in all bands except the SWIR 1 band; and 3) The RSR shift will cause SWIR2 band more to be sensitive to atmospheric conditions.

Second, also inspired by the potential wider FOV design, the impacts of the potential new wider angular observations on vegetation monitoring scientific products were studied. Both crop classification and biophysical quantity retrieval applications were studied

using the simulation code DIRSIG and the canopy radiative transfer model PROSAIL. It should be noted that the RSR shift effect was also considered. Results show that for single view observation based analysis, the higher view angular observations have limited influence on both applications. However, for situations where two different angular observations are available potentially from two platforms, up to 4% improvement for crop classification and 2.9% improvement for leaf chlorophyll content retrieval were found.

Third, to quantify the benefits of a potential new design with red-edge band(s), the impact of adding red-edge spectral band(s) in future Landsat instruments on agroecosystem leaf area index (LAI) and canopy chlorophyll content (CCC) retrieval were studied using a real dataset. Three major retrieval approaches were tested, results show that a potential new spectral band located between the Landsat-8 Operational Land Imager (OLI) red and NIR bands slightly improved the retrieval accuracy (LAI:  $R^2$  of 0.787 vs. 0.810 for empirical vegetation index regression approach, 0.806 vs. 0.828 for look-up-table inversion approach, and 0.925 vs. 0.933 for machine learning approach; CCC:  $R^2$  of 0.853 vs. 0.875 for empirical vegetation index regression approach, 0.500 vs. 0.570 for look-up-table inversion approach, and 0.854 vs. 0.887 for machine learning approach).

In general, for the potential wider FOV design, the RSR shift effect was found to cause noticeable radiance signal difference that is higher than detector noise in all OLI bands except SWIR1 band, which is not observed in the current OLI design with its 15 degree FOV. Also both the new wider angular observations and potential red-edge band(s) were found to slightly improve the vegetation monitoring product accuracy. In the future, the RSR shift effect in other optical designs should be evaluated since this study assumed the angle reaching the filter array is the same as the angle reaching the sensor. In addition to improve the accuracy of the off angle imaging study, a 3D vegetation geometry model should be explored for vegetation monitoring related studies instead of the 2D PROSAIL model used in this thesis.



## Acknowledgements

It has been long time since I began pursuing PhD degree at RIT. Today I still remember the details of my first day in RIT campus. Since then the experience here was splendid. This dissertation is a milestone of my past over five years. Though I am the author of this dissertation, this work belongs to many others.

First of all, I would like to appreciate my advisor Dr. John Kerekes, who guided and supported me throughout my entire stay at Center for Imageing Science. Dr. Kerekes's deep knowledge and broad perspective in remote sensing field, patient and skillful guidance, and excellent time management skills helped me reaching this point. Besides, Dr. Kerekes is a great life mentor and helped me got adapted to the life in the U.S.

My appreciation also goes to my thesis committee members: Dr. Emmett Ientilucci, Dr. Carl Savalggio, and Dr. David Ross. Their inspiring comments and suggestions made the thesis more accomplished. I am grateful to all my committee members for being so supportive.

I would like to recognize the faculty, staff and senior students in Center for Imaging Science. Dr. Rolando Raqueno, Dr. Adam Goodenough and Dr. Scott Brown were always ready to help me set up the DIRSIG simulations. Dr. Wei Yao and Dr. Rajagopalan Rengarajan answered a lot practical simulation questions from me. The experiments in the thesis can not be done without their support. Besides, I am grateful to Dr. John Schott, Dr. Aaron Gerace, Dr. Matthew Montanaro and Dr. Donald McKeown for their rich experience in Landsat projects. I also would like to thank Beth Lockwood, Colleen McMahon, Sue Chan, Joyce French and of course Cindy Schultz, for their meticulous and considerate supports.

In addition, I would like to appreciate NASA for funding this work. Besides, I would like to thank Dr. Brian Markham, Dr. Phil Dabney and Dr. Julia Barsi from NASA. They not only provided me the Landsat data archives, but also gave me comments from the engineering perspective. My special thank goes to Dr. Jochem Verrelst for generously sharing the SPARC '03 field campaign dataset with me.

Lots of thanks go to my friends and roommates: Fu Jiang, Dong Wang, Xuwen Zhang, Chao Zhang, Chi Zhang, Runchen Zhao, Wei Yao, Utsav Gewali, Kamran Bianee,

Can Jin, Fan Wang and all my classmates. It is my great pleasure to meet them here. We had a lot good time and fun together.

Finally, a very grateful appreciation goes to my parents, Zhigang Cui and Xiulian Niu, and my girlfriend Xiaojiao Liu. Their understanding and positive attitude are the greatest spiritual support for me to finish the thesis, and will be the treasure for the rest of my life.

# Contents

<b>1</b>	<b>Introduction</b>	<b>1</b>
<b>2</b>	<b>Objectives</b>	<b>4</b>
2.1	Objectives . . . . .	4
2.2	Tasks . . . . .	5
2.2.1	Impact of RSR central wavelength shift at high AOI in both Landsat 8 OLI and future Landsat instrument with wider FOV . . . . .	5
2.2.2	Impact of wider FOV design of future Landsat instrument on veg- etation monitoring scientific products . . . . .	5
2.2.3	Study the impact of adding red-edge spectral band(s) in future Landsat instrument on agriculture canopy variable retrieval . . . .	6
<b>3</b>	<b>Previous Work</b>	<b>7</b>
3.1	Impact of RSR Shift Effect . . . . .	7
3.2	Impact of Instrument Angular Aspects on Vegetation Monitoring . . . . .	9
3.3	Significance of red-edge spectral band for vegetation biophysical variable retrieval . . . . .	11
3.4	Summary . . . . .	14
<b>4</b>	<b>Background and Analysis Tools</b>	<b>15</b>
4.1	Radiometry . . . . .	15

---

4.1.1	Basic Radiometry . . . . .	16
4.1.2	BRDF . . . . .	17
4.1.3	RSR . . . . .	21
4.2	Landsat 8 OLI Characteristics . . . . .	21
4.2.1	OLI RSR . . . . .	21
4.2.2	OLI SNR . . . . .	24
4.3	RSR Shift Effect . . . . .	24
4.4	Vegetation Monitoring . . . . .	26
4.4.1	Crop mapping . . . . .	26
4.4.2	Crop Parameter Retrieval . . . . .	31
4.5	DIRSIG . . . . .	35
4.6	PROSAIL . . . . .	37
4.7	Factorial Analysis . . . . .	41
4.8	Summary . . . . .	43
<b>5</b>	<b>RSR Shift Effect Impacting on Radiance Signal</b>	<b>44</b>
5.1	Methodology . . . . .	44
5.1.1	View Zenith Angle Determination . . . . .	45
5.1.2	RSR Shift Model . . . . .	46
5.1.3	DIRSIG Configuration . . . . .	47
5.1.4	Radiance Noise Model . . . . .	52
5.2	Result . . . . .	53
5.2.1	DIRSIG Output Analysis . . . . .	54
5.2.2	Qualitative Analysis of the RSR Shift Effect . . . . .	56
5.2.3	Quantitative Analysis of RSR Shifts Contribution to At-detector Radiance Variation . . . . .	60
5.2.4	RSR Shift Effect For Various Atmospheres . . . . .	63
5.2.5	RSR Shift Effect Versus Noise . . . . .	65
5.2.6	RSR Shift Effect Compared to NDVI . . . . .	67

---

5.3	Summary . . . . .	70
<b>6</b>	<b>Impact of Wider Field-of-view Instrument on Vegetation Monitoring Scientific Products</b>	<b>72</b>
6.1	Methodology . . . . .	73
6.1.1	PROSAIL Sensitivity Study . . . . .	73
6.1.2	BRF Noise Model . . . . .	75
6.1.3	Crop Classification . . . . .	76
6.1.4	Canopy Biophysical Quantity Retrieval . . . . .	78
6.2	Results . . . . .	79
6.2.1	Example of Simulated Data . . . . .	79
6.2.2	Crop Mapping . . . . .	83
6.2.3	Crop Canopy Biophysical Quantity Retrieval . . . . .	86
6.3	Summary . . . . .	87
<b>7</b>	<b>Potential of Red-edge Spectral Band in Future Landsat Satellites on Agroecosystem Vegetation Canopy Variable Retrieval</b>	<b>89</b>
7.1	Dataset and Preprocessing . . . . .	90
7.1.1	SPARC '03 dataset . . . . .	90
7.1.2	Data Pre-processing . . . . .	92
7.2	Methodology . . . . .	93
7.2.1	Empirical Vegetation Index Regression Approach . . . . .	93
7.2.2	Support Vector Regression Approach . . . . .	95
7.2.3	Look-up-table Inversion Approach . . . . .	96
7.3	Leaf Area Index Retrieval Results . . . . .	97
7.3.1	Empirical Vegetation Index Regression Approach Result . . . . .	97
7.3.2	LUT Inversion Approach Result . . . . .	100
7.3.3	Support Vector Regression Approach Result . . . . .	103
7.3.4	Discussion . . . . .	105
7.4	Canopy Chlorophyll Content Retrieval Results . . . . .	107

7.4.1	Empirical Vegetation Index Regression Approach Result . . . . .	107
7.4.2	LUT Inversion Approach Result . . . . .	107
7.4.3	Support Vector Regression Approach Result . . . . .	109
7.4.4	Discussion . . . . .	110
7.5	Summary . . . . .	115
<b>8</b>	<b>Summary and Outlook</b>	<b>116</b>
8.1	Conclusions . . . . .	116
8.2	Contributions . . . . .	118
8.3	Outlook and future work . . . . .	119

# List of Figures

1.1	Landsat mission satellites timeline [4]. . . . .	2
3.1	Spectral band settings of Sentinel-2, Landsat-8 and Landsat-7 [37]. . . . .	13
4.1	Illustration of different radiative transfer path [1]. . . . .	16
4.2	Typical surface directional reflectance characteristics [1]. . . . .	18
4.3	Illustration of geometry of BRDF definition [1]. . . . .	19
4.4	The complete OLI focal plane [12]. . . . .	22
4.5	OLI RSRs. . . . .	23
4.6	OLI NIR band RSR non-uniformity between different FPMs [11]. . . . .	23
4.7	Two distinct filter spectra emerge for s- and p-polarized light as AOI increases [49]. . . . .	25
4.8	Example of canopy leaf chlorophyll retrieval using four different VIs [33].	32
4.9	Summary of several algorithms used operationally to retrieve canopy biophysical variables [56]. . . . .	33
4.10	Schematic representation of the PROSPECT+SAIL canopy reflectance model [72]. . . . .	38
4.11	Plate model and multi-layer model of leaf structure [73]. . . . .	38
4.12	Measured (left) and simulated (right) reflectance spectra for maize obtained by CHRIS for 5 observation angles. Date 3 Aug. 2003, solar zenith: 32, relative azimuth: 146.3 (forward looking), 33.7 (backward looking). . .	40

5.1	Candidate sun-synchronized orbits with no more than 10 days repeat cycle [75]. . . . .	45
5.2	RSR shift with respect to AOL. . . . .	47
5.3	Scene and focal plane geometric layout used in the DIRSIG simulation. . .	48
5.4	Landsat 8 OLI RSR profiles and reflectance spectrum of deciduous forest canopy. . . . .	50
5.5	Example forest canopy BRDF plot used in simulation [40]. . . . .	51
5.6	Predicted (curves) and measured (points) OLI SNR performance. . . . .	53
5.7	Noise added, noise free and smoothed at detector spectral radiance profiles. .	55
5.8	Simulated at detector spectral radiance profiles of all bands. In each figure, four profiles are the combinations of two surface types (Lambertian or BRDF) with two RSR types (ideal uniform or shifted) . . . . .	57
5.9	Cross track profiles of at detector BRF and at detector spectral radiance (BRDF surface only). Blue is ideal uniform RSR and red is shifted RSR. . .	59
5.10	OLI RSR and ground reaching spectral irradiance. . . . .	61
5.11	Spectral radiance difference profiles of SWIR 2 band under different atmospheric conditions. . . . .	64
5.12	RSR shift effect versus noise. For each figure, blue profile is at detector spectral radiance difference due to RSR shift only; red profile is noise limit. .	66
5.14	Compensation of NDVI affected by deterministic RSR shift effect in mls atmosphere. . . . .	69
6.1	Input variables sensitivity to the PROSAIL model (1nm spectral resolution). .	74
6.2	Input variables sensitivity to the PROSAIL model (within OLI bands). . .	74
6.3	Workflow of single VZN observations based crop mapping. . . . .	77
6.4	Workflow of two VZN observations based crop mapping. . . . .	78
6.5	Workflow of crop canopy biophysical parameter retrieval. . . . .	80
6.6	Angular variation of the PROSAIL model generated BRF spectra. . . . .	81
6.7	BRF spectra libraries generated using PROSAIL. . . . .	82



6.8	Examples of DIRSIG generated at-detector radiance signal. . . . .	83
6.9	Crop classification accuracy using single VZN observations (LDA, kNN, SVM and DT). . . . .	84
6.10	Crop classification accuracy improvement (%) using two VZN observation over single VZN observation based accuracy. . . . .	85
6.11	Leaf chlorophyll retrieval performance using single VZN observations (LUT inversion and SVR). . . . .	86
6.12	Leaf chlorophyll retrieval performance improvement (RMSE) using two VZN observation over single VZN observation based accuracy (LUT inversion and SVR). . . . .	87
7.1	SPARC field campaign land use map and sampling points [89]. . . . .	91
7.2	The geometry configuration of SPARC '03 campaign data collection [89]. .	91
7.3	Example HyMap RGB images along different flight lines [89]. . . . .	92
7.4	Spectral bands studied in this work (OLI bands and potential red edge bands) and typical agriculture spectral reflectance. . . . .	93
7.5	The relationship between GBVI and LAI for all 118 SPARC '03 dataset ESU samples. . . . .	94
7.6	The 98 SPARC 03 campaign HyMap spectra used in our study. . . . .	94
7.7	Result of VI ( $NDVI_{a-b}$ ) regression approach. . . . .	99
7.8	Result of VI ( $CI_{a-b}$ ) regression approach. . . . .	101
7.9	Statistics of top 10% performance of adding 0/1 new bands in LUT inversion approach. . . . .	102
7.10	Statistics of top 10% performing cases of adding 0/1/2/3 new bands in LUT inversion approach. . . . .	103
7.11	Statistics of top 10% performance of adding 0/1 new bands in SVR approach.	104
7.12	Result of VI ( $CI_{a-b}$ ) regression approach for CCC. . . . .	108
7.13	Statistics of top 10% performing cases of adding 0/1 new bands in SVR approach. . . . .	109

7.14	Statistics of top 10% performance of adding 0/1 new bands in SVR approach.	110
7.15	SPARC '03 dataset ground truth variables distribution. . . . .	113
7.16	SPARC '03 dataset ground truth variables co-distribution. . . . .	114

# List of Tables

4.1	Landsat 8 OLI spectral band characteristics. . . . .	22
4.2	OLI pre-launch measured SNR performance for different signal level. . . .	24
4.3	Landsat 8 OLI effective refractive index ( $n^*$ ) of filters for each band. . . .	26
4.4	Main variables of PROSAIL [70]. . . . .	40
4.5	Table treatment code of $2^3$ design [74]. . . . .	42
5.1	Candidate sun-synchorized orbits with no more than 10 days repeat cycle.	46
5.2	Mean radiance, standard deviation of mean-subtracted residual, and noise level for each band. . . . .	55
5.3	Correlation coefficient between uniform RSR and shifted RSR signals (BRF and at detector radiance). . . . .	58
5.4	Contribution of three factors on at detector radiance variation. . . . .	62
5.5	Maximum at detector spectral radiance difference due to RSR shift for three atmosphere conditions (future Landsat, max AOI = 15 degrees). . . .	64
5.6	Maximum at detector spectral radiance difference due to RSR shift for three atmosphere conditions (Landsat 8 OLI, max AOI = 3.5 degrees). . . .	64
5.7	Noise level and pixel number/AOI threshold where deterministic RSR shift effect exceeds the noise. . . . .	67
5.8	NDVI regression coefficients for different atmospheric conditions. . . . .	70

6.1	PROSAIL input variable distribution for crop classification and crop parameter retrieval tasks [60]. . . . .	75
6.2	Surface reflectance noise model mean and standard deviation of six OLI bands studied (expressed in $10^{-3}$ reflectance). . . . .	76
7.1	Range and distribution of input parameters used to drive PROSAIL model to generate LUT. . . . .	97
7.2	Number of possible band combinations for adding 0/1/2/3 new potential bands. . . . .	102
7.3	LAI retrieval performance and optimal new band center position range of three retrieval approaches. . . . .	105
7.4	CCC retrieval performance and optimal new band center position range of three retrieval approaches. . . . .	110

# Chapter 1

## Introduction

Remote sensing is the field of study associated with extracting information about an object without physical contact with it [1]. Passive remote sensing collects the radiation that is emitted or reflected by the target or surrounding areas. Active remote sensing emits energy to scan the targets and detects the reflected radiation. Remote sensing have been used in numerous areas, including geography, land surveying, military, commercial, and planning applications. Vegetation monitoring is one of the key applications of remote sensing satellites. Since field campaigns are expensive and time consuming, remote sensing satellite can provide the observations over agricultural land periodically. Satellite remote sensing data can be used to estimate the variety, class and area of vegetation for land planning, within multiple scale of ranges.

Currently, several remote sensing satellites such as MODIS [2] and MERIS [3] provide vegetation monitoring products using their multi-temporal and multi-angular observations. However, these products have relatively coarse spatial resolution, which makes them less accurate for precise crop yield prediction or local scale forest monitoring. A higher spatial resolution vegetation product would be desirable. Landsat data have a spatial resolution of 30 meters, moderate temporal coverage, and reasonable spectral sampling to capture the vegetation features. These features of Landsat make it a good candidate for generating moderate spatial resolution vegetation products.

Since the launch of the first Earth Resources Technology Satellite ERTS 1 (later re-named Landsat 1) in 1972, the Landsat series of satellites have monitored the Earth's surface for over forty years. Its imagery collection acquired over the past four decades provides a unique resource for agriculture, forestry, mapping, and global change research. Currently both Landsat 7 and Landsat 8 continue to acquire data from a sun-synchronous orbit with an altitude of 705km, a 15-day revisit rate and a swath width of 185km, which corresponds to 15 degree field of view (FOV) [4].

The timeline of all Landsat mission satellites is as shown in Figure 1.1 [4].

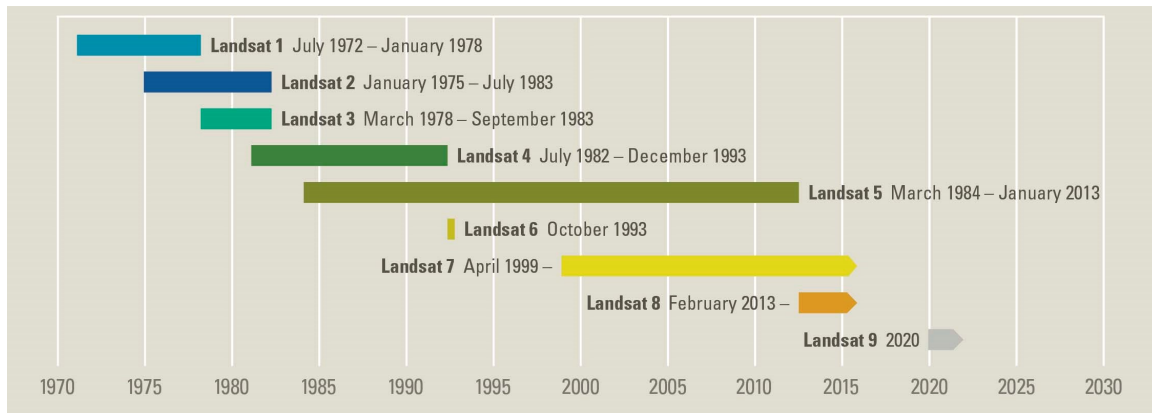


Figure 1.1: Landsat mission satellites timeline [4].

The next satellite in the series, Landsat 9, is currently in production planned for launch in 2020 and will be a near duplicate of Landsat 8. Beyond that, NASA is exploring alternative approaches to continue the data continuity of the Landsat program. Different potential instrument design concepts have been proposed so far. One of them is to expand the FOV with a larger ground swath, which would provide the potential for increased view angle diversity in the data and higher revisit rate. Another potential design is the addition of red-edge band(s). The red-edge is the sharp change in leaf reflectance between 680 and 750 nm [5] and is a key wavelength range in remote sensing that is sensitive to vegetation conditions.

This thesis was motivated by the above mentioned potential future Landsat instru-

ment designs. The goal of this research is to study the trade-off of the potential future Landsat instrument system engineering concepts including wider FOV and addition of red-edge band(s). More specifically, the objectives are to quantify their impacts on radiance signal and impacts on vegetation monitoring products accuracy. The structure of this thesis is: Chapter 1 is the introduction. Chapter 2 projects the detailed objectives and tasks of the thesis. Chapter 3 reviews the related previous work. Chapter 4 describes the background information and analysis tools used in this work. The study of the impact of wider FOV design on radiance signal, the study of the impact of wider FOV design on vegetation monitoring products, the study of the impact of addition of red-edge on agroecosystem canopy variable retrieval are in Chapter 5, 6 and 7, respectively. The conclusions, contributions and future work are presented in Chapter 8.

# Chapter 2

## Objectives

As discussed in Chapter 1, this research is to study the potential of the future Landsat instrument system engineering concepts, including the impact of wider FOV design on spectral radiance signal, the impact of wider FOV design on vegetation monitoring scientific products, and the impact of adding red-edge spectral band on agroecosystem canopy variable retrieval.

To answer these questions, the overall objective of this thesis is to develop a framework by integrating models to study the end-to-end radiance signal sensitivity and scientific product accuracy sensitivity to future Landsat instrument design changes. Specifically, the detailed objectives and the corresponding tasks of the thesis are covered in this chapter.

### 2.1 Objectives

The specific objectives in this thesis are:

- 1) Study the impact of relative spectral response (RSR) central wavelength shift effect at high angle of incidence (AOI) in both Landsat 8 OLI and future Landsat instrument with wider field-of-view (FOV).



2) Study the impact of wider FOV design of future Landsat instrument on vegetation monitoring scientific products.

3) Study the impact of adding red-edge spectral band(s) in future Landsat instrument on agriculture canopy variable retrieval.

## **2.2 Tasks**

### **2.2.1 Impact of RSR central wavelength shift at high AOI in both Landsat 8 OLI and future Landsat instrument with wider FOV**

It is a known characteristic of multilayer dielectric filters that the center wavelength of the bandpass will shift at high AOIs. This could lead to a variation of the signal measured across the swath with a complicated interplay between the filter response, the atmosphere, and the surface reflectance spectra. These effects have motivated the research to quantify the impact on measured radiances due to shifts in the spectral bandpasses of OLI on Landsat 8 and 9 as well as future instrument concepts. This task has been done in simulation approach, and the specific steps included:

- Model the RSR shift with respect to AOI
- Model the radiance signal noise
- Quantify the significance of RSR shift in each band
- Quantify the significance of RSR shift for various atmosphere models
- Quantify the significance of RSR shift versus noise

### **2.2.2 Impact of wider FOV design of future Landsat instrument on vegetation monitoring scientific products**

The potential wider FOV design will introduce new angular observations, comparing to previous Landsat instruments. This section is to quantify the potential impact of a wider FOV future Landsat instrument on vegetation monitoring at scientific product level. Two

aspects will be studied. First, the research investigated if the wider angular observations would affect application performance compared to the existing more narrow FOV instruments. Second, the research studied if the new angular observations would provide a benefit from a combination with data from OLI or another future Landsat satellite. Two important applications, crop classification and vegetation biophysical variable retrieval, were investigated in this study. Both crop canopy radiative transfer model (RTM) and radiance propagation models were used. The detail steps included:

- Model the angular variant vegetation canopy reflectance
- Model the reflectance level noise
- Quantify the impact of larger AOI observations on crop mapping and canopy parameter retrieval tasks
- Quantify the impact of combination of cross sensor observations on crop mapping and canopy parameter retrieval tasks

### **2.2.3 Study the impact of adding red-edge spectral band(s) in future Landsat instrument on agriculture canopy variable retrieval**

The potential of adding red-edge spectral band in future Landsat instrument will improve the performance of vegetation related products. In this section, the impact of adding one, two, or three red-edge spectral bands in future Landsat instrument on canopy biophysical parameter retrieval applications were studied, with real field campaign data. Different red-edge spectral band candidates were considered, the performance improvements and the optimal red-edge band position were studied. The steps included:

- Pre-process the field campaign data
- Quantify the performance improvement and locate the optimal potential red-edge spectral band position for canopy leaf area index retrieval
- Quantify the performance improvement and locate the optimal potential red-edge spectral band position for canopy chlorophyll content retrieval

# Chapter 3

## Previous Work

This section briefly reviews the previous efforts related to the tasks of this thesis, and the gaps that can be filled by this thesis.

### 3.1 Impact of RSR Shift Effect

As far as we know, since most of the wide FOV satellite instruments use whiskbroom scanners, there have been very little research focusing on studying the RSR shift effect in pushbroom scanner like OLI. However, some research has been done to study the impact of cross-sensor RSR variation on both radiance signal and scientific product level. Their topics included the RSR variation impact on vegetation monitoring products like NDVI [6][7][8], cross-sensor radiometric calibration for temporal studies [9] [10], and within-sensor RSR non-uniformity studies [11] [12]. They are briefly reviewed here:

Radiometrically calibrated data have been an important aspect of Landsat data continuity [13]. Accurate radiometric calibration has been observed to be an essential step in providing high quality quantitative remote sensing data [14]. Since many Landsat studies are focused on monitoring earth surface parameters over long periods of time, harmonizing the data from multiple different instruments onto a common radiometric

scale is necessary. A variety of methods have been developed that include pre-launch lab based calibrations and post-launch on-orbit calibration.

Since vegetation is one of the most common land surface biomes, previous research on the effects of spectral response variation have studied the effects on monitoring vegetation temporal changes. Teillet, et al, studied the impact of changes in spectral bandwidth and spatial scale on forest NDVI [15]. They concluded that NDVI is more sensitive to the spectral location of the red band than that of the near infrared (NIR) band. Trishchenko, et al, studied the effect of different system RSR functions on the measurement of surface reflectance and NDVI with moderate resolution satellite sensors [7]. Franke, et al, and Gonsamo, et al, performed similar studies on spectral response function impacts. Franke, et al, considered three sensors [16] while Gonsamo, et al, considered twenty-one different sensors [8]. Both studies confirmed that vegetation monitoring, especially as measured by NDVI, is affected by RSR variation and should not be ignored.

Additional studies have focused on cross sensor calibration and data continuity analysis. Van Leeuwen et al, Teillet et al and D'Odorico et al all studied radiometric cross-calibration between different sensors with a goal of time series continuity [9][17][10]. They presented regression models to radiometrically intercalibrate sensors data. In particular, some studies have focused on Landsat sensor cross calibration. Teillet, et al, studied Landsat-7 ETM+ and Landsat-5 TM sensor cross calibration [6]. Mishra studied the inter calibration between Landsat-7 ETM+ and Landsat-8 [18]. The majority of the above mentioned studies were done using a data simulation approach; they combined ground material reflectance spectra (from a field or laboratory measurement library or from a first principles simulation tool), atmospheric radiative transfer model and different sensors RSRs to simulate the top of atmosphere (TOA) spectral radiance or reflectance.

Lastly, Barsi et al studied the RSR uniformity of Landsat-8 OLI including in-band response, out-of-band response and spectral uniformity across the focal plane [12][11]. They concluded that for Landsat-8 OLI, the maximum at detector radiance discontinuity

due to focal plane module (FPM) variations for all bands was 0.19%, which occurred when the sensor was observing vegetation.

For the potential future Landsat instrument with wider FOV design, concerns have been raised that whether the detector RSR shift effect would negatively impact the radiance signal when the instrument is observing the vegetation. This is an open area and no previous studies can answer that. The gap can be filled in this thesis.

### **3.2 Impact of Instrument Angular Aspects on Vegetation Monitoring**

The impacts of angular aspects on vegetation monitoring have been studied in a lot previous works. Barnsley et al.[19] explored the potential of CHRIS instrument on board of PROBA satellite for estimating canopy biophysical parameters from space by means of a LUT-based Bidirectional reflectance distribution factor (BRDF) model inversion scheme. They simulated reflectance data with spectral (18 bands ranging from 410nm to 1050nm) and directional (at-ground zenith angles of  $0^\circ$ ,  $\pm 15^\circ$ ,  $\pm 30^\circ$ ,  $\pm 45^\circ$ ,  $\pm 60^\circ$ ) sampling characteristics of the CHRIS/PROBA satellite sensor. The results showed that the inversion was robust to random noise up to 0.1 reflectance unit and sensitive to variations in the angular sampling. The inversion using the combination of two weeks observations achieved high degree of accuracy with errors of only a few percent for most parameters. And the retrieval accuracy varied as a function of time of year and latitude.

Leroy et al. [20] studied the improvements expected from POLDER. POLDER has a FOV of  $\pm 43$  degrees in along track direction and  $\pm 51$  degrees in cross track direction. A surface target was viewed up to 14 times during the satellite overpassed with various viewing angles. This is beneficial for both surface reflectance estimation and atmospheric compensation. Taking advantage of the directional signatures captured by POLDER, new vegetation indices were designed and the optimal viewing directions were decided. Also, the LUT based vegetation biophysical parameter inversion were tested. The authors

found two specific directions that the POLDER instrument is well adapted to: the hot spot direction and the specular direction of the BRDF.

Lucht [21] studied the expected accuracies of Bidirectional reflectance factor (BRF) and albedo retrieved from the angular samples provided by the upcoming MODIS and MISR instruments in simulation approach using different BRDF models. Results showed that albedo can be retrieved with 2% to 8% median accuracy using either the Ambrals or the modified RPV model for any solar zenith angle for any MODIS/MISR sampling. And the accuracy of predicted nadir view reflectance was also mostly within 10% error margin.

In application level, Verrelst et al [22] studied the angular sensitivities of different vegetation indices (VIs) using CHRIS/PROBA data. They studied different broadband and narrowband VIs sensitivity to angular variation. They found most widely used VIs have significant angular sensitivities. They also concluded the VIs angular sensitivity varies between homogeneous vegetation such as grass and heterogeneous vegetation such as forest. Breunig et al [23] studied the directional effects of NDVI with MODIS data. They found a trend of higher reflectance in back scattering direction due to more sunlit. They also found a trend of higher NDVI value in forward scattering direction due to stronger shadow effects in the red band. Galvao et al [24] studied the impact of view angle effects on soybean varieties discrimination with Hyperion data. They found that the discrimination with back scattering direction observations achieved the highest classification accuracy. This was verified by Xavier [25] et al. They found forest types are most discriminative at back scattering direction (26.1 degrees in MISR data they used). For canopy biophysical parameter retrieval applications, Weiss et al [26] studied the optimal sampling directions for vegetation canopy LAI, chlorophyll, and fraction of photosynthetically active radiation absorbed (fAPAR) retrievals. They concluded that less than six directions observations are enough for retrieving the interested parameters. The observations from the other directions are redundant. They also concluded that the hot spot direction is the most important direction for LAI retrieval.

Besides, with simulated datasets [27] [28] or field measured datasets [29], some

research have been done to study the potential of vegetation biophysical parameter and surface reflectance retrieval with multiple directional satellite observations.

The above mentioned previous angular aspect studies are helpful for potential wider FOV future Landsat instrument design. However, specific studies with Landsat spectral band settings are not available. It is beneficial to quantitatively predict the impact of potential Landsat instrument new angular observations on vegetation monitoring applications. The gap can be filled by this thesis.

### **3.3 Significance of red-edge spectral band for vegetation biophysical variable retrieval**

The red edge is the sharp change in leaf reflectance between 680 and 750 nm. It is a key wavelength region that is sensitive to vegetation conditions and can be used to support different vegetation interested quantity retrieval. The previous work of studying the significance of red-edge band(s) have been reviewed in this section:

For example, the usage of MERIS instrument red-edge spectral bands for estimating the red-edge position were evaluated in [30]. They concluded that the MERIS bands centered at 708.75 and 753.75 nm are beneficial for the red-edge position index (REP) estimation using linear fitting method. Besides, Curran et al designed a vegetation index (MERIS Terrestrial Chlorophyll Index, MTCI) suitable for MERIS spectral band settings [31]. The index is defined using MERIS bands centered at 681nm, 708nm and 753nm. It is easy to be calculated from MERIS data and sensitive to wide range of chlorophyll contents. They also validated the robustness of the proposed index using both modeled and field collected data.

The spectral band settings of Sentinel-2, Landsat-8 and Landsat-7 are as shown in Figure 3.1. The band settings of Sentinel-2 and Landsat-8 are similar within visible, NIR and SWIR region. Due to the similarity, the previous studies about Sentinel-2 mission spectral band settings for vegetation monitoring are valuable for the design of future Landsat in-

strument. The significance of red-edge bands has been directly explored and quantified in part of those Sentinel-2 studies. In the other studies, though not directly calculated, the significance of red-edge bands can be inferred from their results. Some studies were done before the launch of Sentinel-2, they adopted simulation-based approaches to predict the potential of Sentinel-2 bands for vegetation biophysical parameter retrieval. These studies generated simulated Sentinel-2 data by either resampling high-resolution field campaign data or running canopy radiative transfer models (RTM). In [32] Verrelst et al. predicted the retrieval accuracies of LAI, leaf chlorophyll content (LCC), and fractional vegetation cover (FVC) based on machine learning approaches with Sentinel-2 bands. In particular, they compared the retrieval accuracy with the three red-edge bands (705, 740, 780 nm) and the retrieval accuracy without the three red-edge bands. They found slight improvement from their inclusion. In [33], Delegido et al. studied the importance of Sentinel-2 red-edge bands for green LAI retrieval in vegetation index regression approach. For LAI estimation, after testing multiple field campaign datasets, they found the combination of Sentinel-2 red band and 705 nm red-edge band provides the highest retrieval accuracy. In [34], Richter et al. evaluated the performance of crop LAI estimation based on LUT inversion and neural network approaches. They tested all Sentinel-2 band combinations and evaluated the significance of each band by counting the frequency each band appeared in the top 5% of the band combinations. They concluded the importance of spectral regions (in descending order) as NIR, red-edge, visible, and SWIR. Researchers in [35] assessed the importance of Sentinel-2 red-edge bands for wheat and potato crop LAI estimation through both partial least square regression (PLSR) and VI approaches. They concluded the red-edge bands are the most important bands. Fernandes et al. [36] developed a physical based empirical relationship between LAI and the normalized difference of two Sentinel-2 red-edge bands.

Since the launch of the Sentinel-2 satellites, real data have been available. The latest studies have evaluated the significance of Sentinel-2 red-edge bands and compared the performance of biophysical parameter retrieval using Sentinel-2 and Landsat-8 OLI data. In [38] Clevers et al. studied the importance of Sentinel-2 red-edge bands for potato



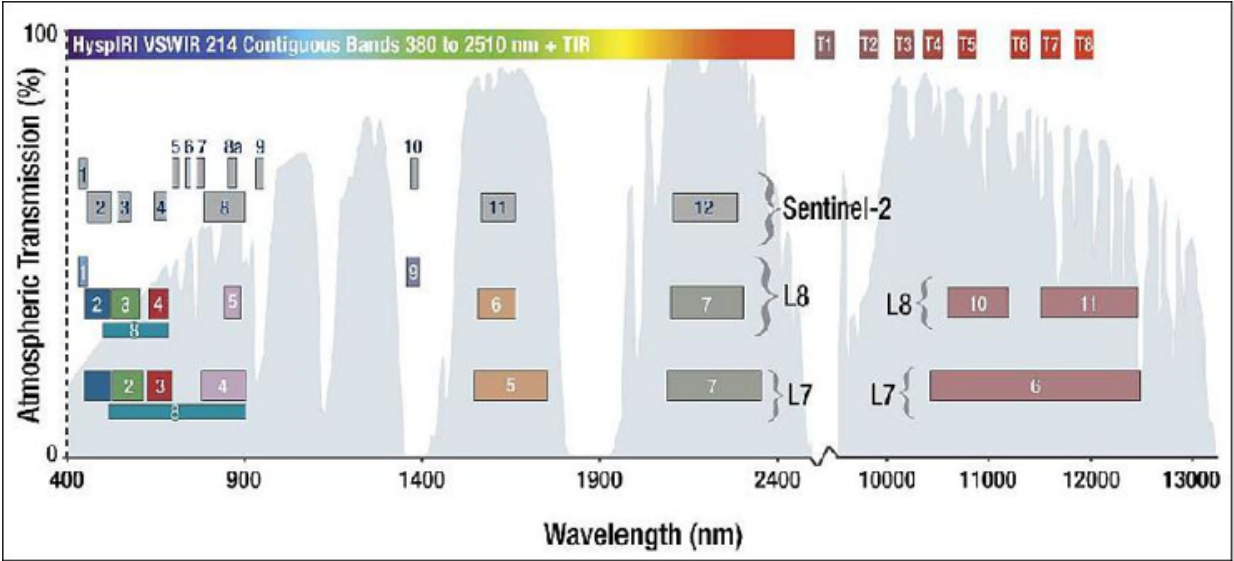


Figure 3.1: Spectral band settings of Sentinel-2, Landsat-8 and Landsat-7 [37].

crop LAI and CCC estimation. They compared the retrieval accuracy using 10m bands VIs (red-edge bands excluded) and the retrieval accuracy using 20m bands VIs (red-edge bands included). They found the VIs composed of red-edge bands can not achieve higher accuracy than VIs composed of non-red-edge bands. Researchers in [39] studied the significance of Sentinel-2 red-edge bands for boreal forest LAI estimation by comparing the results from Sentinel-2 and Landsat-8 data. They found limited improvement (up to approximately 4%) from the addition of the Sentinel-2 red-edge bands.

As mentioned above, the significance of Sentinel-2 red-edge bands for LAI retrieval has been evaluated through different approaches. However, those conclusions from Sentinel-2 studies cannot be directly applied to predict the performance of a future Landsat instrument with red-edge bands. Previous studies have shown that the differences in OLI and Sentinel-2 spectral band position and RSR shape can cause considerable signal differences when observing a forest [40][41]. The specific study about the significance of red-edge band on Landsat instrument is necessary.

### **3.4 Summary**

In this thesis, the gaps mentioned in the above reviewed previous efforts have been filled. For the RSR shift effect study, Chapter 5 of this has quantified the significance of within-sensor deterministic RSR shift effect on radiance signal. For the wider FOV angular observation study, Chapter 6 of this thesis first studied the benefits of the new angular observations from the potential wider FOV future Landsat instrument design for vegetation monitoring purposes. For the addition of red-edge band design, Chapter 7 has been the first work to predict the significance of red edge spectral bands used together with previous Landsat spectral bands for green leaf area index and canopy chlorophyll content retrieval.

# Chapter 4

## Background and Analysis Tools

This chapter presents the necessary background information and analysis tools used in this thesis. Section 4.1 and 4.2 are the basic radiometry theory and the Landsat instrument characteristics, respectively. Section 4.3 introduces the RSR shift effect at large angle-of-incidence (AOI) situation. The RSR shift effect is an interested effect for potential wider FOV instrument design. Section 4.4 reviews the remote sensing based vegetation monitoring applications, and the related algorithms that have been studied and tested in this research. Section 4.5 and 4.6 introduce the synthetic image generation tool DIRSIG and canopy radiative transfer model PROSAIL, respectively. They have been used to generate the synthetic remote sensing data. Section 4.7 reviews the factorial analysis, which has been used for quantifying the factor significance. Section 4.8 is the summary.

### 4.1 Radiometry

In this section, the model describing the travel paths of the photons from light source to sensor is first reviewed in section 4.1.1. Then in section 4.1.2, bi-directional reflectance distribution factor (BRDF) is introduced to describe how the surface reflectance angular variation is parameterized. Finally, section 4.1.3 reviews the sensor RSR characteristics.

### 4.1.1 Basic Radiometry

Radiometry is formally defined as the science of characterizing or measuring how much electro-magnetic (EM) energy is present or associated with, some location or direction in space. It has evolved separately in the fields of physics, illumination or vision, and engineering [1]. In this thesis, only the reflective spectral wavelength region are studied. The reflective spectral wavelength region ranges from visible (VIS: 0.4 - 0.7  $\mu\text{m}$ ) to near infrared (NIR: 0.7 - 1.3  $\mu\text{m}$ ), and to shortwave infrared (SWIR: 1.3 - 3.0  $\mu\text{m}$ ). The radiative transfer within the thermal wavelength range are not covered.

The sensor reaching radiance is the accumulation of photons radiation originating from the sun to the sensor through different paths. Figure 4.1 [42] illustrates the main paths that dominate the sensor reaching energy [1]:

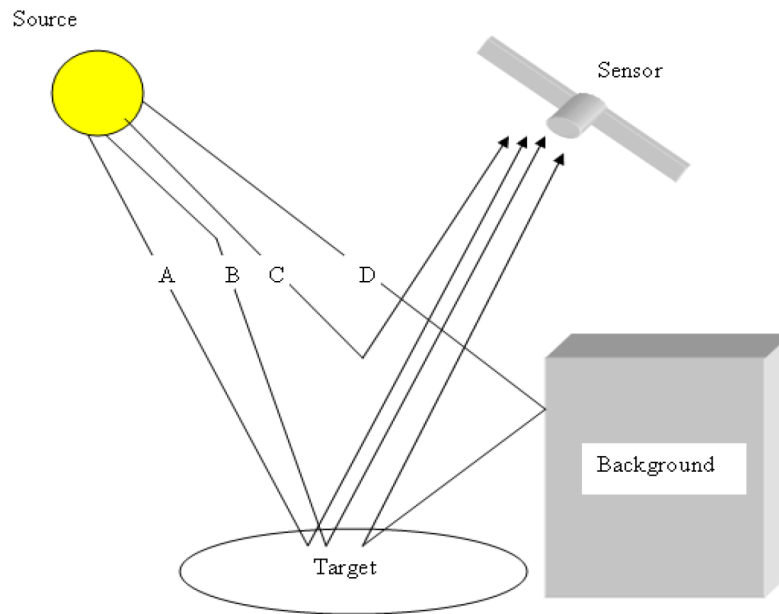


Figure 4.1: Illustration of different radiative transfer path [1].

Path A, which is called direct solar radiance, describes the photons originate from the sun, pass through the atmosphere, reflected by the target and propagate through

the atmosphere to the sensor. Path B, the downwell radiance, describes the photons originate from the sun, scattered by the atmosphere, reflected by the target, and travel through the atmosphere to the sensor. These photons make up what we commonly refer to as skylight. Path C, the upwell radiance, describes the photons originate from the sun and scattered into the sensor without reaching the target. Path D describes the photons from the sun travel through the atmosphere, reflected by the background object and reflected off the target to the sensor [1].

In general, path A,B and C dominate the photons reaching the sensor and they are the paths studied in this thesis. The top of atmosphere (TOA) radiance signal reaching the sensor, which is a combination of the three path signals, can be goverened into one equation 4.1:

$$L_{toa}(\lambda) = [E_{solar}(\lambda) \cdot \cos\theta \cdot \tau_1(\lambda) + E_d(\lambda)] \cdot \frac{r(\lambda)}{\pi} \cdot \tau_2(\lambda) + L_u(\lambda) \quad (4.1)$$

where  $L_{toa}(\lambda)$  is TOA spectral radiance,  $E_{solar}(\lambda)$  is the spectral solar irradiance reaching the ground,  $\theta$  is the solar irradiance incident angle,  $\tau_1(\lambda)$  is the spectral transmission between sun and ground,  $E_d(\lambda)$  is the spectral downwelled irradiance,  $r(\lambda)$  is the ground reflectance,  $\tau_2(\lambda)$  is the spectral transmission between ground and sensor, and  $L_u(\lambda)$  is the spectral upwell radiance.

### 4.1.2 BRDF

The surface reflectance properties play an important role in calculating the radiative propagation. The reflectance properties of materials are function of wavelength, illumination angle, and viewing angle. The angular signatures can be measured and exploited to provide enhanced surface information [43]. Figure 4.2 [1] are several typical directional reflectance characteristics types.

The bidirectional reflectance distribution function (BRDF) is defined as the ratio of the radiance scattered into the direction described by the orientation angles  $\theta_o, \phi_o$  to the irradiance from the direction  $\theta_i, \phi_i$ , as shown in Equation 4.2 [44] and Figure 4.3 [1]:

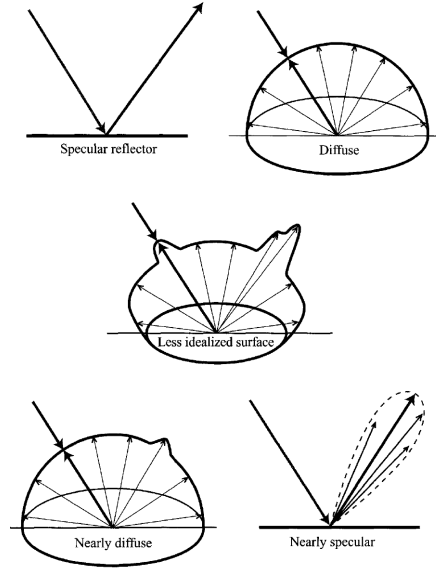


Figure 4.2: Typical surface directional reflectance characteristics [1].

$$BRDF = f_r(\theta_i, \phi_i; \theta_o, \phi_o; \lambda) = \frac{dL_r(\theta_i, \phi_i; \theta_o, \phi_o; \lambda)}{dE_i(\theta_i, \phi_i; \lambda)} \quad (4.2)$$

BRDF describes the intrinsic reflectance properties of a surface and thus facilitates the derivation of many other relevant quantities. However, it is expressed as the ratio of infinitesimal quantities and can not be directly measured [44]. In real scenario, when measuring the reflectance properties of a surface, the procedure usually follows the definition of a reflectance factor. Bidirectional reflectance factor (BRF) is the ratio of the reflected radiant flux reflected by a sample surface to the radiant flux reflected into the identical beam geometry by an ideal Lambertian standard surface [44], as shown in Equation 4.3

$$BRF = R(\theta_i, \phi_i; \theta_r, \phi_r) = \frac{d\Phi(\theta_i, \phi_i; \theta_r, \phi_r)}{d_r^{id}(\theta_i, \phi_i)} = \frac{f_r(\theta_i, \phi_i; \theta_r, \phi_r)}{f_r^{id}(\theta_i, \phi_i)} = \pi \cdot f_r(\theta_i, \phi_i; \theta_r, \phi_r) \quad (4.3)$$

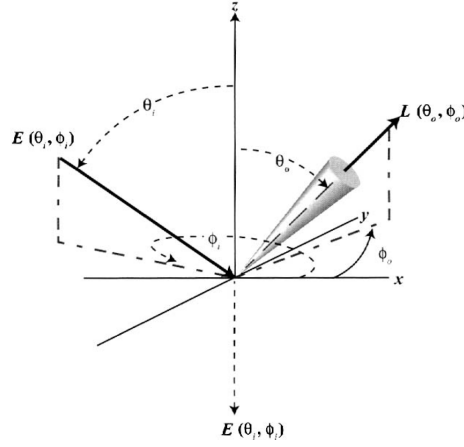


Figure 4.3: Illustration of geometry of BRDF definition [1].

Since an ideal Lambertian surface reflects the same radiance in all view directions, and its BRDF is  $\frac{1}{\pi}$ , the unitless BRF of any surface can be expressed as its BRDF  $[sr^{-1}] \cdot \pi[sr]$ .

BRDF can be measured indirectly in the laboratory or in the field. However, since BRDF is directional and spectral variant, it is impractical and time consuming to measure BRDF of all variable combination conditions. Instead, researchers explored to describe the infinite BRDF conditions using parametrized models with limited number of parameters. Different BRDF models have been proposed to describe different material surface properties. Since this thesis focuses on the vegetation monitoring applications, only the forest canopy BRDF model is introduced here.

The Ross-Li BRDF model, as shown in Equation 4.4, is a linear semi-empirical BRDF model formulated based on isotropic scattering, radiative transfer type volumetric scattering kernel as from horizontally homogeneous leaf canopies, and geometric-optical surface scattering kernel as from scenes containing 3-D objects that cast shadows and are mutually obscured from view at off nadir angles [45].

$$R(\theta, \vartheta, \phi, \lambda) = f_{iso}(\lambda) + f_{vol}(\lambda)K_{vol}(\theta, \vartheta, \phi) + f_{geo}(\lambda)K_{geo}(\theta, \vartheta, \phi) \quad (4.4)$$

The kernel values for a ground facet are determined by variables including local solar

zenith angle  $\theta$ , view zenith angle  $\vartheta$ , solar/view relative azimuth angle  $\phi$ , and wavelength  $\lambda$ . The key parameters of Ross-Li model are the three wavelength dependent weighting factors  $f_{isor}$ ,  $f_{vol}$  and  $f_{geo}$ .

In detail, the volumetric kernel, named Ross-Thick model, is expressed as Equation 4.5 [46]:

$$K_{vol} = K_{RT} = \frac{(\frac{\pi}{2} - \xi)\cos\xi + \sin\xi}{\cos\theta + \cos\vartheta} - \frac{\pi}{4} \quad (4.5)$$

where  $\cos\xi = \cos\theta\cos\vartheta + \sin\theta\sin\vartheta\cos\phi$

The geometric kernel is derived from the geometric-optical mutual shadowing BRDF model by Li and Strahler, as shown in Equation 4.6 [47]:

$$K_{geo} = k_{LSR} = O(\theta, \vartheta, \phi) - \sec\theta' - \sec\vartheta' + \frac{1}{2}(1 + \cos\xi')\sec\theta'\sec\vartheta' \quad (4.6)$$

with

$$O = \frac{1}{\pi}(t - \text{sintcost})(\sec\theta' + \sec\vartheta')$$

$$\text{cost} = \frac{h}{b} \frac{\sqrt{D^2 + (\tan\theta' \tan\vartheta' \sin\phi)^2}}{\sec\theta' + \sec\vartheta'}$$

$$D = \sqrt{\tan^2\theta' + \tan^2\vartheta' - 2\tan\theta' \tan\vartheta' \cos\phi}$$

$$\cos\xi' = \cos\theta' \cos\vartheta' + \sin\theta' \sin\vartheta' \cos\phi$$

$$\theta' = \tan^{-1}\left(\frac{b}{r}\tan\theta\right)$$

$$\vartheta' = \tan^{-1}\left(\frac{b}{r}\tan\vartheta\right)$$

Here,  $O$  is the overlap area between the view and solar shadows. The term  $\text{cost}$  should be constrained to the range  $[-1,1]$ .  $\frac{h}{b}$  and  $\frac{b}{r}$  are crown relative height and shape parameters [45].

Ross-Li BRDF model has been verified to be effective to capture the canopy angular reflectance variation within reasonable range. It has been adopted by MODIS BRDF and surface albedo products [48].



### 4.1.3 RSR

Spectral sensitivity is the relative efficiency of sensor detection of light, as function of wavelength of the signal. The relative spectral response (RSR), which is a unitless quantity, is obtained by normalizing the spectral sensitivity function by its peak spectral response. The photons reaching the ground are reflected by the target, propagate through the atmosphere and reach the satellite instrument. Then the at-detector spectral radiance signal is the integration of TOA spectral radiance profile with the RSR within the interested wavelength range, as shown in Equation 4.7.

$$L_{total} = \int_{\lambda_1}^{\lambda_2} L_{TOA}(\lambda) RSR(\lambda) d\lambda \quad (4.7)$$

## 4.2 Landsat 8 OLI Characteristics

In this thesis, the Landsat 8 OLI instrument spectral and radiometric settings serve as the baseline for future Landsat instrument system trade-off studies. In this section the characteristics of the Landsat 8 OLI, including its RSR and signal-noise-ratio (SNR) are introduced. They were used in the simulation experiments of the thesis.

### 4.2.1 OLI RSR

The OLI is a pushbroom scanner with nine spectral bands. The OLI detectors are divided between 14 focal plane modules (FPMs) as shown in Figure 4.4 [12]. Each FPM includes nine arrays of detectors covered by nine spectral filters to differentiate the spectral bands. The order of the spectral band detectors from most off-axis to least off-axis is: cirrus, SWIR1, SWIR2, green, red, NIR, coastal aerosol, blue and panchromatic [12].

Table 4.1 [11] shows the OLI spectral band characteristics. And the pre-launch measured average detector RSR of each OLI band are as shown in Figure 4.5 [12]:

Due to the special FPM structure, RSR non-uniformity has been observed within

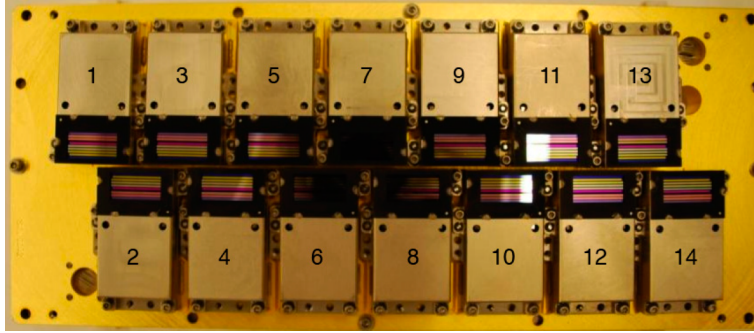


Figure 4.4: The complete OLI focal plane [12].

Spectral Band	Wavelength ( $\mu m$ )	GSD( $m$ )
coastal aerosol	0.43 - 0.45	30
blue	0.45 - 0.51	30
green	0.53 - 0.59	30
red	0.64 - 0.67	30
NIR	0.85 - 0.88	30
SWIR1	1.57 - 1.65	30
SWIR2	2.11 - 2.29	30
panchromatic	0.50 - 0.68	15
cirrus	1.36 - 1.38	30

Table 4.1: Landsat 8 OLI spectral band characteristics.

and between different FPMs. Figure 4.6 [11] is an example of the between FPMs RSR non-uniformity in OLI band NIR. However, to simplify the simulation, in this research the average RSR of each band was used for the corresponding detectors. The RSR non-uniformity was not assumed.

Among the nine OLI bands, the coastal aerosol and cirrus bands are designed for atmospheric concentration estimation purposes. The panchromatic band is designed to provide high spatial resolution data. The other six bands (blue, green, red, NIR, SWIR1, SWIR2) are the primary multispectral bands designed for land surface cover analysis and in particular for vegetation monitoring. Since this research mainly focuses on these applications, only these six spectral bands were considered in simulations.

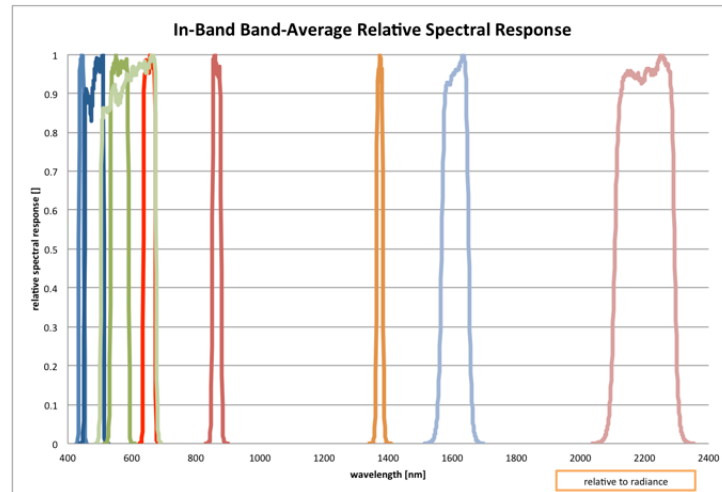


Figure 4.5: OLI RSRs.

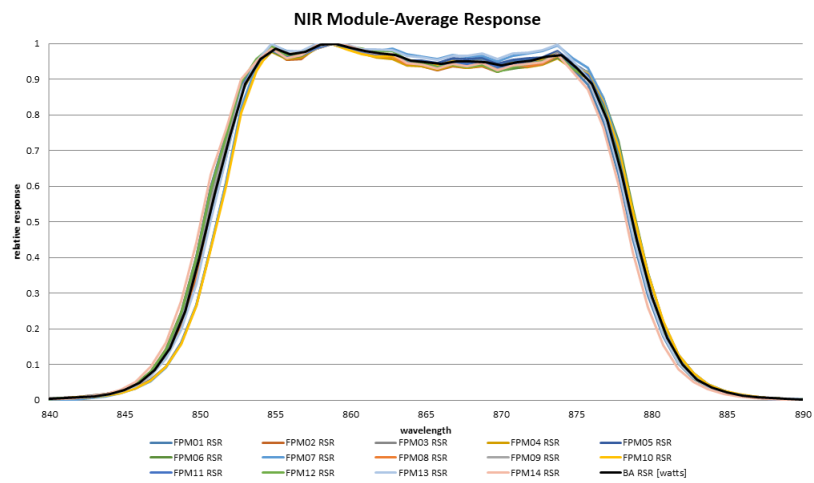


Figure 4.6: OLI NIR band RSR non-uniformity between different FPMs [11].

### 4.2.2 OLI SNR

The detector SNR is spectral band and signal level dependent. This means the SNR of different spectral bands are different. And the SNR are different within the same spectral band at different signal levels. In this research, the pre-launch measured OLI SNR performance was used to model the radiance signal noise. The pre-launch measured OLI SNR performance at two different signal levels are in Table 4.2 [12]:

Spectral Band	$L_{typical}$ ( $W/m^2sr\mu m$ )	$L_{high}$ ( $W/m^2sr\mu m$ )	$SNR_{typical}$	$SNR_{high}$
blue	40	190	355	1127
green	30	194	296	1213
red	22	150	222	945
NIR	14	150	199	1009
SWIR1	4	32	261	1007
SWIR2	1.7	11	326	1030

Table 4.2: OLI pre-launch measured SNR performance for different signal level.

## 4.3 RSR Shift Effect

For future Landsat instrument architecture design, some proposed instrument concepts incorporate a wider FOV to allow more frequent imaging of ground areas. Depending on the implementation, one potential consequence of this may be a higher AOI for light entering the optical band filters than currently occurs in OLI. It is a known characteristic of multilayer dielectric filters that the central wavelength of the bandpass will shift towards shorter wavelengths as the AOI increases [49]. Figure 4.7 [49] shows the example of how the RSR shift when s-polarized light and p-polarized light incident from different AOIs. This could lead to a variation of the signal measured across the swath with a complicated interplay between the filter response, the atmosphere, and the surface reflectance spectra.

For each band RSR, the quantitative relationship between the angle dependent wavelength shift and the AOI can be approximated as Equation 4.8:

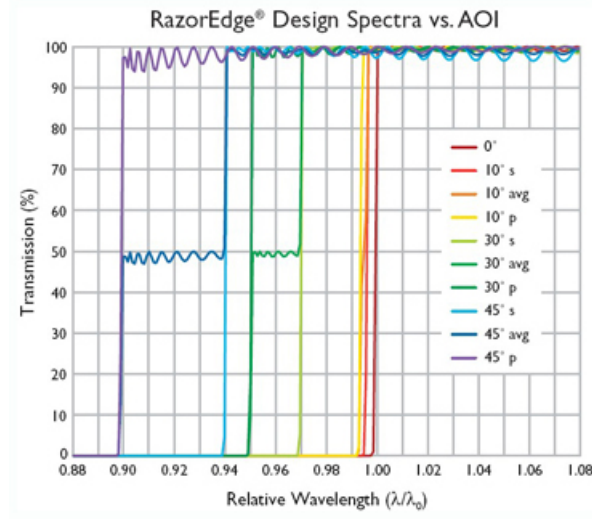


Figure 4.7: Two distinct filter spectra emerge for s- and p-polarized light as AOI increases [49].

$$\lambda_{\theta} = \lambda_0 \left[ 1 - \left( \frac{n_0}{n_*} \right)^2 \sin^2 \theta \right]^{0.5} \quad (4.8)$$

where  $\lambda_{\theta}$  is the central wavelength of RSR when AOI is  $\theta$ ,  $\lambda_0$  is the central wavelength of RSR when the detector is at nadir view (normal incidence),  $n_0$  is refractive index of the medium surrounding the filter, and  $n_*$  is effective refractive index of the filter [49]. To estimate the  $n_*$  for each OLI filter, different angles of incidence and the corresponding RSR shift amount were measured over the OLI off-axis angles up to 3.5 degrees. These measurements were then fitted to the model in Equation 4.8 with the assumption  $n_0 = 1$ . The resulted  $n_*$  are listed in Table 4.3. The assumption in this study is that future Landsat filters have the same set of  $n_*$  as OLI.

---

Spectral Band	$n_*$
blue	1.8
green	1.75
red	1.75
NIR	2
SWIR1	1.7
SWIR2	1.7

---

Table 4.3: Landsat 8 OLI effective refractive index ( $n_*$ ) of filters for each band.

## 4.4 Vegetation Monitoring

Since two vegetation monitoring applications are mainly tested in this research: crop mapping and crop biophysical parameter retrieval, this section reviews the applications and the related algorithms. Section 4.4.1 introduces the four crop classification algorithms and dimension reduction methods used in this thesis. Section 4.4.2 presents the major vegetation variable retrieval approaches.

### 4.4.1 Crop mapping

Crop mapping is one of the typical remote sensing based agricultural applications. The US Department of Agriculture (USDA) use Landsat and Landsat-like satellites to monitor cropping systems. One example is the Cropland Data Layer (CDL), which is annually updated to define over 100 land cover and crop type classes at 30m resolution [50]. These data can be served for other applications such as change detection.

Different land mapping algorithms have been proposed in the past decades. They can be grouped in two major categories: unsupervised and supervised classifications. Supervised classification methods process where the user identifies a sample of pixels of each type or class, and digital processing algorithms are used to assign all similar pixels to one of the classes [1]. On the other hand, unsupervised classification methods have the algorithms sort out which pixels have similar characteristics rather than to try to

force the pixels into a class based on our culturally driven sense of their similarities [1].

In this research, to study the impact of increasing FOV in future Landsat satellite instrument on crop classification accuracy, four different supervised classification algorithms were tested: linear discriminant analysis (LDA), k-nearest neighbor (kNN), support vector machine (SVM) and decision tree (DT). It should be noted that the objective of this research is to study the impact of larger FOV instrument on crop mapping accuracy, rather than to improve the crop classification accuracy as high as possible. These four algorithms were selected because they are widely used and can serve as baseline in classification algorithm development.

### Linear Discriminant Analysis

Linear Discriminant Analysis (LDA) is a classifier with linear decision boundaries. The boundaries are generated by fitting class conditional densities to the data using Bayes rule. LDA fits a Gaussian distribution to each class, assuming that all classes share the same covariance matrix. The Bayes theorem is as Equation 4.9

$$Pr(G = k|X = x) = \frac{f_k(x)\pi_k}{\sum_{l=1}^K f_l(x)\pi_l} \quad (4.9)$$

where  $Pr(G = k|X = x)$  is the posterior probability of the data sample  $x$  is in class  $k$ .  $f_k(x)$  is the class conditional density of  $x$  in class  $k$ .  $\pi_k$  is the prior probability of class  $k$ . LDA assume each class follows the multivariate Gaussian distribution as Equation 4.10

$$f_k(x) = \frac{1}{(2\pi)^{p/2} |\Sigma_k|^{1/2}} e^{-\frac{1}{2}(x-\mu_k)^T \Sigma_k^{-1} (x-\mu_k)} \quad (4.10)$$

And all classes share a common covariance matrix  $\Sigma_k = \Sigma \forall k$ . When comparing the probability of sample  $x$  in class  $k$  and class  $l$ , we look at the log-ratio and have Equation 4.11

$$\log \frac{Pr(G = k|X = x)}{Pr(G = l|X = x)} = \log \frac{f_k(x)}{f_l(x)} + \log \frac{\pi_k}{\pi_l} = \log \frac{\pi_k}{\pi_l} - \frac{1}{2}(\mu_k + \mu_l)^T \Sigma^{-1}(\mu_k - \mu_l) + x^T \Sigma^{-1}(\mu_k - \mu_l) \quad (4.11)$$

The log-ratio is linear in  $x$ . This indicates that the decision boundary with  $Pr(G = k|X = x) = Pr(G = l|X = x)$  is linear in  $x$ . For each class  $k$ , the linear discriminant function is defined as Equation 4.12

$$\delta_k(x) = x^T \Sigma^{-1} \mu_k - \frac{1}{2} \mu_k^T \Sigma^{-1} \mu_k + \log \pi_k \quad (4.12)$$

So for given  $x$ , it is classified to the class with max discriminant function value.

In practice, to use LDA, we need to estimate the parameters using the training data:

$\widehat{\pi}_k = N_k/N$  where  $N_k$  is the number of class  $k$  observations

$\widehat{\mu}_k = \sum_{g_i=k} x_i / N_k$

$\widehat{\Sigma} = \sum_{k=1}^K \sum_{g_i=k} (x_i - \widehat{\mu}_k)(x_i - \widehat{\mu}_k)^T / (N - K)$

Geometrically, LDA can be described as each class  $k$  is represented by a prototype  $\mu_k$  and each test data is assigned to the class with the nearest Mahalanobis distance [51].

### k-Nearest Neighbor

k-nearest neighbor (kNN) is among the prototype methods and requires no model to be fit. It is non-parametric and can not be used for exploiting the underlying relationship between the features and class labels. However, kNN is effective and often outperforms the other algorithms in real data problems. Given a test sample, the algorithm finds the  $k$  training samples that are closest in distance to the test sample and then classifies using majority vote among the  $k$  neighbors [51]. Usually the Euclidean distance in the data feature space is adopted as the metric to measure the distance between test and training samples. The kNN classification criterion is as shown in Equation 4.13.



$$\widehat{Y}(x) = \frac{1}{k} \sum_{x_i \in N_k(x)} y_i \quad (4.13)$$

where  $N_k(x)$  is the neighborhood of  $x$  consisted of the  $k$  nearest samples  $x_i$  in the training set. In words, kNN finds the  $k$  training data samples  $x_i$  closest to input sample  $x$ , and averages their responses as the prediction.

kNN has been successful in a large number of classification problems, including multispectral remote sensing data, handwritten digits and EKG patterns. It is often successful when each class has many possible prototypes and the decision boundary is irregular [51].

### Support Vector Machine

Given labeled training data, support vector machine (SVM) outputs an optimal hyperplane that gives the largest minimum distance (margin) to the training samples. In other words, the optimal separating hyperplane maximizes the margin of the training data. When the data is not linear separable, the algorithms assuming linear decision boundary may not work. But they can be generalized to produce nonlinear boundaries by constructing a linear boundary in a large, transformed version of the feature space [51]. In SVM, kernel trick can be used to map the linear non-separable features to higher dimensional linear separable space. Also, to make the SVM more robust to noise, soft margin scheme is introduced to allow mis-classification in the training set.

### Decision Tree

Decision Tree (DT) is a non-parametric supervised learning method and can be used for both classification and regression problems. Decision tree can handle the nonlinear relationship between features and labels, and allows for missing values. The goal of DT is to create a model that predicts the value of a target variable by learning simple decision rules inferred from the data features. The advantages of decision tree techniques

for remote sensing data classification problems are their flexibility, intuitive simplicity, and computation efficiency [52].

In general, DT is defined as a classification procedure that recursively partitions a dataset into smaller subgroups on the basis of a set of tests defined at each branch in the tree. Unlike conventional statistical classifiers that use all features simultaneously to make the classification, the DT adopts a multi-stage framework to classify the samples. The labelling process is considered to be a chain of simple decisions based on the results of sequential tests rather than a single, complex decision.

Different strategies to automatically split the training data have been proposed for DT. Among them, C4.5 [53] is popular for univariate data. Univariate decision tree means the decision at each node of the tree are made using a single feature of the data. On the contrary, multivariate decision tree uses multiple features combinations in each node to make the split and decision.

Another advantage of decision tree is that it can be combined with other classifiers. The decision model used in each node can be different. For example, LDA, kNN can be used as the decision strategies in different nodes. This makes the decision tree a flexible framework for classification problems.

### **Canonical Correlation Analysis**

For multispectral or hyperspectral image classification, not all bands (features) are necessary to be used as the input to the classifier. The redundant information contained in the unnecessary features deteriorate the classifier performance. Especially, multi-angular observations based classification was conducted in this research. The information redundancy was more severe in this case. To avoid this, a feature selection procedure on the training data is necessary before the classification or regression. In this study, canonical correlation analysis (CCA) was adopted for data dimension reduction.

CCA deals with two groups of variables and tries to investigate correlations between the two groups [54]. Mathematically, we define the two sets of random variables as two random vectors [54]:

$$X = [X_1, X_2, \dots, X_p]^T$$

$$\text{and } Y = [Y_1, Y_2, \dots, Y_q]^T$$

The goal of CCA is to find the linear combinations:

$U = a^T X = a_1 X_1 + a_2 X_2 + \dots + a_p X_p$  and  $V = b^T Y = b_1 Y_1 + b_2 Y_2 + \dots + b_q Y_q$  that maximize the correlation:  $\text{Corr}(U, V) = \frac{\text{Cov}(U, V)}{\sqrt{\text{Var}(U)} \sqrt{\text{Var}(V)}}$

CCA can find the canonical variables:

$U = a^T X = e_k^T \Sigma_{XX}^{-1/2} X$  and  $V = b^T Y = f_k^T \Sigma_{YY}^{-1/2} Y$  that maximize  $\text{Corr}(U_k, V_k)$ . Where  $\Sigma_{XX} = \text{Var}(X)$ ,  $\Sigma_{YY} = \text{Var}(Y)$ ,  $\Sigma_{XY} = \text{Cov}(X, Y)$ . And  $e_1, e_2, \dots, e_m$  are the normalized p-dimensional eigenvectors of the matrix  $\Sigma_{XX}^{-1/2} \Sigma_{XY} \Sigma_{YY}^{-1} \Sigma_{XY}^T \Sigma_{XX}^{-1/2}$ ,  $f_1, f_2, \dots, f_m$  are the normalized q-dimensional eigenvectors of the matrix  $\Sigma_{YY}^{-1/2} \Sigma_{XY} \Sigma_{XX}^{-1} \Sigma_{XY}^T \Sigma_{YY}^{-1/2}$ .

In this study, the input multispectral training data for classification are the random variable X, while the corresponding labels for each training sample are the categorical random variable Y. Conducting CCA on the input training data with respect to the labels before classification can find two sets of new variables that have less features while maximizing the within-class dispersity. The dimension reduced data can decrease the computation time in the classification while increasing the classification accuracy.

#### 4.4.2 Crop Parameter Retrieval

Among all vegetation related parameters, leaf area index (LAI), leaf chlorophyll content (LCC) and canopy chlorophyll content (CCC) are the most common ones. LAI is defined as the leaf area per unit ground area [55]. It is required by many process models to describe energy and mass exchanges in the soil/plant/atmosphere system [56]. Leaf chlorophyll content (LCC) can be considered as a bio-indicator of plant health status and of vegetation gross productivity [33]. Canopy chlorophyll content, as shown in Equation 4.14, can be expressed by the product of LAI and LCC. It is an indicator of the vegetation chlorophyll concentration in the canopy level.

$$CCC = LAI \times LCC \quad (4.14)$$

So far, different methods have been proposed to retrieve LAI, LCC and CCC from top of canopy (TOC) reflectance spectra. These methods can be divided into four categories: 1) retrieval based on the empirical relationship between vegetation index (VI) and interested variable; 2) physical model based inversion, including iterative optimization and look-up-table (LUT) inversion; 3) machine learning approach, e.g., neural networks (NNs) [56]; 4) Hybrid method that combines physical methods and machine learning methods. Each category has advantages and disadvantages.

Empirical methods exploit the empirical relationship between interested biophysical quantities and different VIs. They are easy to be implemented, but are time and location variant. They also suffer from saturation effects [33][57]. Figure 4.8 [33] is an example of exploring the empirical relationship between chlorophyll content and four different VIs.

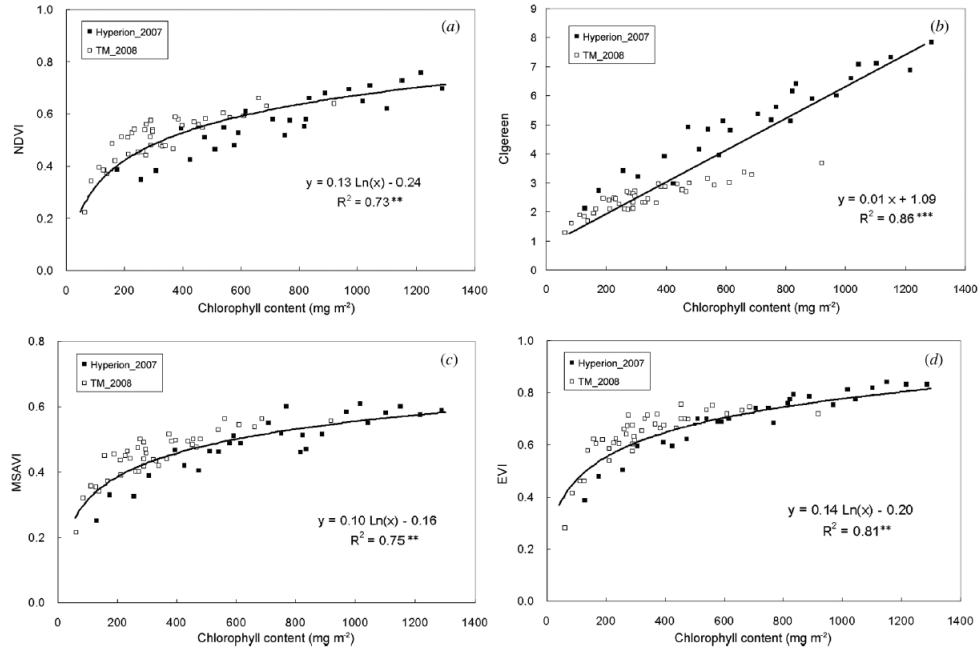


Figure 4.8: Example of canopy leaf chlorophyll retrieval using four different VIs [33].

The physical model based approaches, such as look-up-table (LUT) inversion, are

more general and can be adopted globally. In previous researches, different vegetation physical radiative transfer models (RTM) were used to generate LUT. Then each real reflectance spectra is compared with LUT using specific cost functions to search for the closest entry as the solution. Physical model based approaches are the most widely used methods in satellite based products. Figure 4.9 [56] summarizes the algorithms, RT models and inversion techniques used in different satellite biophysical quantity retrieval products [56].

#	Algorithm	RT models				Inversion technique	uncertainties	prior information	
		leaf	soil	Canopy	Atmosphere				
1	<b>POLDER</b> <i>LAI, fAPAR</i>	PROSPECT N, Cab, (Cw,Cdm, Cs)	PRICE 2 abundances	Kuusk LAI, ALA, hot	TOC	NNT	measurements	Some variables fixed Range of variation	
2	<b>MODIS/MISR</b> <i>LAI, fAPAR</i>	prescribed for each biome	Hapke 3 typical + understorey	DISORD 6 biomes	TOC	LUT	measurements prescribed at 20%	specific values for 6 biomes	
3	<b>MERIS<sup>(1)</sup></b> <b>MGVI</b> <i>fAPAR</i>	PROSPECT N, Cab, (Cw,Cdm, Cs)	5 typical soil unique BRDF	Gobron LAI, ALA, hot	TOA (MODTRAN)	Parametric	not specified	Range of variation (uniform distribution)	
4	<b>VEGETATION<sup>(2)</sup></b> <b>CYCLOPES</b> <i>LAI, fAPAR, fCover</i>	PROSPECT N, Cab, Cw,Cdm, Cbp	brightness parameter &reference spectra	SAIL LAI, ALA, hot, vCover	TOC	NNT	model and measurements prescribed at 4% (relative)	approximation of actual distribution	
5	<b>VEGETATION-Canada-Global</b> <i>LAI</i>	Empirical relations for specific biomes using TM sensor and the corresponding ground measurements over some sites Prescribed BRDF model				TOC	Parametric	not specified	Specific relations for each biome
6	<b>MERIS</b> <i>LAI, fAPAR, fCover, LAIxCab</i>	PROSPECT green/brown separated N, Cab, Cdm, Cw, Cbp	brightness parameter &reference spectra	SAIL, LAI, ALA, hot, vCover	2 versions: - TOC version - TOA version (SMAC)	NNT	model and measurements prescribed at 4% (relative)	approximation of actual distribution	

Figure 4.9: Summary of several algorithms used operationally to retrieve canopy biophysical variables [56].

Machine learning approaches are fast and can capture the nonlinear relationship between different parameters. But they are time variant and location dependent. Verrelst et al [32] used neural network (NN), support vector regression (SVR) and Gaussian process regression (GPR) to study the opportunity of Sentinel-2 and 3 for biophysical parameter retrieval. Bacour et al [3] combined NN and RT model to estimate different vegetation parameters using MERIS reflectance data. They both achieved comparable or

higher performance than empirical and physical model based algorithms in local scale parameter retrieval problems.

There have been several studies focused on vegetation biophysical quantity retrieval based on Landsat data [57][58][59][60]. However, most of them used Landsat ETM+ / TM data, which have lower SNR and a wide NIR band (760-900nm) that covers the entire red-edge wavelength range. Comparing to ETM+ and TM, Landsat 8 OLI has a much narrower NIR band (850-880nm), which covers only the high reflectance plateau. However, OLI does not include a narrow band that captures the raise in reflectance between the red and the NIR bands. Such a new band is of interest for future Landsat instruments and was studied in this research. In this research, for canopy biophysical quantity retrieval applications, three major retrieval approaches were tested: empirical VI regression, support vector regression (SVR) and LUT inversion. They are introduced in the following section.

### Support Vector Regression

Similar as finding the optimal hyperplane that separates two classes in the support vector machine classification, the goal of support vector regression (SVR) is to estimate an unknown continuous valued function based on a finite number set of training samples [61]. In SVR, the input  $s$  is first mapped onto an  $m$ -dimensional feature space using some fixed (nonlinear) mapping. Then a linear model is constructed in this feature space [62]. The linear model in the feature space is given by Equation 4.15

$$f(x;w) = \sum_{j=1}^m \omega_j \varphi_j(s) + b \quad (4.15)$$

where  $\varphi_j(s)$ ,  $j = 1, 2, \dots, m$  represents a high dimensional feature space, which is nonlinearly mapped from the input space  $s$ , and  $b$  is the bias term assumed to be zero and dropped [61].

The quality of the estimation is measured by the loss function  $L_\epsilon(y, f(s, \omega))$ . SVR

adopts  $\varepsilon$ -insensitive loss function proposed by Vapnik [62], as shown in Equation 4.16

$$L_{\varepsilon}(y, f(s, \omega)) = \begin{cases} 0 & \text{if } |y - f(s, \omega)| \leq \varepsilon \\ |y - f(s, \omega)| - \varepsilon & \text{otherwise} \end{cases} \quad (4.16)$$

### Look-up-table Inversion

Look-up-table (LUT) inversion is the retrieval algorithm for MODIS and MISR LAI products. LUT is generated by running radiative transfer models (RTM). In practice, the RTM input variables should span the entire possible distribution and been effectively sampled. Once the LUT has been built, the test spectra is compared to each sample in the LUT according to a cost function, and the canopy biophysical variables corresponding to the closest sample in LUT are the solution.

The LUT inversion is often an under-determined problem. Because the number of unknowns is larger than the number of independent radiometric information remotely sampled by sensors [56]. For example, the RTM PROSAIL needs at least 13 inputs variables and these 13 unknowns have to be estimated from the information content in six bands Landsat measurements. Even though some instruments have the capability to provide multidirectional observations that have large number of dimensions, the actual intrinsic dimensionality is much smaller considering the relatively high level redundancy between bands and directions [56]. For this ill-posed problem, ancillary information or constraints can be introduced to improve the retrieval performance, such as prior information, spatial constraints and temporal constraints. In this research, we tested the potential of adding new angular observations to improve the retrieval performance.

## 4.5 DIRSIG

Since this research is based on simulation approach, this section introduces the synthetic image generation tool that has been used throughout this thesis.

The Digital Imaging and Remote Sensing Image Generation (DIRSIG) tool was developed by the Digital Imaging and Remote Sensing (DIRS) Laboratory at RIT [1]. The tool is a ray tracing based synthetic image generation tool and integrates a suite of first-principles based radiation propagation modules to produce passive broadband, multi-spectral, hyper-spectral, LIDAR, and SAR data [63] [64].

A DIRSIG simulation is composed of five major components: 1) the scene component, 2) the atmosphere component, 3) the platform component, 4) the platform motion component and 5) the tasks component. These components describe the details of every link in the imaging chain and constitute a DIRSIG simulation [65].

The scene component describes the target being observed by the sensor. Basically it describes the target 3D geometry and assigns material descriptions such as the optical properties to drive the radiometric prediction. A proper coordinate system should be selected to describe the objects location and orientation accurately. The entire scene can be assumed to be on a flat plane when its extend is limited, or on a sphere with the radius of earth when simulating the large swath space borne instrument observations. The scene file can be generated in various of ways, and more detailed description of the scene building will be introduced later.

The atmosphere component allows the user to set the optical properties of the atmosphere. DIRSIG has a suite of interface modules to call externally developed atmospheric models such as MODTRAN [66]. Several different atmosphere modes are available for different simulation purposes: uniform, simple and classic atmosphere modes.

The platform component describes the data acquisition platform model that can have one or more imaging instrument sensors attached to it [63]. The platform model positions sensor(s) and synchronizes them by global clocking mechanisms. At least one imaging instrument should be described in the platform component. Different instrument types are supported, including frame camera, pushbroom scanner, whiskbroom scanner etc. The detector size, spatial layout, detector spectral response, and sub-pixel sampling scheme can also be set in the platform file. Besides, if ground truth is required, the truth collector can also be set in platform component to support the data analysis.



The platform motion component describes the position and orientation of a static platform, or the position and orientation of a moving platform as a function of time. The motion description can be provided in either parameterized model or data driven.

The task component controls when the sensor is on to record the data. Different sensor modes are supported: instantaneous capture for frame camera or setting the time of start and stop acquiring data for a pushrboom or whiskbroom scanner.

DIRSIG has been validated by many researches from different perspectives: Cui et al. [67] validated DIRSIG simulated Landsat-8 OLI images versus corresponding real data. In [68] and [69] Bloechl et al. and Cui et al. studied the similarity between DIRSIG simulated hyperspectral images and the corresponding SHARE 2012 campaign real data. All these validation efforts have proved that DIRSIG can capture the key characteristics of real images for a variety of scenes.

## 4.6 PROSAIL

To study the impacts of potential future Landsat instrument system designs on vegetation monitoring tasks, accurate descriptions of the canopy angular reflectance characteristics are necessary. Different canopy radiative transfer models (RTM) have been proposed so far for this purposes. Some models simulate the light reflection, absorption and transmission with fully described canopy geometry models. These models require large effort in scene building and are very time consuming. Some models simplify the canopy as parameterized descriptions. These models make different assumptions to simplify and parameterize the radiative transfer between canopy leaves and the understory such as soil.

The PROSAIL model is one of the parametrized RTM family. It is a combination of the leaf optical properties model PROSPECT [70] and the canopy bidirectional reflectance model 4SAIL [71]. The PROSAIL model allows a description of both the spectral and directional variation of canopy reflectance as a function of leaf biochemistry and canopy architecture [70]. A typical PROSAIL model simulation is as shown in Figure 4.10 [72].

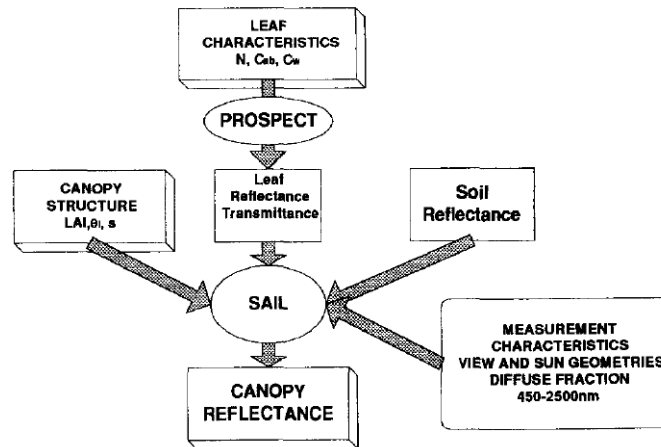


Figure 4.10: Schematic representation of the PROSPECT+SAIL canopy reflectance model [72].

PROSPECT, the leaf model, assumes the leaf as multi-layer structure of air and material plates, as shown in Figure 4.11 [73]. Each plate has its own spectral refractive index and specific absorption coefficients.

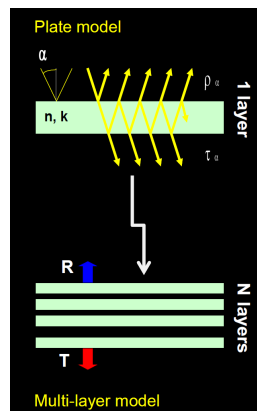


Figure 4.11: Plate model and multi-layer model of leaf structure [73].

After parametrization, the PROSPECT model simulates the bi-Lambertian reflectance and transmittance of leaves as Equation 4.17

$$[refl, tran] = PROSPECT(N, C_{ab}, C_w, C_{bp}, C_m) \quad (4.17)$$

where  $N$  is the leaf structure parameter,  $C_{ab}$  is the concentration of chlorophyll a and b,  $C_{bp}$  is the content of brown pigments,  $C_w$  is the equivalent water thickness in leaf, and  $C_m$  is the leaf dry matter per unit area [70]. The PROSPECT model have been successfully used for different applications such as leaf parameter inversion from reflectance spectra.

The SAIL family models describe the canopy structure. They assume the canopy as turbid randomly distributed reflective discs. They have different variations with different assumptions, ranging from homogeneous one layer structure to vertically heterogeneous multi-layer canopies. The hot spot effect was added as a function of the ratio of leaf size to canopy height. 4SAIL, developed by Verhoef, is a numerically robust and speed-optimized version in SAIL family.

The 4SAIL model simulates the bidirectional reflectance factor of turbid medium plant canopies by solving four stream radiative fluxes [71]. The 4SAIL model can be expressed as Equation 4.18

$$R_{ROC} = SAIL(refl, tran, LAI, ALA, hotS, \rho_s, \theta_s, \theta_v, \varphi) \quad (4.18)$$

where  $refl$  and  $tran$  are leaf reflectance and transmittance spectra from PROSPECT,  $LAI$  is the leaf area index,  $ALA$  is the average leaf angle or leaf angle distribution function,  $hotS$  is the hot spot parameter describing the ratio between leaf size the canopy height,  $\rho_s$  is the soil reflectance factor, and  $\theta_s, \theta_v, \varphi$  are the sun zenith angle, view zenith angle and relative azimuth angle respectively.

Table 4.4 [70] is a summary of major PROSAIL input variables.

The PROSAIL model has been validated by comparing with in-situ measurements as shown in Figure 4.12. It has also been validated by other radiative transfer models using benchmark simulated crop canopy structures such as RAMI.

The PROSAIL model was adopted for describing the vegetation canopy BRF for different applications in this research.

Model	Symbol	Quantity	Unit
<i>PROSPECT</i>	N	Leaf structure parameter	-
	$C_{ab}$	Leaf chlorophyll content	$\mu g/cm^2$
	$C_w$	Leaf water content	cm
	$C_m$	Leaf dry matter content	$g/cm^2$
	$C_{bp}$	Leaf brown pigment content	-
<i>SAIL</i>	LAI	Leaf area index	-
	ALA	Average leaf angle	degrees
	hotS	Hot spot parameter	( $m/m$ )
	$\rho_s$	Soil reflectance factor	-
	skyl	Diffuse incoming solar radiation	-
	$\theta_s$	Sun zenith angle	degrees
	$\theta_v$	View zenith angle	degrees
	$\phi$	Sun-sensor azimuth angle	degrees

Table 4.4: Main variables of PROSAIL [70].

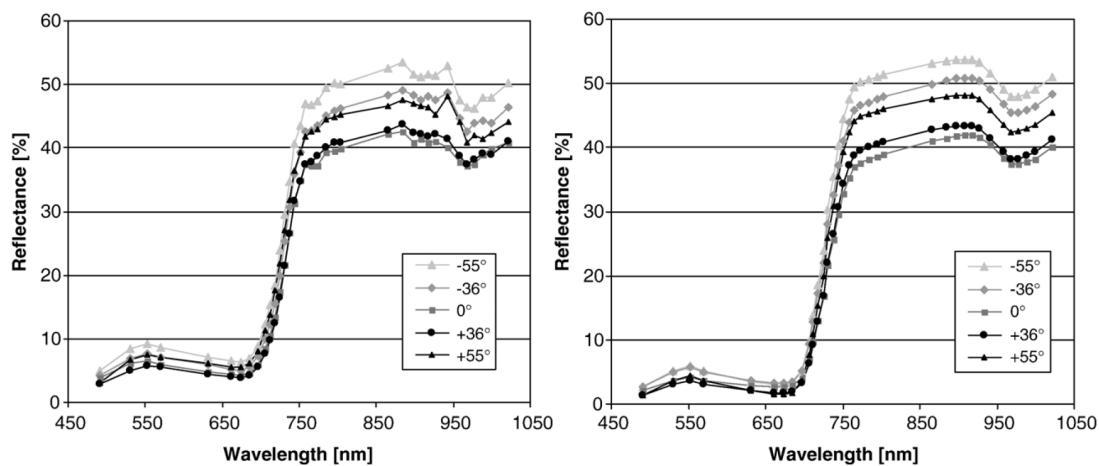


Figure 4.12: Measured (left) and simulated (right) reflectance spectra for maize obtained by CHRIS for 5 observation angles. Date 3 Aug. 2003, solar zenith: 32, relative azimuth: 146.3 (forward looking), 33.7 (backward looking).

## 4.7 Factorial Analysis

In this research, to quantify the significance of different independent variables on dependent variable, factorial analysis was adopted. This section introduces the basic concepts of factorial experiment and analysis.

Factorial experiment is performed by varying all the factors at the same time to provide information about the process variability. The effect of a factor is defined as the change in response produced by a change in the level of the factor. In experiments with more than one factor, interaction effects among more than one factors are possible [74]. For example, in the RSR shift effect research, multiple factors, including the RSR shift effect, contribute to the variation of sensor reaching radiance signal. The factorial experiment is a suitable tool for analyzing the significance (effect) of each factor variation on sensor reaching radiance variation. One special example of factorial experiment is  $2^k$  design. It is a special case of the general factorial design with  $k$  factors each has two possible levels. The two levels of each factor can be either qualitative or quantitative. A complete replicate of such a design requires  $2 \times 2 \times 2 \dots \times 2 = 2^k$  observations. Table 4.5 is an example of the design matrix of a  $2^3$  design, where - and + corresponds to the lower and higher level of each factor (A,B,C). The left column corresponds to the main and interaction effects. In this study it is not difficult to achieve all the factor combination observations since the DIRSIG simulation tool can simulate all possible conditions [74].

When all combination observations are ready, the significance of each factor and each factors interaction can be quantified by fitting them to the fixed effect analysis of variance (ANOVA) model. For example, a three factor (A,B and C) case can be modeled as:

$$y_{ijkl} = \mu + \tau_i + \beta_j + \gamma_k + (\tau\beta)_{ij} + (\tau\gamma)_{ik} + (\beta\gamma)_{jk} + (\tau\beta\gamma)_{ijk} + \varepsilon_{ijkl} \quad (4.19)$$

where  $y_{ijkl}$  is the  $ijkl$ th observation,  $\mu$  is the overall mean of all observations,  $\tau_i, \beta_j, \gamma_k$  are the main effects of  $i$ th,  $j$ th and  $k$ th level of factor A,B and C.  $(\tau\beta)_{ij}$ ,  $(\tau\gamma)_{ik}$  and  $(\beta\gamma)_{jk}$  are the effect of two factors interaction,  $(\tau\beta\gamma)_{ijk}$  is the three factors interaction.  $\varepsilon_{ijkl}$  is the random noise. And the effect (significance) of each factor can be interpreted by dividing the sum

treatment comination	A	B	C
(1)	-	-	-
a	+	-	-
b	-	+	-
ab	+	+	-
c	-	-	+
ac	+	-	+
bc	-	+	+
abc	+	+	+

Table 4.5: Table treatment code of  $2^3$  design [74].

of square variance of all observations as:

$$SS_T = SS_A + SS_B + SS_C + SS_{AB} + SS_{AC} + SS_{BC} + SS_{ABC} + SS_{ERR} \quad (4.20)$$

where  $SS_A$ ,  $SS_B$  and  $SS_C$  represent the sum of squares for the main effects for factor A,B and C.  $SS_{AB}$ ,  $SS_{AC}$ ,  $SS_{BC}$  and  $SS_{ABC}$  represent the sum of squares for the interaction effects between all combination of factors.  $SS_{ERR}$  is the sum of squares for the error [74][40].

Besides, a single dependent variable that depends on several independent variables can also be expressed by a regression model. Especially, it can be expressed by a polynomial model when the inherent functional model is not available, as shown in Equation 4.21

$$y = \beta_0 + \beta_1 x_1 + \beta_2 x_2 + \beta_3 x_1 x_2 + \varepsilon \quad (4.21)$$

where  $x_1$ ,  $x_2$  correspond to the two main factors and  $x_1 x_2$  is the interaction factor. Similar as ANOVA analysis, the effect of each factor can be quantified by the ratio of the sum of squares of each factor to the sum of squares explained by the regression model [40][74].

## 4.8 Summary

This chapter introduced the background information, including the radiometry, land surface anisotropic features and Landsat 8 OLI instrument characteristics. The RSR shift effect was also described since it is a concern for potential wider FOV instrument. Remote sensing based vegetation monitoring applications, especially crop mapping and canopy biophysical quantity retrieval were briefly reviewed, as well as the related algorithms that were used in this thesis. The image simulation tool DIRSIG and the crop canopy BRF model PROSAIL were introduced. They were adopted throughout this thesis for different purposes. Finally, the factorial analysis was briefly introduced and it was used for sensitivity study.

## Chapter 5

# RSR Shift Effect Impacting on Radiance Signal

The primary objective of this chapter is to quantitatively analyze the significance of measured spectral radiance differences due to a relative spectral response (RSR) center wavelength (CW) shift with angles of incidence in Landsat 8 and 9 OLI and future Landsat designs using similar filter technology. In this chapter the interplay between the RSR shift effect, ground surface reflectance characteristics, atmospheric path radiance and ground reaching irradiance has been studied and quantified. The RSR shift effect under various atmospheric types has been studied and compared to the instrument noise. Besides, the impact of RSR shift effect on the NDVI product has also been quantified.

### 5.1 Methodology

This section introduces the details of RSR shift study simulation configurations.



### 5.1.1 View Zenith Angle Determination

To achieve accurate nadir revisit over the same ground point, all sun-synchronized satellites must follow the Keplers equation, which defines the relationship between revisit days, revolutions, and satellite altitude [75]:

$D$ : revisit days

$R$ : revolutions within  $D$  days

Orbit period:  $P = 86400 * \frac{D}{R} [\text{seconds}]$

Equatorial altitude (km):  $h = \sqrt[3]{\mu(P/2\pi)^2} - a_e$

where  $\mu = 398600 \text{ km}^3/\text{s}^2$  and  $a_e$  is earth radius.

The interval distance between adjacent groundtracks (km) is  $\Delta l = 2\pi * a_e/R$

Assuming that the satellite revisit days must be integer, all possible sun-synchronized orbit can be derived following the Kepler equations. Figure 5.1 [75] shows all orbit candidates with repeat cycle no more than ten integral days.

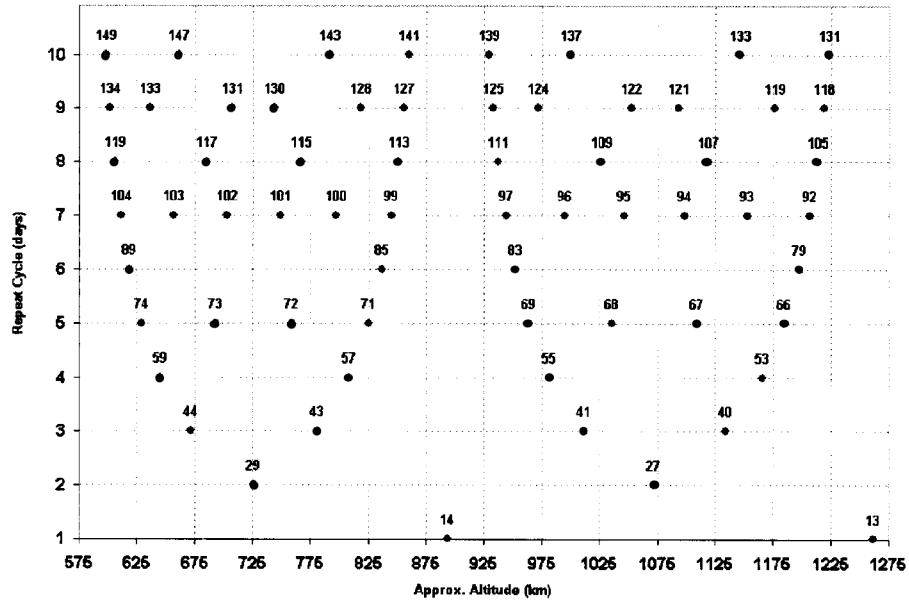


Figure 5.1: Candidate sun-synchronized orbits with no more than 10 days repeat cycle [75].

Since the altitudes of most sun-synchronized satellites are within 680 to 800km, a subset of the candidate orbits are listed in Table 5.1

<b>D</b>	<b>R</b>	<b>h</b>	<b>minimum swath</b>	<b>P</b>	<b>max VZN</b>	<b>FOV</b>
<b>revisit days</b>	<b>revolutions</b>	<b>elevation [km]</b>	<b>interval between adjacent GTs [km]</b>	<b>orbit period [seconds]</b>	<b>[degrees]</b>	<b>[degrees]</b>
9	131	717.09	305.42	5935.88	12.03	24.06
9	130	753.40	307.77	5981.54	11.55	23.10
8	117	694.64	341.96	5907.69	13.84	27.67
8	115	776.32	347.91	6010.43	12.64	25.27
7	102	711.95	392.25	5929.41	15.41	29.28
7	101	758.62	396.14	5988.12	14.64	30.82

Table 5.1: Candidate sun-synchronized orbits with no more than 10 days repeat cycle.

In the simulations of future Landsat satellite, to achieve a higher revisit rate than OLI, an orbit with 7-days revisit rate and 30 degrees field-of-view (FOV) was assumed as the future Landsat satellite orbit. This is a reasonable orbit that has a FOV large enough to restrict a maximum AOI range for future designs. For these reasons, the last row orbit (seven revisit days, elevation=758.62km, FOV=30.82 degrees) in Table 5.1 was selected to set up the DIRSIG simulation configurations.

### 5.1.2 RSR Shift Model

As mentioned in Section 4.3, detector RSR shifts as the angle of incidence (AOI) increases. And the RSR shift can be modeled as Equation 4.8. In this research, the OLI pre-launched RSRs were used as the nadir view detector RSRs in the DIRSIG simulations, as both OLI and future Landsat instruments RSRs. In the simulation, since the maximum AOI was set to be 15 degrees, the amount of RSR central wavelength (CW) shift within AOI range from zero to 15 degrees was calculated according to Equation 4.8 for each band. Figure 5.2 shows the resulting RSR CW shift amount versus AOI. The maximum RSR shift were 5.0nm, 6.2nm, 7.2nm, 7.2nm, 18.7nm and 25.6nm for the six interested bands.

One assumption of this experiment was that the overall RSR profile of each band

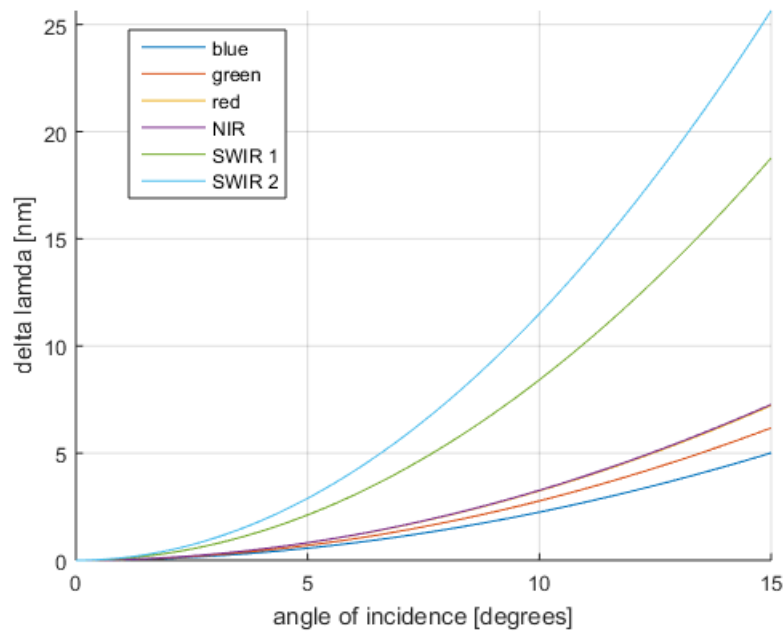


Figure 5.2: RSR shift with respect to AOI.

shift along the spectral axis without shape or magnitude changes. It should be noted that, since the specific future instrument optic design have not been decided yet, the relationship between sensor VZN and detector AOI is assumed to be 1:1 ratio. This may not be true in the real instrument. For example, in the OLI, the sensor VZN in degrees is almost twice of the detector AOI in degrees.

### 5.1.3 DIRSIG Configuration

DIRSIG 4 was used in this study to simulate cross track (XT) spectral radiance signal profiles. In each of the simulations, the inputs for DIRSIG must include platform/sensor geometry, sensor spectral response, atmospheric condition, and ground scene information. Radiometry solvers were also used in the simulation. The details of each of these modules are presented in the rest of this section.

### Platform/Sensor Geometry and Spectral Feature Settings

Landsat 8 OLI has a maximum off-nadir angle of 7.5 degrees. Due to the optical design of the instrument this corresponds to a maximum AOI at the focal plane of approximately 3.5 degrees. To include this as well as possible wider FOV in future Landsat instruments, a cross track scene encompassing a 420 km swath was created. In the simulations, as shown in Figure 5.3, an array with 14,000 detectors was configured to simulate a pushbroom system. The size of each detector, the focal length and the height of the platform were configured so that the ground sample distance (GSD) for the nadir view detector was 30 meters in both along track and cross directions, the same as Landsat-8 OLI.

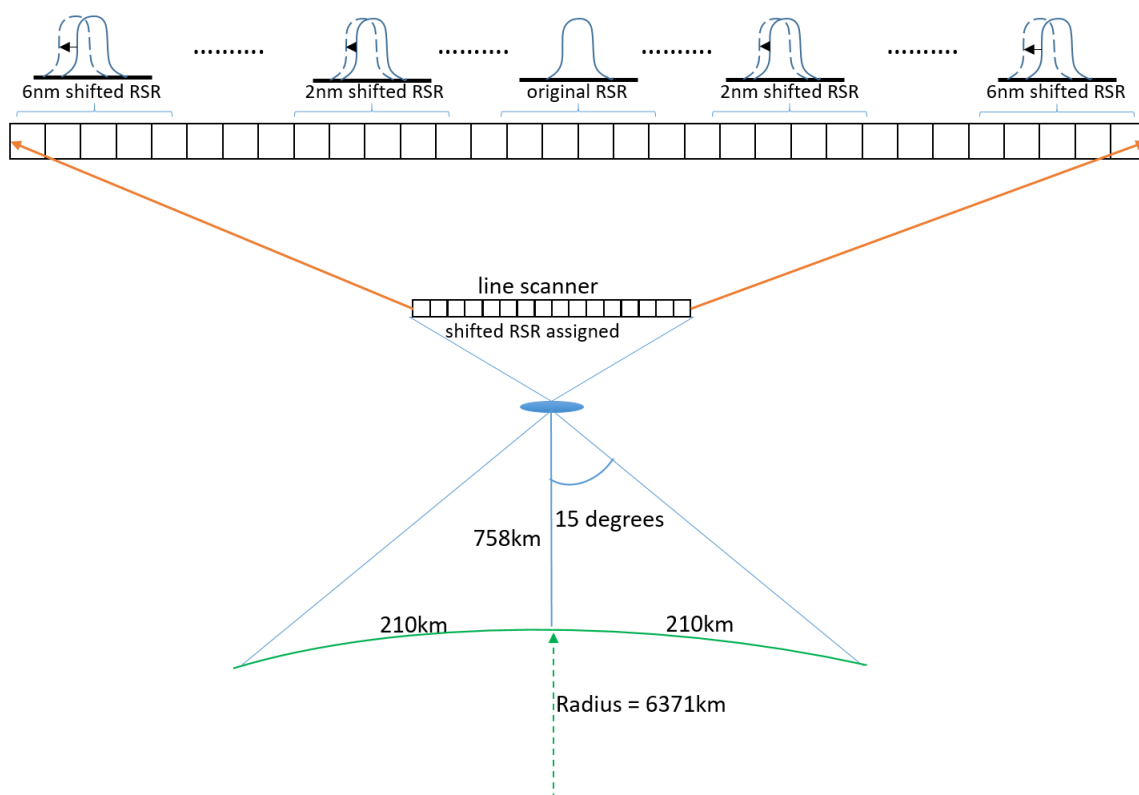


Figure 5.3: Scene and focal plane geometric layout used in the DIRSIG simulation.

Spectral response functions were assigned to the detectors according to the off-axis angle determined by the location across the swath and the shift described by Equation 4.8. In the experiment it was assumed the off-nadir angle of light entering the aperture was the same as the angle of incidence at the filter focal plane. Due to finite spectral sampling in the simulation, it was unnecessary to assign each detector with an exactly shifted RSR profile. In the simulation the minimum RSR shift for red, green, red and NIR bands were set as 0.1 nm and the minimum RSR shift for SWIR1 and SWIR2 bands were set as 0.3 nm, so that the number of possible shifted RSRs and computation time were in reasonable range. Thus, for each band a range of detectors with the same RSR shift were created leading to a stepwise variation across the array.

To produce radiometrically accurate data and to incorporate a realistic point spread function (PSF),  $5 \times 5$  spatial subsampling was adopted in DIRSIG. This means for each spatial pixel 25 points were sampled and convolved with the PSF to produce the at-sensor spectral radiance.

This detector array was modeled on a platform corresponding to the presumed orbit, at 758 km above the ground, and the data acquisition time was set to 11:30 AM, August 3rd, 2015 at a location in western Massachusetts, USA (described below).

### **Atmospheric Settings**

DIRSIG 4 has a suite of interface modules that leverage externally developed atmospheric radiative transfer models such as MODTRAN. The DIRSIG 4 model uses MODTRAN to define the atmosphere as a function of altitude. In this simulations, to study the RSR shift effect under different atmospheric conditions, three atmospheric models were used including the default mid-latitude summer (mls), mid-latitude winter (mlw) and tropical (trop). To keep the spectral resolution in line with the RSR shifting configurations, the MODTRAN output radiance spectral resolution was set to 0.1 nm for blue, green, red and NIR bands and 0.3 nm for SWIR1 and SWIR2 bands.

## Surface Characterization and BRDF Modelling

In DIRSIG 4, the scene file defines the features of the ground surface as viewed by the sensor. In this study, to simplify the simulation geometry, reduce undesired variations, and to isolate the variables of interest, the ground terrain was set to be a perfect sphere with the Earth's radius. The scene origin was set to be at the Harvard forest in Massachusetts, USA (42.5 N, 72.2 W), which is a key area in forest remote sensing studies. The surface elevation was set at a constant.

A reflectance spectrum of a forest top of crown extracted from the JPL ASTER spectral library was assigned to the surface [76]. Figure 5.4 plots the forest spectral along with the six interested Landsat OLI band RSRs.

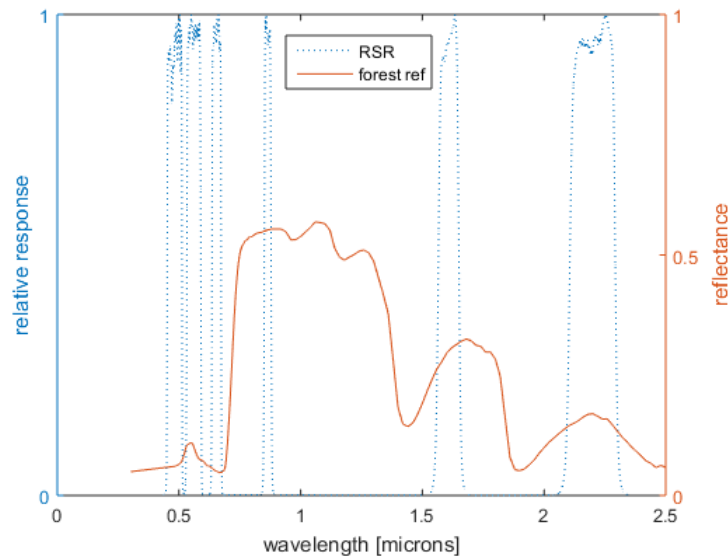


Figure 5.4: Landsat 8 OLI RSR profiles and reflectance spectrum of deciduous forest canopy.

To study the relationship between deterministic RSR shift effect and surface reflectance characteristics, both Lambertian surfaces and surfaces described were considered by a full BRDF model. A Lambertian surface is relatively easy to define and

simulate because it is isotropic. For the BRDF case the Ross-Li model as discussed in Equation 4.2 was adopted.

To define the surface BRDF properties, the three weight factors  $f_{iso}$ ,  $f_{vol}$  and  $f_{geo}$  are described at different wavelength intervals. The MODIS BRDF and albedo product (MCD43A1) can provide high temporal frequency monitoring of Ross-Li coefficients [77]. However, the spectral resolution of this product is low and cannot satisfy the high spectral resolution required to study the fine spectral radiance difference. Rengarajan estimated a set of Ross-Li model weighting factors ranging from 0.45 to 2.31 microns based on DIRSIG simulations [40]. In this study, this set of weighting factors was used as it was verified with real MODIS BRDF data. Figure 5.5 is an example of a DIRSIG derived forest canopy BRDF plot at a wavelength of 0.866 microns.

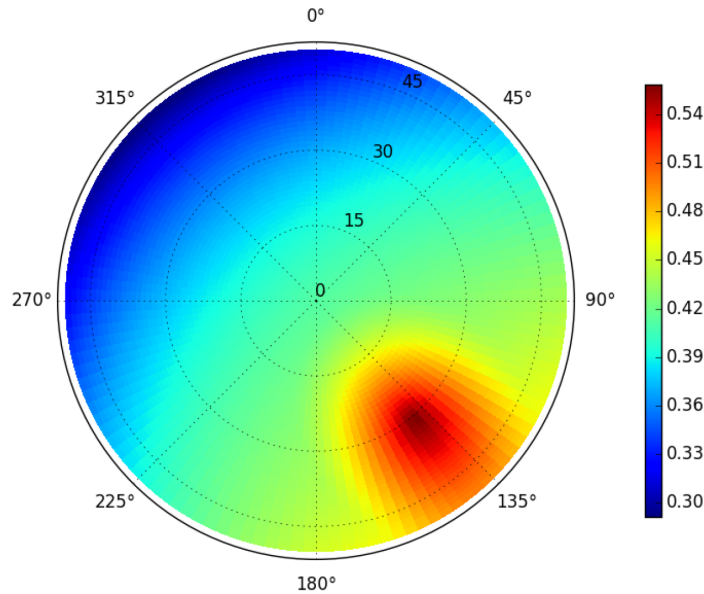


Figure 5.5: Example forest canopy BRDF plot used in simulation [40].

## DIRSIG Radiometry Solver

The DIRSIG radiometry equations are driven by a ray tracer that finds intersections with geometric elements within the scene. DIRSIG provides different radiometry solvers to compute spectral radiance for different scenarios, each with different approximations, different accuracies and resulting computation times. In this study, since we studied the slight signal differences due to shifted RSRs, the DIRSIG Generic Rad Solver (GRS) was selected because it is the most rigorous. GRS uses an importance sampling algorithm instead of uniform sampling over the BRDF hemisphere, which better captures the significant regions of an object and increases the final computation accuracy.

### 5.1.4 Radiance Noise Model

The spectral radiance profiles generated by DIRSIG 4 are without sensor noise. To improve the simulation reality and for further analysis consideration, noise was added to DIRSIG simulated radiance profiles. The noise can be modeled as Equation 5.1 to 5.4:

$$x'(i, j) = x(i, j) + n(i, j) \quad (5.1)$$

$$n(i, j) = \sigma(i, j) * r(i, j) \quad (5.2)$$

$$\sigma(i, j) = \sqrt{s(i, j)^2 + f^2} \quad (5.3)$$

$$s(i, j) = k * \sqrt{x(i, j)} \quad (5.4)$$

where  $x'(i, j)$  is noise added data,  $x(i, j)$  is noise free data,  $n(i, j)$  is noise term,  $r(i, j)$  is normal distribution variable,  $\sigma(i, j)$  is noise variance,  $f$  is fixed noise,  $s(i, j)$  is signal dependent shot noise,  $k$  is shot noise coefficients [78]. To add noise using this model, two parameters  $f$  and  $k$  were estimated for each band. They were estimated by inverting



the noise model with respect to OLI pre-launch SNR performance measurements [79]. For each band the SNR performance was measured at typical and high signal levels. Regression was used to build a signal versus SNR relationship according to the noise model. Figure 5.6 is example of predicted SNR performance over different signal levels, for the blue, green, red and NIR bands.

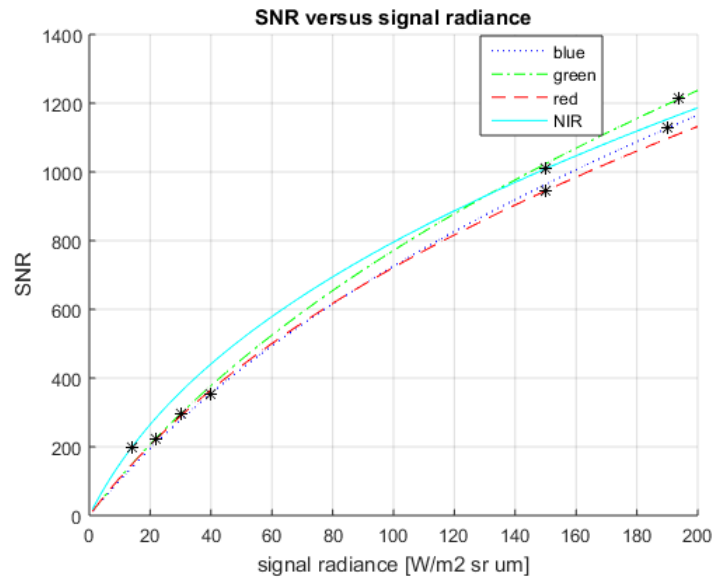


Figure 5.6: Predicted (curves) and measured (points) OLI SNR performance.

## 5.2 Result

This section presents results and discussion analysis showing the impact of the off-axis spectral shift for a variety of parameters. We begin by showing example outputs from the simulation code DIRSIG. Then we compute the correlation coefficients between ideal and shifted RSR radiance signals for the absolute significance of RSR shift in each band. We qualitative study the RSR shift effect interplay with different components in the radiometric image formation chain, and quantify the relative significance of RSR shift

effect comparing with other factors for each band. Then we show the impact on the shift-induced radiance difference of different atmosphere. The difference is also compared to the instrument noise level and its impact on NDVI presented.

### 5.2.1 DIRSIG Output Analysis

#### Smoothing of Local Variance due to Discrete Simulation

In theory the DIRSIG simulated spectral radiance profile should be smooth. However, due to the finite approximations used in the simulation including spatial sub-pixel sampling, quantization of the BRDF reflectance calculation and GRS discrete importance sampling over the hemisphere, a local variance is observed.

Figure 5.7 presents for the green spectral band example cross-track spectral radiance profiles. The cyan curve is an example of noise-free DIRSIG output that shows this local variance. To evaluate if this DIRSIG intrinsic variation is significant compared to sensor noise, we smooth the noise free profiles using a sliding average filter and calculate the standard deviation of the mean-subtracted residual, then compare it to the additive sensor noise using the model described in Equation 5.1 to 5.4. In Figure 5.7, the yellow curve is the noise added profile, while the black profile is smoothed profile. It is clear that the local variance in the noise free spectral radiance profile is smaller than the noise. Similar conclusions are also observed for the other bands. Table 5.2 shows for all bands the local variance due to the discrete simulation is smaller than the additive noise. Thus, in our analysis and subsequent results shown in this paper, the noise free spectral radiance profiles are all smoothed.

#### Cross Track Spectral Radiance Profiles

Figure 5.8 presents smoothed noise free simulated cross track spectral radiance profiles for all reflective OLI bands studied. Each plot includes the variations of combinations of spectral response functions and surface types. The green profile was simulated using

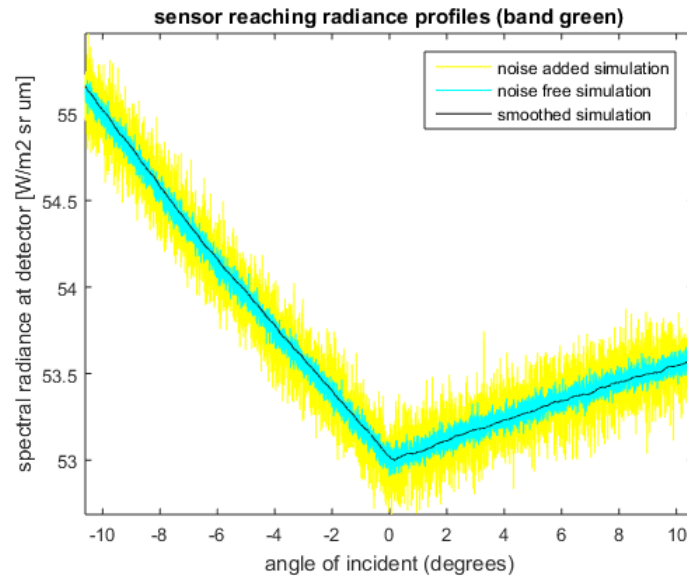


Figure 5.7: Noise added, noise free and smoothed at detector spectral radiance profiles.

Spectral Band	mean signal ( $W/m^2sr\mu m$ )	std ( $W/m^2sr\mu m$ )	noise ( $W/m^2sr\mu m$ )
blue	62.97	0.040	0.123
green	53.68	0.041	0.112
red	29.56	0.020	0.104
NIR	118.14	0.093	0.135
SWIR1	18.52	0.009	0.025
SWIR2	3.37	0.001	0.007

Table 5.2: Mean radiance, standard deviation of mean-subtracted residual, and noise level for each band.

the nadir-viewing uniform RSR with Lambertian ground surface; the yellow profile was simulated using the deterministic off-axis shifted RSR with Lambertian surface; the blue profile was simulated using the nadir-viewing uniform RSR with the Ross-Li BRDF surface; and the red profile was simulated using the deterministic off-axis shifted RSR with the Ross-Li BRDF surface. For this simulation, as determined by the scene location, time, and date of data acquisition selected, the solar zenith angle and azimuth angle are 30.5 and 138.85 degrees, respectively.

These plots demonstrate the interaction between the passband shift as the AOI varies across the swath and the spectral character of the atmosphere as well as the surface. The first observation is the comparatively larger difference between profiles generated using a Lambertian surface and those generated using the BRDF model. These two versions of the surface were simulated to separate out the surface geometric contributions from the spectral contributions.

The second observation is the dramatically different behavior as a function of angle of incidence for the six bands due to the wavelength shift. The blue, green, red, and SWIR2 bands show a significant difference at the high angles when including the wavelength shift, while the NIR and SWIR1 bands show minimal differences due to the shift. This can be explained by the relatively flat spectral radiance curves for the latter two bands while the former four bands are located in spectral regions with more spectral character such as atmospheric absorption features.

### 5.2.2 Qualitative Analysis of the RSR Shift Effect

Quantitatively, Equation 4.1 can be rephrased as Equation 5.5

$$L_{total} = \int_{\lambda_1}^{\lambda_2} [E_g(\lambda) \cdot r(\lambda) + L_u(\lambda)] \cdot RSR(\lambda) d\lambda \quad (5.5)$$

where  $E_g(\lambda)$  is the ground reaching irradiance, including both direct solar and diffuse downwell irradiance.  $L_u(\lambda)$  is atmosphere path radiance. It is obvious that there are

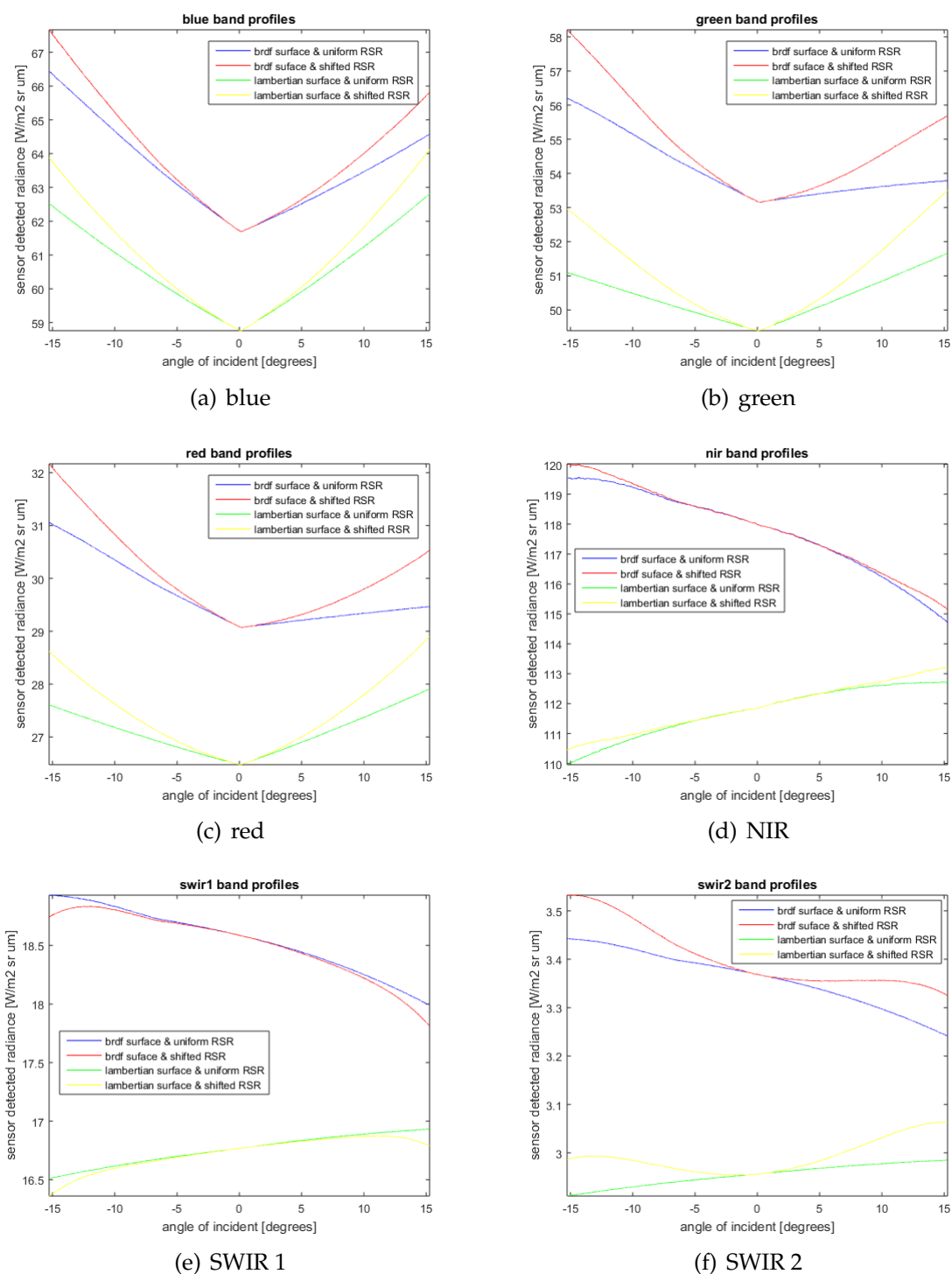


Figure 5.8: Simulated at detector spectral radiance profiles of all bands. In each figure, four profiles are the combinations of two surface types (Lambertian or BRDF) with two RSR types (ideal uniform or shifted)

three terms interplaying with RSR shift: the ground reaching irradiance  $E_g(\lambda)$ , ground BRF  $r(\lambda)$  and atmosphere path radiance  $L_u(\lambda)$ . The interplay between  $r(\lambda)$  and RSR shift can be quantified by calculating the correlation coefficient between uniform RSR and shifted RSR BRF profiles, as shown in the second column of Table 5.3. Band green, red and SWIR 1 have more BRF difference due to RSR shift, which agree with Figure 5.4, these bands RSR cross the forest reflectance spectrum at slope region.

Spectral Band	BRF	Radiance
blue	-0.9871	0.9935
green	0.9934	0.9330
red	0.9154	0.9457
NIR	-0.9982	0.9943
SWIR1	-0.7609	-0.9870
SWIR2	0.9968	0.8678

Table 5.3: Correlation coefficient between uniform RSR and shifted RSR signals (BRF and at detector radiance).

Surface bi-directional reflectance factor (BRF) profiles were also simulated using uniform atmosphere mode simulation in DIRSIG. Uniform atmosphere model in DIRSIG defines the irradiance onto the ground as uniform distributed and there is no atmosphere between target and sensor. When the magnitude of the uniform ground reaching irradiance is carefully selected as the method in [80], the detector signal will be target surface BRF spectrally weighted by detector RSR, instead of radiance signal. The BRF results are shown in Figure 5.9, the upper panel of each figure. The corresponding cross track at sensor radiance signal profiles are plotted in the lower panel of each figure. All profiles were simulated with BRDF surface assumption. Both BRF and radiance signal have two simulations: uniform RSR (ideal) and shifted RSR (real). For each band, the correlation coefficient between uniform RSR profile and shifted RSR profile are computed, for both BRF and radiance. The result is summarized in Table 5.3 as well.

It should be noticed that in Table 5.3 the positive or negative sign in the table only mean the relative magnitude relationship between uniform RSR and shifted RSR profiles:

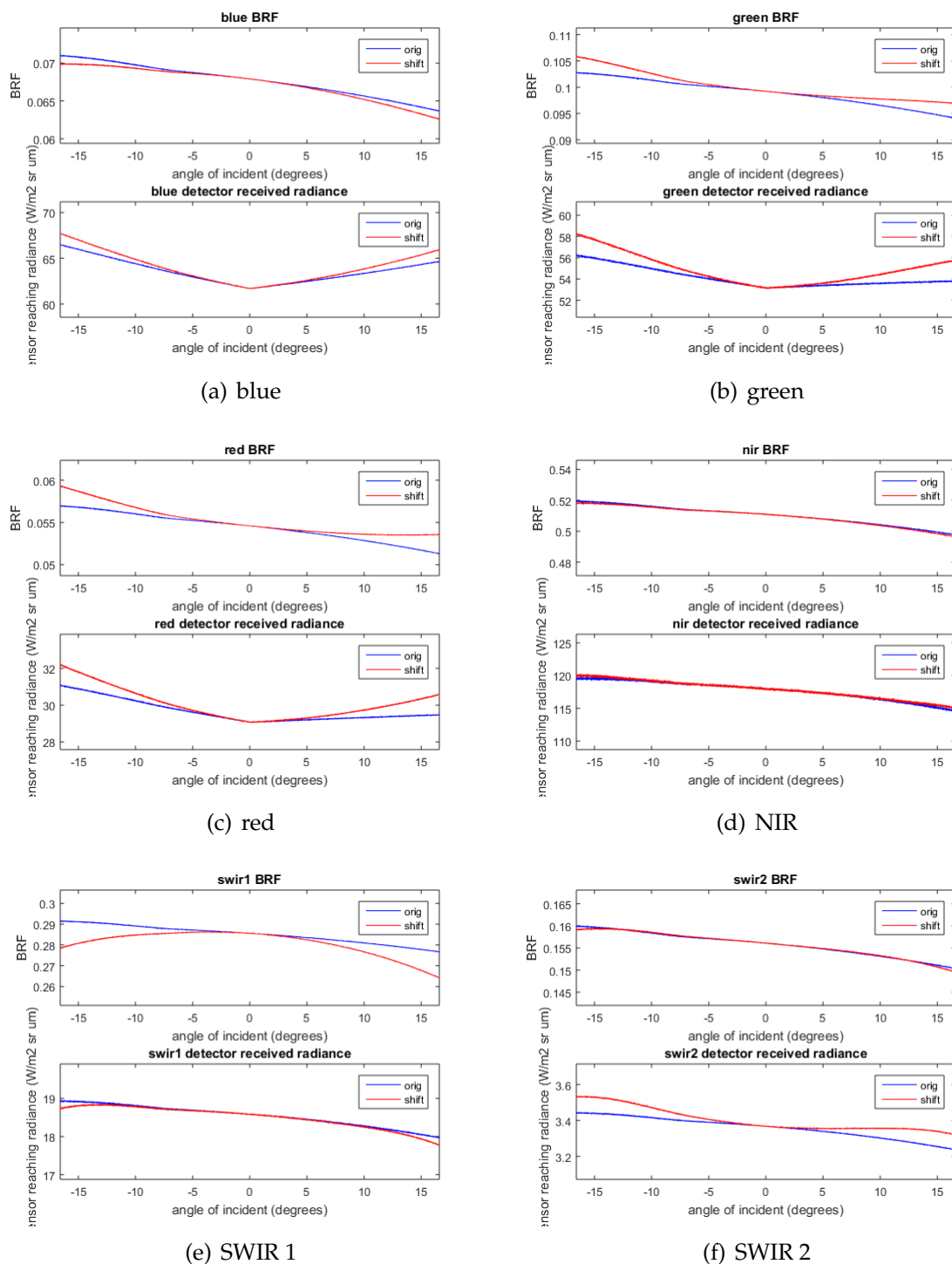


Figure 5.9: Cross track profiles of at detector BRF and at detector spectral radiance (BRDF surface only). Blue is ideal uniform RSR and red is shifted RSR.

positive sign means the magnitude of shifted RSR profile is higher than the magnitude of uniform RSR profile, and vice versa. For each band, the correlation coefficient of radiance signal indicates the absolute significant of RSR shifted effect: a magnitude of correlation coefficient closer to one means the radiance signal is less affected by the RSR shift. Band green, red and SWIR 2 suffer more radiance signal difference due to RSR shift than other bands.

However, after surface BRF  $r(\lambda)$  multiplying the ground reaching irradiance  $E_g(\lambda)$ , the BRF difference can be compensated a lot in band SWIR 1, which is evidenced by the correlation coefficient increase from -0.7609 of BRF to -0.9870 of radiance (atmospheric path radiance  $L_u(\lambda)$  is negligible in SWIR bands, so the correlation coefficient change is only due to the term  $E_g(\lambda) \cdot r(\lambda)$ ). As shown in Figure 5.10, the significant change of correlation coefficient of band SWIR 1 is due to band SWIR 1 RSR crosses the ground reaching irradiance spectrum at an inverse slope region. Similar, for band SWIR 2, after multiplying ground reaching irradiance, the correlation coefficient decreases from 0.9968 of BRF to 0.8678 of radiance. This is because the band SWIR 2 RSR crosses the ground reaching irradiance spectrum at high slope region.

For the visible and NIR bands, since their RSR central wavelength shift amount is not as large as SWIR bands, their  $E_g(\lambda) \cdot r(\lambda)$  term does not change as severely as SWIR bands when RSR shifts. However, since the atmospheric scattering effect is more significant in these bands wavelength range, the radiance signal change due to RSR shift in these bands is more from the atmospheric path radiance change, rather than the ground leaving radiance change.

### 5.2.3 Quantitative Analysis of RSR Shifts Contribution to At-detector Radiance Variation

In this section we use regression analysis to quantitatively understand the relative contribution of each factor to at detector radiance. The factors we analyze include surface model difference (Lambertian or BRDF earth surface), sensor AOI, and RSR shift (uni-



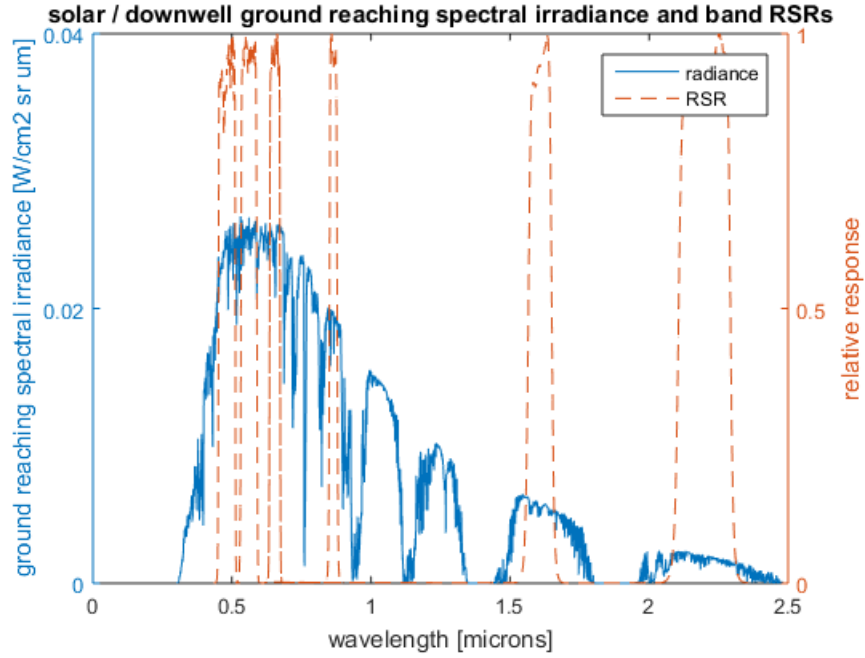


Figure 5.10: OLI RSR and ground reaching spectral irradiance.

form or shifted RSR). At- detector radiance profiles, using either Lambertian or BRDF surface type, and either uniform or shifted RSR, are fitted to a linear regression model Equation 5.6 in least square approach [74].

$$L = \beta_0 + \beta_1 A + \beta_2 B + \beta_3 C + \beta_{11} A^2 + \beta_{12} AB + \beta_{13} AC + \beta_{23} BC + \beta_{111} A^3 + \beta_{112} A^2 B + \beta_{112} A^2 C + \beta_{123} ABC \quad (5.6)$$

where  $L$  is at detector radiance,  $\beta_0$  is intercept of the regression model.  $A, B, C$  corresponds to the three factors we studied:  $A$  is sensor AOI, which is a quantitative factor within the range from 0 to 15 degrees and a step of 0.5 degree;  $B$  is surface model type, which is a categorical factor with value 0 or 1 corresponding to Lambertian or BRDF surface model type;  $C$  is RSR type, which is a categorical factor with value 0 or 1 corresponding to uniform RSR or shifted RSR. The regression model contains both main and interaction

terms and the maximum power of all terms is set to three. Stepwise regression is used in model fitting. Akaike information criterion (AIC) value is used as criterion to add or remove terms from model. When the fitting was done, the contribution or significance of each factor is estimated from the ratio of the sum of squares of each factor to the sum of squares explained by the model [40]. For interaction term, the contribution is evenly divided to the corresponding factors. This fitting is done for each band individually, the  $R^2$  value of the fitting reach 0.99 for all six bands studied. Table 5.4 summarizes the contribution of each factor for six bands.

Spectral Band	surface model	AOI	RSR type
blue	56.9%	41.5%	1.6%
green	79.4%	17.1%	3.5%
red	83.8%	14.2%	2.0%
NIR	98.3%	1.7%	< 0.1%
SWIR1	99.2%	0.7%	< 0.1%
SWIR2	97.6%	1.3%	1.1%

Table 5.4: Contribution of three factors on at detector radiance variation.

It should be noticed that, the numbers in Table 5.4 are the average effect of each factor we studied, which is inherent in the fixed effect model analysis of variance [74]. The purpose of this section is to estimate the significance of different factors, especially RSR shift, in a quantitative way. Also, since the regression is fitted for each band separately, the quantitative contribution values are in a relative sense within each band. They should not be used as absolute values to make cross band comparisons.

From Table 5.4, we can see the RSR shift effect in the NIR and SWIR 1 bands is tiny, which agrees with the small at-detector radiance difference between uniform and shifted RSR profiles of NIR and SWIR 1 bands in Fig 5.9. The relative contribution of the RSR shift in the visible bands is higher, even though their maximum RSR central wavelength shift amount is less than the other bands, as shown in Figure 5.2.

Since surface type is decoupled and analyzed as a separate factor in the regression analysis, the factor AOI is equivalent to atmosphere effects. As shown in the AOI

column in Table 5.4, the contribution of AOI decreases as the band wavelength increases, especially in the visible to NIR range. This is reasonable because more atmospheric scattering in the shorter wavelengths makes the detector view angle difference more significant in these bands. Also, since the BRDF anisotropic effect is more severe as wavelength increases, the difference in surface type assumption (Lambertian or BRDF) is more significant as wavelength increases, which is in line with the trend in the surface type column in Table 5.4. In general, the bands with a comparable significance of AOI (atmospheric path radiance) and RSR type, like band green, red and SWIR2, will be more affected by the RSR shift effect, which is in line with the lower correlation coefficients of these bands in Table 5.3.

#### 5.2.4 RSR Shift Effect For Various Atmospheres

In above sections, the simulations were done using the MODTRAN mid latitude summer (mls) atmospheric model. In this section, three default atmospheric models in MODTRAN (mls, mlw and tropical) were compared to study the significance of the signal difference due to the RSR shift under different atmospheric conditions. All other parameter settings were held constant.

Figure 5.11 is an example for the SWIR2 band. Each profile corresponds to the at detector spectral radiance difference due to the RSR shift for the given atmospheric model. Blue, red and green profiles are for mls, mlw and tropical atmosphere conditions respectively. In SWIR2 case, the difference profiles of mls and tropical are similar, and mlw is higher (about 3.5% versus 2.6%). Table 5.5 summarizes the maximum at detector spectral radiance difference, for future Landsat designs with a maximum AOI equal to 15 degrees, while Table 5.6 presents comparable values for the Landsat-8 OLI, which has a maximum AOI equal to 3.5 degrees.

As can be seen in Table 5.5, when the AOI is as large as 15 degrees, the magnitudes of radiance difference are very different for the six bands: SWIR1 and NIR bands have relatively small differences. This observation aligns with the Teillet et al conclusion that

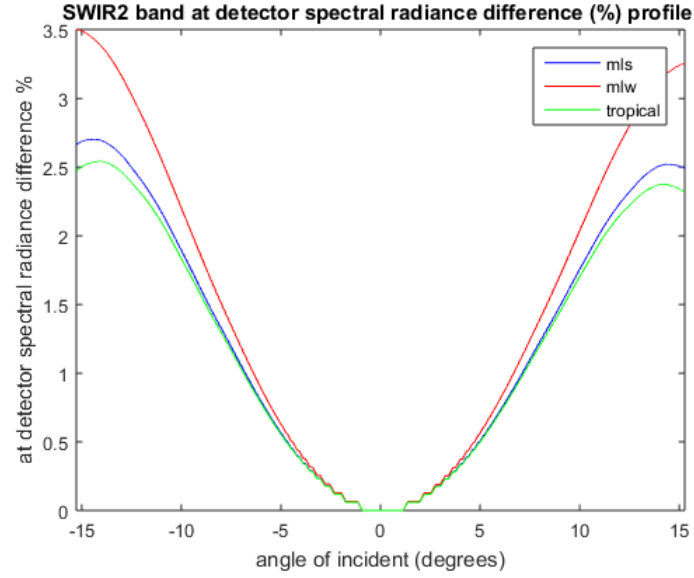


Figure 5.11: Spectral radiance difference profiles of SWIR 2 band under different atmospheric conditions.

Band	mls	mlw	tropical
blue	1.95%	1.93%	1.92%
green	3.70%	3.61%	3.73%
red	3.75%	3.80%	3.82%
NIR	0.40%	0.82%	0.20%
SWIR1	0.99%	0.84%	1.03%
SWIR2	2.70%	3.50%	2.54%

Table 5.5: Maximum at detector spectral radiance difference due to RSR shift for three atmosphere conditions (future Landsat, max AOI = 15 degrees).

Band	mls	mlw	tropical
blue	0.11%	0.11%	0.11%
green	0.24%	0.22%	0.25%
red	0.24%	0.24%	0.24%
NIR	0.01%	0.02%	0.01%
SWIR1	0.02%	0.02%	0.01%
SWIR2	0.29%	0.32%	0.28%

Table 5.6: Maximum at detector spectral radiance difference due to RSR shift for three atmosphere conditions (Landsat 8 OLI, max AOI = 3.5 degrees).

NDVI is more sensitive to the spectral location of the red band than the location of the NIR band [15]. The green, red and SWIR 2 bands have relatively higher differences. Comparing the values in each row, we see a very modest sensitivity to the RSR shift across the different atmospheres. The SWIR2 band is the most sensitive to atmospheric differences compared to the other bands, which we observe when comparing the change in the mid-latitude winter compared to the tropical model result. For the other bands, there is a minimal detector spectral radiance difference due to RSR shift when compared for the different atmospheric models.

Table 5.6 summarizes the impact of the RSR shift for the various atmospheric models for Landsat-8 OLI, with a maximum AOI of 3.5 degrees. In this case, the impact of the RSR shift does not vary significantly for the different atmospheric models.

### 5.2.5 RSR Shift Effect Versus Noise

Instrument noise is always present in satellite observed signals. To assess the significance of the RSR shift effect versus noise, we plot in Figure 5.12 the at detector spectral radiance difference due to the RSR shift alone together with the noise standard deviation as calculated by the model presented in Section 5.1.4. All other system configuration parameters were kept constant. In each plot, the blue curve is the spectral radiance difference due to RSR shift alone and the red profile is the noise level at the corresponding signal level for the band. Any spectral radiance difference lower than the noise limit line is not detectable.

In band SWIR1, the spectral radiance differences are lower than the noise, which is in line with the observations in Sections 5.2.2. In the other five bands, the signal difference due to RSR shift in the near nadir region detectors are lower than the noise. Which means that the RSR shift effect is not detectable for these angles of incidence. However, when the AOI is large enough the spectral radiance difference is higher than the noise and is therefore significant. For each band except SWIR1, the angle of incidence and corresponding detector position off nadir for which the RSR shift effect is detectable is

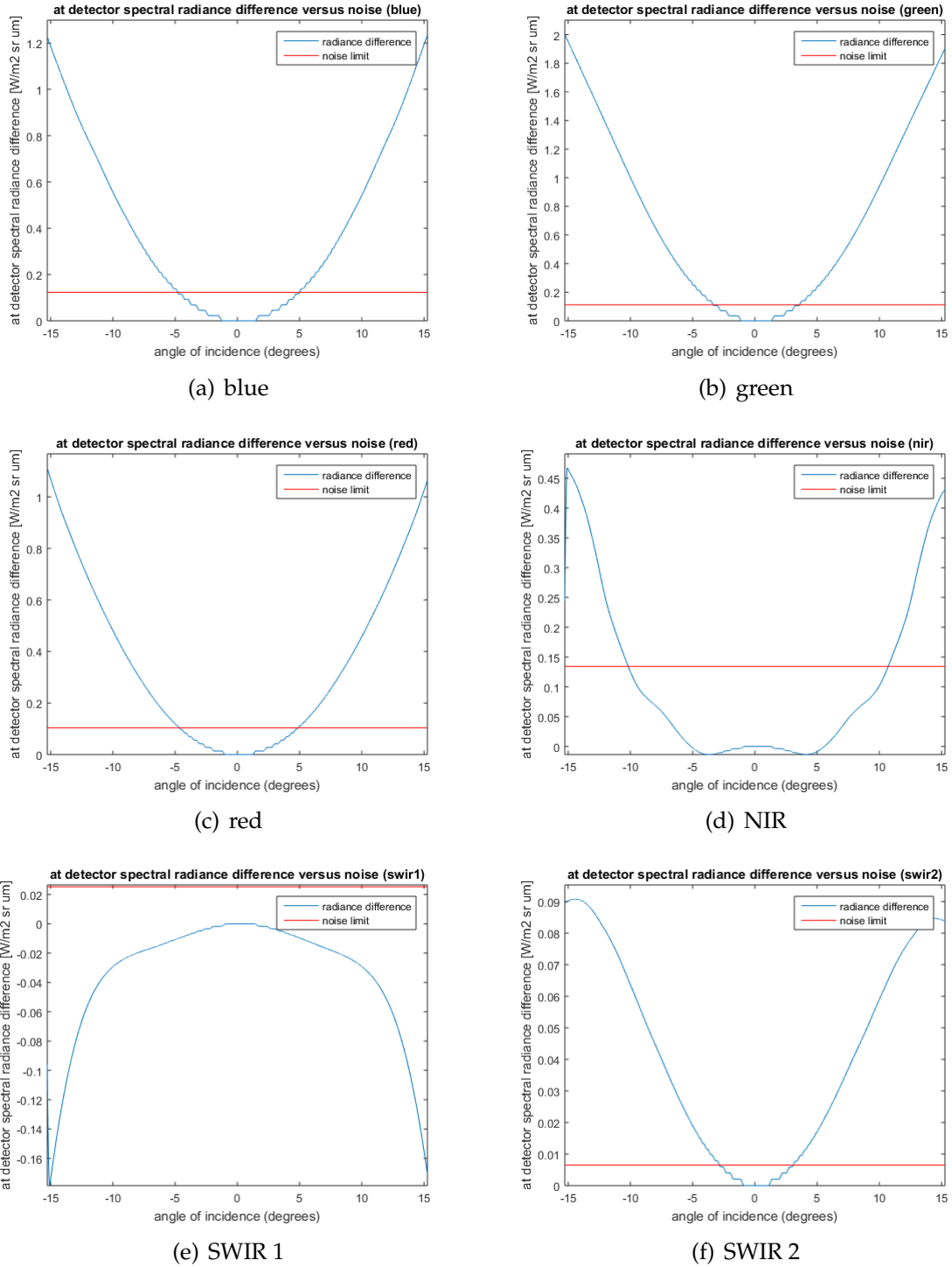


Figure 5.12: RSR shift effect versus noise. For each figure, blue profile is at detector spectral radiance difference due to RSR shift only; red profile is noise limit.

calculated and presented in Table 5.7.

Band	noise level	pixel index off nadir	AOI threshold (degrees)
blue	0.1229	2229	5.04
green	0.1117	1613	3.65
red	0.1036	2170	4.91
NIR	0.1345	4700	10.54
SWIR1	0.0252	N/A	N/A
SWIR2	0.0065	1378	3.12

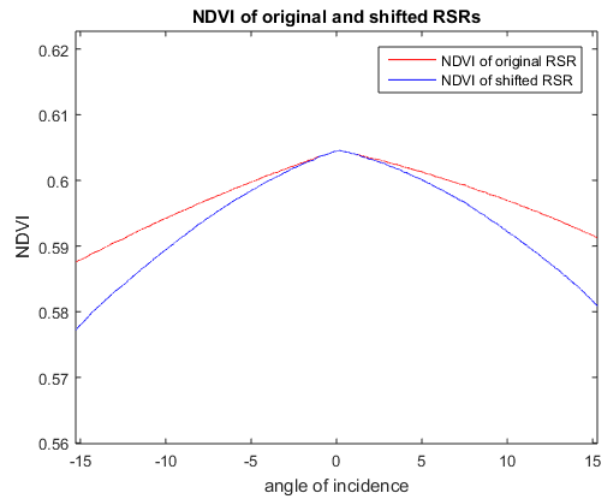
Table 5.7: Noise level and pixel number/AOI threshold where deterministic RSR shift effect exceeds the noise.

As seen in Table 5.7, only the SWIR 2 band AOI threshold is lower than 3.5 degrees. This suggests that for Landsat-8 OLI the RSR shift effect is only noticeable in the far edge of the swath in the SWIR 2 band. For future possible Landsat designs with a large AOI, all bands except SWIR 1 should consider the RSR shift effect when the architecture design has a maximum AOI larger than their thresholds.

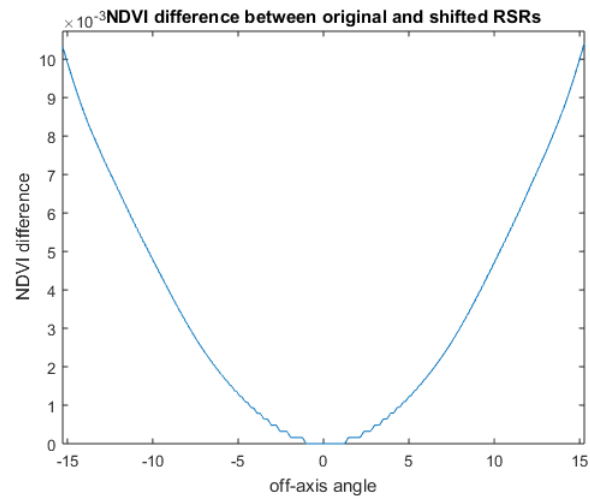
### 5.2.6 RSR Shift Effect Compared to NDVI

The RSR shift effect changes the magnitude of the measured signals in the red and NIR bands which results in a potential change in NDVI as calculated based on TOA radiance values. Figure 5.13 presents NDVI versus angle of incidence using TOA radiance values as well as the percent difference in NDVI due to the wavelength shift. The case here is the default forest spectrum and a midlatitude summer atmosphere. The maximum NDVI difference caused by the deterministic RSR shift is 1.88% for the maximum AOI equal to 15 degrees. The corresponding maximum NDVI difference for OLI is 0.2%.

Since this NDVI difference effect is deterministic for typical vegetation spectra it may be possible to compensate for the change due to the wavelength shift by building a regression model between NDVI and the angle of incidence. We illustrate this procedure by using our simulated data. We assume a quadratic relationship between the shifted



(a)



(b)

Figure 5.13: (a) NDVI profiles of original and shifted RSR (b) NDVI difference due to RSR shift



NDVI and the nadir viewing original NDVI as a function of the AOI  $\theta$ , as shown in Equation 5.7

$$NDVI_o = NDVI_s \cdot (a + b \cdot \theta + c \cdot \theta^2) \quad (5.7)$$

where  $NDVI_o$  is the NDVI for the original nadir-viewing RSR;  $NDVI_s$  is the NDVI for a deterministic shifted RSR;  $\theta$  is AOI; and  $a, b, c$  are the coefficients for the quadratic model. The shifted and compensated NDVI derived from simulated (with noise) spectral radiances are plotted in Figure 5.14. Red points are the NDVI values before compensation and blue points are NDVI after compensation. It is clear that after compensation, the compensated NDVI has been corrected to coincide with the NDVI computed for the nadir-viewing RSRs.

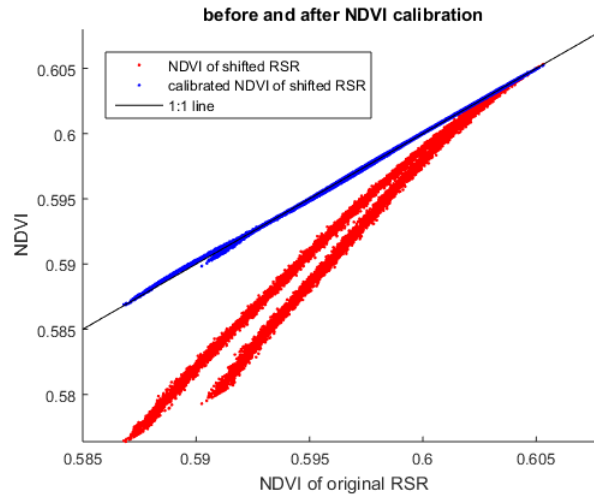


Figure 5.14: Compensation of NDVI affected by deterministic RSR shift effect in mls atmosphere.

Table 5.8 summarizes the results of NDVI compensation for the three atmospheric conditions considered. It shows that the quadratic regression model can significantly decrease the NDVI error due to the deterministic RSR shift.

---

atmosphere	rmse(before)	rmse(after)	a	b	c
mls	0.82%	0.02%	1	1.05E-5	6.97E-5
mlw	0.73%	0.02%	1	1.47E-4	5.78E-5
tropical	0.88%	0.02%	1	7.52E-5	7.75E-5

---

Table 5.8: NDVI regression coefficients for different atmospheric conditions.

### 5.3 Summary

This chapter presented a simulation study on the significance of wavelength shifts in the passbands of Landsat program multispectral filters at large angles of incidence, motivated by the potential for future instruments to acquire imagery across a wider FOV to improve the temporal coverage rate. We computed the correlation coefficients between uniform and shifted RSR profiles and found that the RSR shift effect is more significant in bands green, red and SWIR 2. We studied the RSR shift effect interaction with all components in the radiometric imaging chain. We found that in visible and NIR bands the RSR shift interacting with atmospheric path radiance is the main source of at detector radiance signal difference, and in SWIR bands the RSR shift interacting with surface BRF and ground reaching irradiance is more significant, due to the larger RSR shift in these bands. We quantitatively analyzed the relative relationship between the RSR shift and the impact of ground surface BRDFs as well as atmospheric path radiance, and the polynomial regression study concluded that the RSR shift effect is less significant, both for the current OLI design and future designs incorporating AOIs up to 15 degrees.

In addition, we analyzed the sensitivity of this deterministic RSR shift to different atmospheric conditions, and found that the RSR shift effect is not obviously affected by the atmosphere in Landsat 8 (and 9) OLI. But if future designs include an angle of incidence as large as 15 degrees, then our results suggest the SWIR 2 band may sensitive to atmospheric conditions, making it more difficult to apply compensation methods. We also studied the relationship between the RSR shift effect and the sensor noise. For the

Landsat-8 OLI the RSR shift is only significant in the SWIR2 band. However, for future designs which may have a maximum AOI equal to 15 degrees, our results indicate the impact of the shift will exceed sensor noise in all bands except the SWIR 1 band. Finally we investigated the impact on NDVI from the shift and then explored a method to compensate for the change through the use of a quadratic regression model.

It should be noticed that this study was based on the assumption that the AOI at the detector filter is equal to the AOI at the instrument input aperture. However, for some instrument designs this may not apply. Also, this work focused exclusively on a forest land cover type and all the simulations were set at only one geographic location and acquisition date.

This work has been published in [81].

## Chapter 6

# Impact of Wider Field-of-view Instrument on Vegetation Monitoring Scientific Products

In this chapter the potential impact of a wider field-of-view (FOV) future Landsat instrument on vegetation monitoring scientific products has been quantitatively estimated. Since real dataset within proper angular resolution requirements was not available, synthetic dataset was used in this work. Two aspects of the potential wider FOV instrument have been studied. First, comparing to the existing narrower FOV OLI instrument, whether the wider angular observations (along with the RSR shift effect studied in the previous chapter) would affect application performance. Second, whether the new angular observations are beneficial when used together with other platform data such as OLI. Two important applications, crop classification and vegetation biophysical quantity retrieval have been investigated in this chapter.

This chapter is organized as following: Section 6.1 introduces the research methodologies. Sections 6.2 presents the results of crop classification and leaf chlorophyll content retrieval experiments. Then the conclusions are in Section 6.3.

## 6.1 Methodology

### 6.1.1 PROSAIL Sensitivity Study

Since this study focused on vegetation canopy angular aspects, an accurate description of the canopy bi-directional reflectance factor (BRF) was necessary. The PROSAIL canopy radiative transfer model (RTM) was adopted to characterize the canopy. The PROSAIL model has a large number of input variables. To efficiently sample the RTM input variable distributions, an experiment was conducted to study the sensitivity to BRF of the PROSAIL input parameters. This study adopted a two-level factorial design approach as introduced in section 4.7: each key variable was set to have two levels: high(+) and low(-) that span the potential range. A complete combinatorial study of all levels of all  $k$  variables studied required  $2^k$  PROSAIL runs. Based on the assumption that the response is approximately linear over the range of the selected factor levels, the effect of each factor can be estimated from those  $2^k$  observations. It should be noted that only the direct contribution of each factor was analyzed, and the interactions between different factors were ignored. The resulted 1nm spectral resolution sensitivities, which is as shown in Figure 6.1, were then convolved with the six OLI band RSRs. The resulted band specific PROSAIL input variables sensitivities are as shown in Figure 6.2.

From Fig 6.1, it is obvious that leaf chlorophyll was more sensitive in the visible bands, canopy LAI was more sensitive in the NIR and the SWIR2 bands, and water content was more sensitive in the SWIR1 band. In this study, the model input variable ranges presented in [60] were adopted to determine the PROSAIL input variable ranges. The sensitivity results presented above were used as well to determine the input variable distributions: more samples for the input variables with higher sensitivity. Table 6.1 summarizes the PROSAIL model input variables distributions.

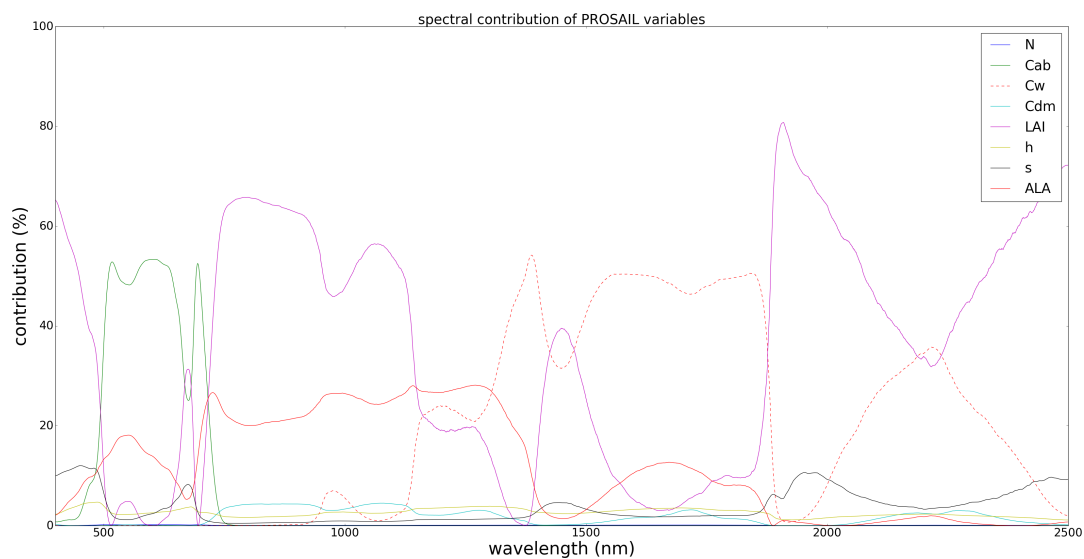


Figure 6.1: Input variables sensitivity to the PROSAIL model (1nm spectral resolution).

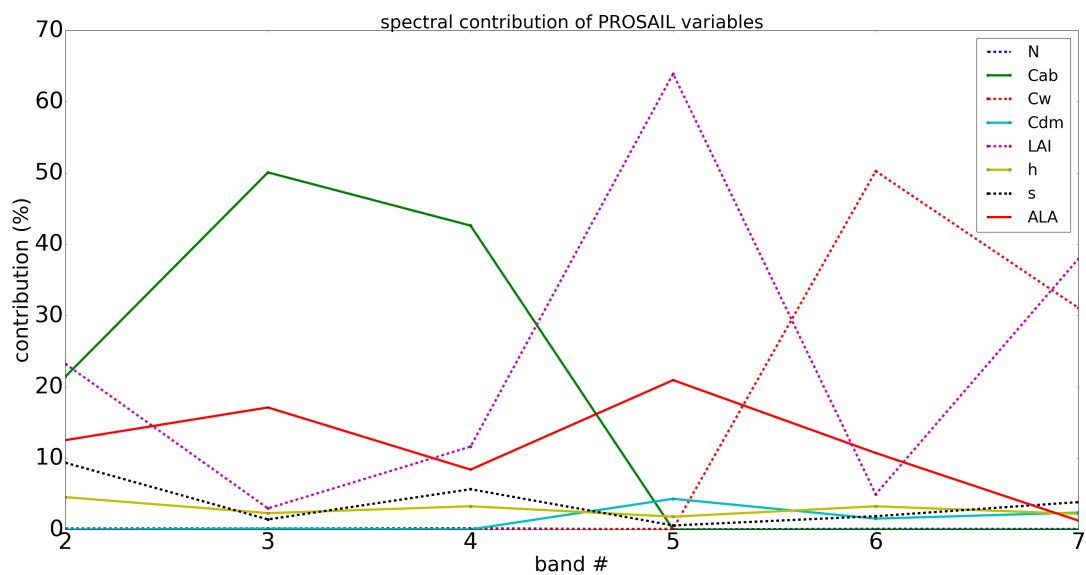


Figure 6.2: Input variables sensitivity to the PROSAIL model (within OLI bands).

Variable	Unit	Sugarbeet	Sunflower	Alfalfa	Potato	Natural Vegetation
$N$	-	1.6	1.6	1.7	1.6	1.5
$C_{ab}$	$\mu g/cm^2$	[42,48]	[40,46]	[46,52]	[32,38]	[20,50]
$C_{bp}$	-	0	0	0	0	0
$C_w$	$cm$	[0.03,0.06]	[0.03,0.06]	[0.012,0.016]	[0.02,0.03]	[0.005,0.02]
$C_m$	$g/cm^2$	0.0065	0.0075	0.0055	0.0045	0.005
$LAI$	-	[0.1,6.0]	[0.1,6.0]	[0.1,6.0]	[0.1,6.0]	[0.1,6.0]
$ALA$	-	[-0.2,0]	[0.7,0.9]	[0.8,1.0]	[-0.38,-0.3]	0
$HotS$	-	0.45	0.15	0.08	0.15	[0.05,0.15]
$\rho_s$	-	0.1	0.1	0.1	0.1	0.1
$\theta_s$	$degree$	30	30	30	30	30
$\theta_v$	$degree$	[-15,15]	[-15,15]	[-15,15]	[-15,15]	[-15,15]
$\varphi$	$degree$	0	0	0	0	0

Table 6.1: PROSAIL input variable distribution for crop classification and crop parameter retrieval tasks [60].

### 6.1.2 BRF Noise Model

Since vegetation parameters are often retrieved from data that have been compensated to surface reflectance, realistic noise was directly added to the PROSAIL generated top-of-canopy (TOC) BRF signal directly in canopy biophysical quantity retrieval experiments. This realistic noise was added as in Equation 6.1:

$$BRF_{noise} = BRF_{noisefree} + N(\mu, \sigma) \quad (6.1)$$

where  $N(\mu, \sigma)$  is Gaussian distribution with mean  $\mu$  and standard deviation  $\sigma$ .

Vermote et al studied the accuracy of OLI surface reflectance products [82]. The comparison was done between ground truth and atmospheric compensated surface reflectance data [82]. For each band, three performance metrics were calculated:

$$A = \frac{\sum_{i=1}^N (\mu_i^e - \mu_i^t)}{N}$$

$$P^2 = \frac{\sum_{i=1}^N (\mu_i^e - \mu_i^t - A)^2}{N-1}$$

$$U^2 = \frac{\sum_{i=1}^N (\mu_i^e - \mu_i^t)^2}{N}$$

where  $A, P, U$  are accuracy, precision and uncertainty, respectively [82].

In this experiment the accuracy and uncertainty measurements summarized in [82] were adopted as the mean and the standard deviation of the surface reflectance noise. In [82], the accuracy and uncertainty of OLI band 2-7 were estimated. Table 6.2 summarizes the BRF noise coefficients [82].

Band	mean $\mu$	std $\sigma$
blue	3.8	8.5
green	2.5	5.4
red	1.7	4.0
NIR	1.4	2.6
SWIR1	0.4	1.1
SWIR2	1.5	3.6

Table 6.2: Surface reflectance noise model mean and standard deviation of six OLI bands studied (expressed in  $10^{-3}$  reflectance).

### 6.1.3 Crop Classification

Since all the simulations were configured as the same sun geometry, the simulated radiance spectra were not atmospherically compensated to surface reflectance. The crop classification was done directly using the at-sensor spectral radiances. Radiances from four different crop species (sugarbeet, sunflower, potato, alfalfa) were simulated. First the TOC BRF samples of each class were generated using PROSAIL model using the range of input variables as listed in Table 6.1. Then with the TOC BRF as input, the instrument received spectral radiance signals were simulated using DIRSIG. For each PROSAIL BRF spectra, the spectral radiance from five different view zenith angles (VZN) ranging from -15 (forward scattering) to +15 (backward scattering) degrees in 7.5 degree increments were simulated. It should be noted that the detector RSR shift effect was considered as well for different viewing angles in the DIRSIG simulations. The sun zenith angle (SZN) was set to 30 degrees for all simulations. Finally realistic noise was added to the spectral radiances following the noise model described in section 5.1.4.



First, the classification was done using single VZN observations only. This was to study the effect on classification accuracy from the wider angular observations (15 degrees) possible in the future wider FOV sensor. The work flowchart is as shown in Figure 6.3.

**Single angular observations based crop mapping:**

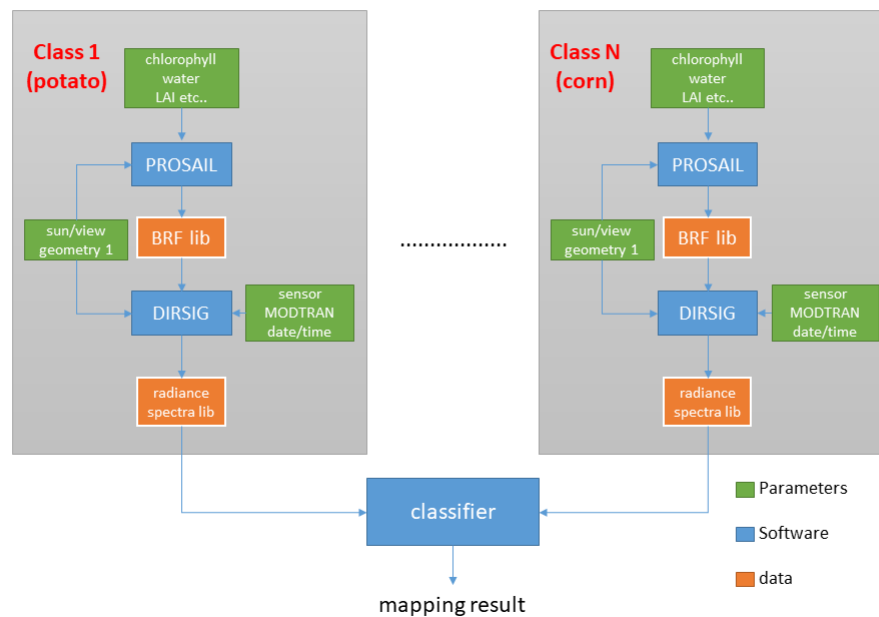


Figure 6.3: Workflow of single VZN observations based crop mapping.

Second the classification was done using all possible pairs of two VZN observations. As shown in Figure 6.4. This was to study the potential benefit to classification performance from using cross-sensor observations. For example, the same ground target may be observed twice: one observation from the future wider FOV Landsat instrument at VZN of 15 degrees and the other observation from Landsat 8 OLI at nadir, respectively. These two observations were assumed within a reasonable time interval so that the ground vegetation condition can be assumed to be constant.

### Multi-angular observations based crop mapping:

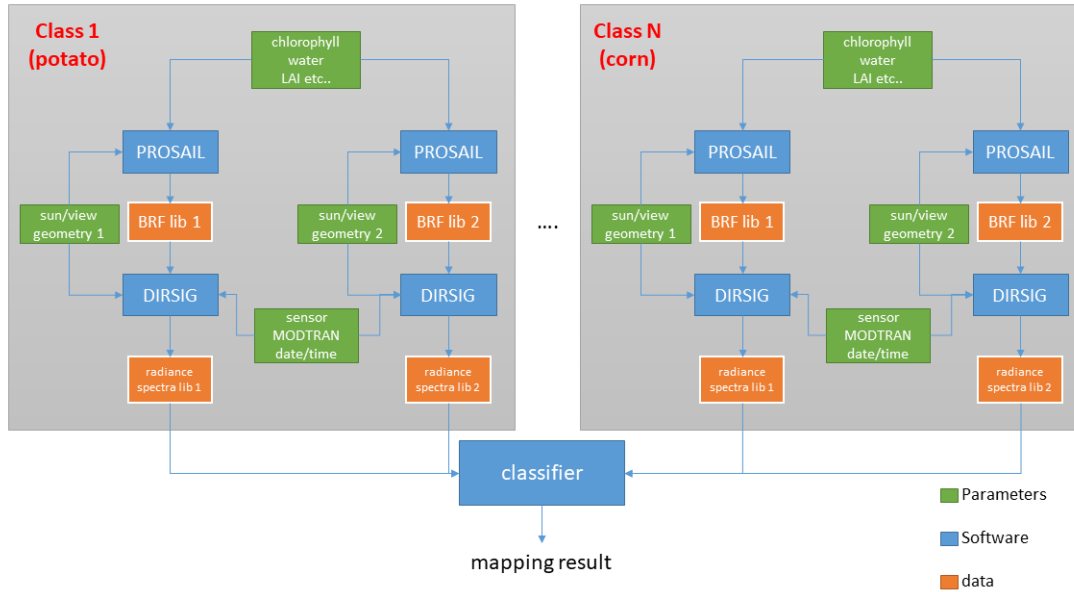


Figure 6.4: Workflow of two VZN observations based crop mapping.

Since the results may be algorithm dependent, four supervised classification algorithms were tested: Linear discriminant analysis (LDA), k-nearest neighbor (kNN), support vector machine (SVM), and decision tree (DT). In both cases of using single VZN observations (6 bands) or using stacked two VZN observations ( $6 \times 2 = 12$  bands), data dimensionality reduction was applied using canonical correlation analysis (CCA). For each algorithm, 20-fold cross validation was used to minimize random effects on classification accuracy from the sampling and added noise.

#### 6.1.4 Canopy Biophysical Quantity Retrieval

In this study leaf chlorophyll content was retrieved from the TOC BRF signal, assuming the data were atmospherically compensated. 1000 test samples were generated using PROSAIL, each with five VZN conditions. The PROSAIL model input variable ranges

followed the natural vegetation species listed in Table 6.1. Realistic noise and atmospheric compensation errors were added directly to the TOC BRF data as described in section 6.1.2.

Two retrieval approaches were studied: look-up-table (LUT) inversion and support vector regression (SVR). We followed the optimal OLI band combination for leaf chlorophyll retrieval as reported in [26]. We used the band combination of red/NIR/green for both approaches. For LUT inversion, similar to the method in [83], a LUT with 100,000 samples was generated. In the inversion process, each test sample was compared to each sample in the LUT. The first 250 LUT samples with minimum RMSE were identified as possible solutions. The mean leaf chlorophyll of this group was then selected as the estimated parameter. In the SVR approach, a radial basis function (RBF) kernel was used. During the SVR training, grid search and cross validation were adopted to estimate the optimal regressor parameters [84]. For both approaches, the retrieval tasks were repeated 10 times to reduce random effects.

Similar as the approach of the classification experiment, first the retrieval was done using each single VZN observations only, and then the retrieval was done using all possible two VZN combination observations. The workflow can be summarized in Figure 6.5.

## 6.2 Results

### 6.2.1 Example of Simulated Data

This section presents the examples of the simulated data used in the study. Figure 6.6 (a) and (b) show the capability of the PROSAIL model to generate the angular variate BRF signal. In each subfigure, the five spectras correspond to the same ground BRF spectra observed from five different VZNs. The angular variation is obvious in both perpendicular (a) and principle (b) planes.

Figure 6.7 presents the high spectral resolution (1nm) BRF spectra libraries of the four

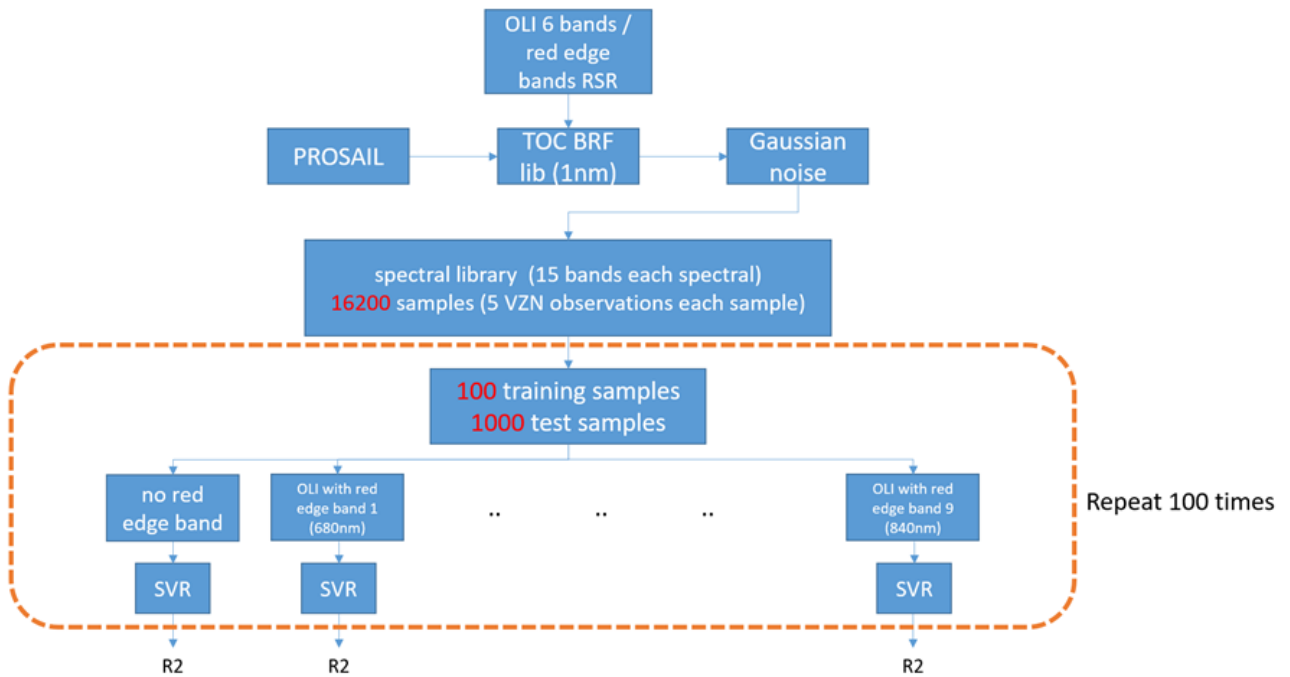
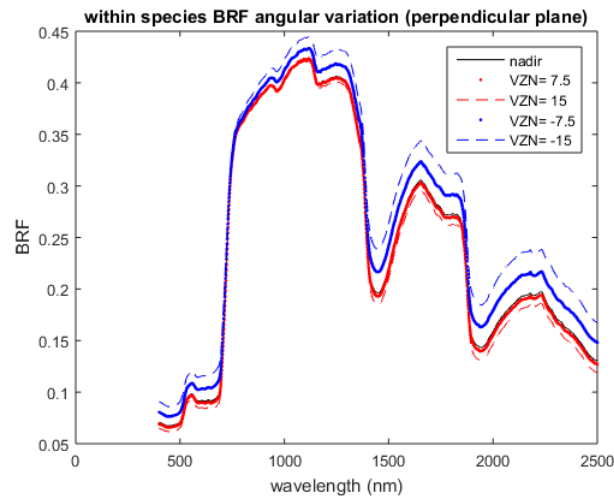


Figure 6.5: Workflow of crop canopy biophysical parameter retrieval.

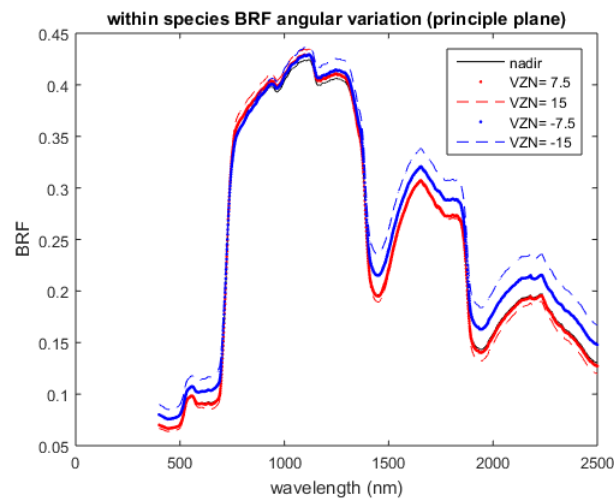
crop species generated from the PROSAIL model. Each library contains the BRF spectra that span the PROSAIL model input variable distribution. The red edge in high LAI samples are prominent and the spectra are more flat for low LAI samples.

Figure 6.8 presents the examples of the at-detector radiance signal libraries of the four crop species. The six interested OLI bands were simulated using DIRSIG 4, with the BRF libraries in Figure 6.7 as input.

The above presented spectra libraries were used in the crop classification and crop canopy biophysical quantity retrieval experiments. And the results are in the following sections.

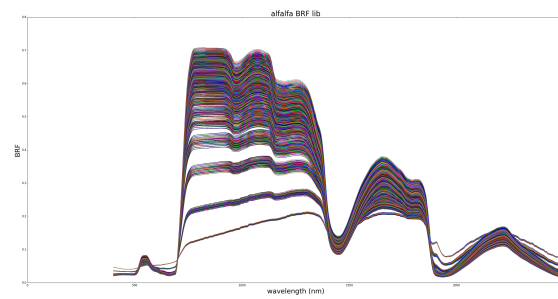


(a) Perpendicular plane.

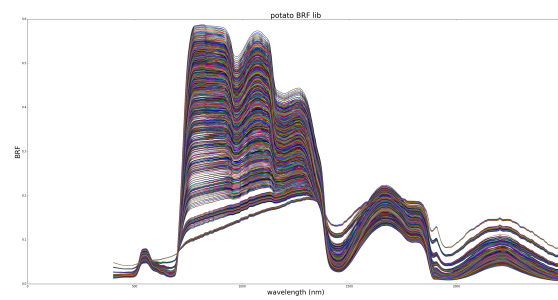


(b) Principle plane.

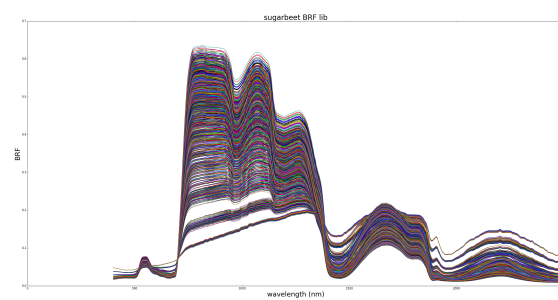
Figure 6.6: Angular variation of the PROSAIL model generated BRF spectra.



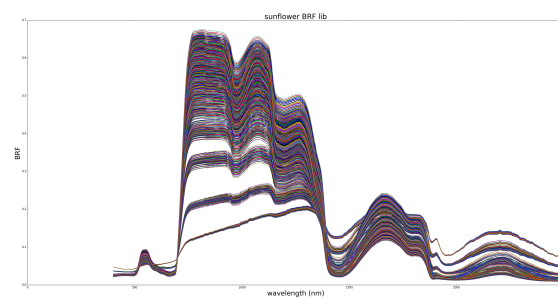
(a) Alfalfa



(b) Potato



(c) Sugarbeet



(d) Sunflower

Figure 6.7: BRF spectra libraries generated using PROSAIL.

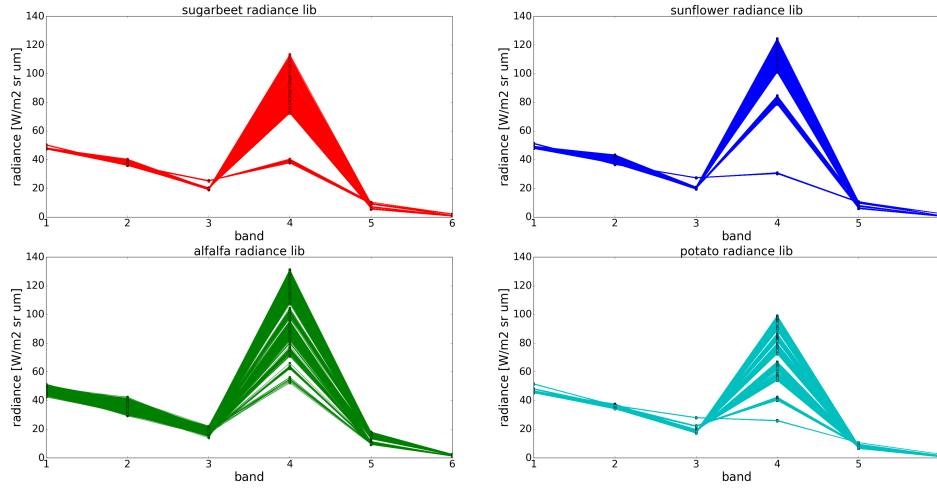


Figure 6.8: Examples of DIRSIG generated at-detector radiance signal.

## 6.2.2 Crop Mapping

The results of single VZN observation based classification are shown in Figure 6.9. The overall classification accuracies of the four algorithms were between 88% and 93%. No significant VZN trend was observed. This does not agree with previous research results. For example, in [24] Galvao et al. studied the atmospheric compensated Hyperion and MODIS data, and in [25] Xavier et al. studied the MISR data. They both found that the classification with backscatter direction data achieved higher classification accuracy. One reason for this difference was the limited off-axis view angle range (15 degrees) considered in this study. In [24] the Hyperion data were acquired at VZN of +21 and -26 degrees and the MODIS data were acquired at VZN of +44 and -42 degrees.

The results of using two angular VZN observations for classification are shown in Figure 6.10. Each subfigure shows the classification accuracy improvement of using the combinations of different two VZN observations, compared to the best classification accuracy case using one single VZN observation. It is clear the accuracy increased significantly for all algorithms, which suggests the multi-directional observations contain

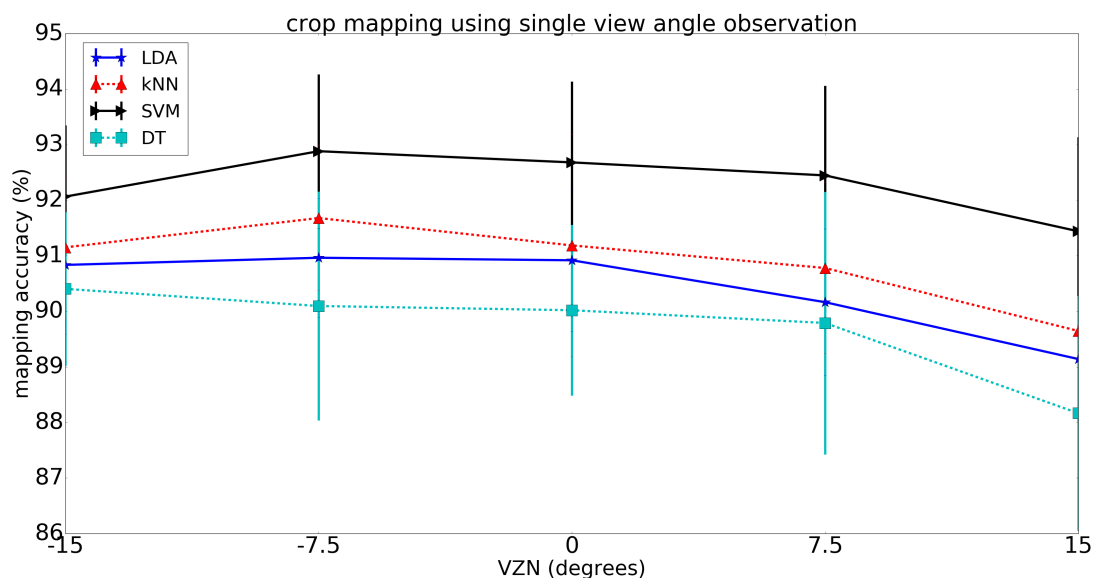


Figure 6.9: Crop classification accuracy using single VZN observations (LDA, kNN, SVM and DT).

useful additional information. This result is consistent with those reported in [85] which used a neural network with ASAS data, in [86] using MISR data, and in [87] which applied a decision tree classifier to POLDER data. In addition, it is obvious that for all algorithms, the highest accuracy improvement were seen for the cases in the lower left corner in each subfigure. In particular, the combinations of (0, +15 degrees) and (0, -15 degrees) increased the classification accuracy by 2.2%, 3.6%, 3.2% and 4.0% for LDA, kNN, SVM, and DT, respectively. This indicates the potential benefits for crop classification when using combination of multiple satellite data (Landsat, Sentinel, etc.) with future wider FOV Landsat observations.



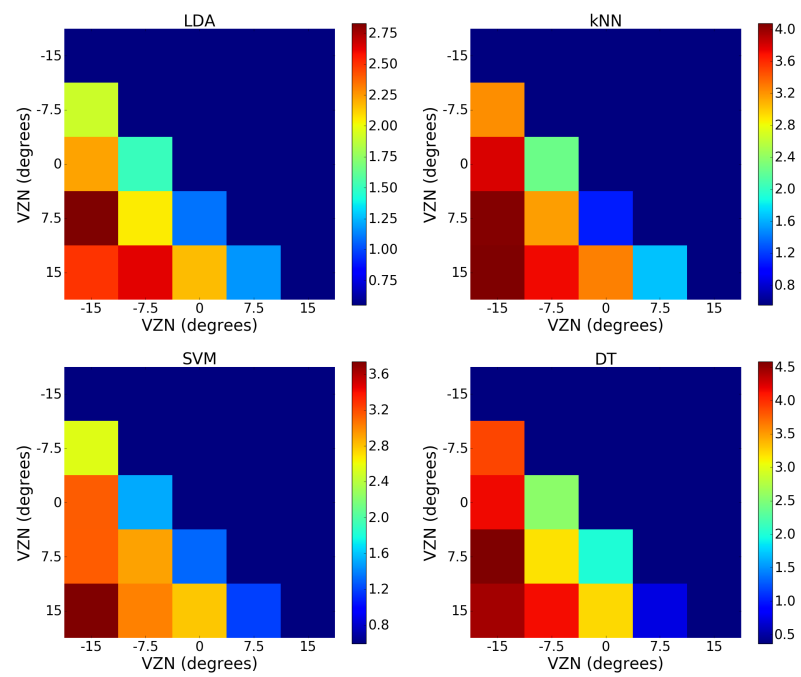


Figure 6.10: Crop classification accuracy improvement (%) using two VZN observation over single VZN observation based accuracy.

### 6.2.3 Crop Canopy Biophysical Quantity Retrieval

The results of leaf chlorophyll content retrieval using single VZN observations are shown in Figure 6.11. For both the LUT inversion and SVR approaches, as the VZN changed from forward scattering to nadir to back scattering, increase in the  $R^2$  correlation were observed. This is reasonable since the backscatter direction data have more canopy illumination than the forward scatter direction and contain more variation. This is in line with the conclusion in [88] that the relative RMSE of retrieved chlorophyll content decreased as the view angle changed from the forward to the backscatter direction.

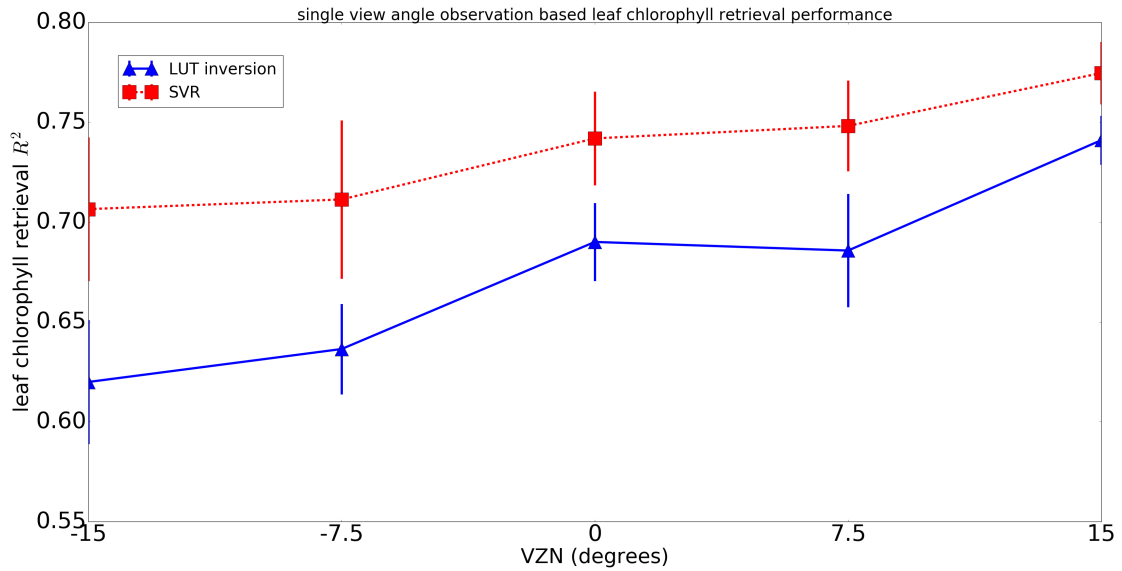


Figure 6.11: Leaf chlorophyll retrieval performance using single VZN observations (LUT inversion and SVR).

The retrieved leaf chlorophyll content improvement (in RMSE) when using two VZN combinations as compared to the best case from a single VZN observation is shown in Figure 6.12. It is obvious that for both LUT inversion and SVR approaches, retrieval with two VZN observations improved the performance. As shown in Table

6.1, the leaf chlorophyll content ranged from 20 to 50  $\mu\text{g}/\text{cm}^2$ . The highest retrieval RMSE improvements for LUT inversion and SVR were 1.0 and 0.7  $\mu\text{g}/\text{cm}^2$ , respectively. Dorigo [88] studied the chlorophyll retrieval performance using CHRIS-PROBA data and concluded that when using the angular combination of -36, 0, 36 and 55 degrees, the relative RMSE dropped 10% comparing to using single VZN data only. In our experiment, this relative RMSE dropped about 2.9%. This is reasonable since our study considered a much smaller VZN range than CHRIS-PROBA.

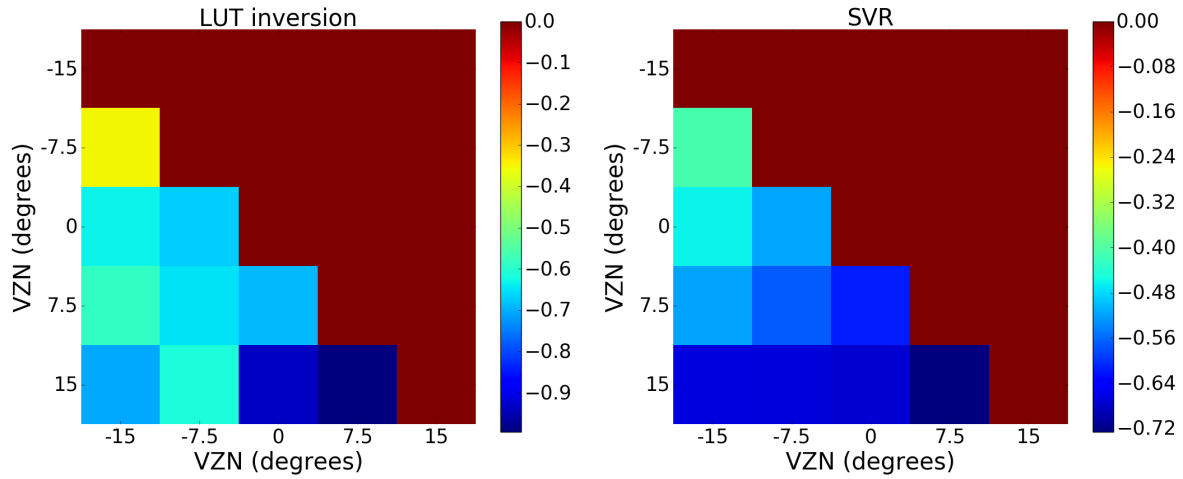


Figure 6.12: Leaf chlorophyll retrieval performance improvement (RMSE) using two VZN observation over single VZN observation based accuracy (LUT inversion and SVR).

### 6.3 Summary

In this chapter the potential impacts of future Landsat instruments with wider FOV design (FOV up to 30 degrees) on vegetation monitoring applications were studied and compared to current Landsat instruments with 15 degrees FOV. Two applications were investigated: crop classification and leaf chlorophyll retrieval.

We studied the performance using single VZN observations to investigate if the new angular data in future wider FOV Landsat instrument would affect the performance. Results showed that neither the +15 nor the -15 degrees observations had a significant effect on the classification accuracy. For leaf chlorophyll retrieval with TOC BRF data, the backscatter direction +15 degrees observations were observed to be beneficial for retrieval performance.

We also studied the performance using all possible two VZN combinations. This represented a scenario using cross-sensor data. The results showed that for both classification and leaf chlorophyll retrieval tasks combining data from two VZNs can improve the performance, especially when +15 or -15 degrees VZN observations were included. The classification accuracy increased by up to 4% and the leaf chlorophyll content retrieval relative RMSE decreased by 2.9% when combining the multi-angular observations. It should be noticed that, to make the simulation more realistic, all the DIRSIG simulations have included the RSR shift effect discussed in Chapter 5.

## **Chapter 7**

# **Potential of Red-edge Spectral Band in Future Landsat Satellites on Agroecosystem Vegetation Canopy Variable Retrieval**

In this chapter, the potential impacts of the addition of new spectral bands in the red-edge region in future Landsat satellites on agroecosystem canopy green leaf area index (LAI) and canopy chlorophyll content (CCC) retrieval have been studied. Besides, the other objective of this chapter is to locate the optimal potential red-edge band position. The chapter is organized as follows. Section 7.1 presents the field campaign dataset used in this chapter, and the related pre-processing procedures. Section 7.2 introduces the methodologies used for LAI and CCC retrieval and the implementation details. Section 7.3 and section 7.4 present the results and discussions for LAI and CCC retrieval, respectively. Section 7.5 is the summary.

## 7.1 Dataset and Preprocessing

### 7.1.1 SPARC '03 dataset

The experimental dataset used in this study is the Spectra bARrax Campaign (SPARC 03) dataset [89], a field campaign organized by ESA during July 2003, at the Barrax, La Mancha region in Spain. The test area extends 5 x 10 km, and consisted of large flat uniform land-use units [90]. This campaign was aimed at supporting algorithm calibration, validation, development, in support of the Phase-A preparations for the SPECTRA mission, and other instrument designs such as Sentinel-2.

Unlike other researches focusing on one crop species only, the SPARC '03 dataset was an agroecosystem. The dataset included nine different crop types (garlic, alfalfa, onion, sunflower, corn, potato, sugar beet, vineyard, and wheat), different growing stages, and varying soil conditions [91]. Figure 7.1 illustrates the field landuse map, sampling points, and airborne flight lines. The data collection geometry configuration is as shown in Figure 7.2. During the campaign, multiple biophysical parameters including LAI and leaf chlorophyll content (LCC) were measured within 118 20 x 20 m elementary sampling units (ESUs). Each ESU was assigned one LAI value measured with a LiCor LAI-2000 digital analyzer.

During the campaign, airborne hyperspectral HyMap images and CHRIS/PROBA satellite images were acquired. HyMap provided 125 contiguous spectral bands ranging from 450 nm to 2500 nm. Its average spectral bandwidth is 15 to 16 nm for visible, NIR and SWIR1 bands and 18 to 20 nm for SWIR2 bands [92]. The example HyMap RGB images of the field campaign from different flight lines are as shown in Figure 7.3. CHRIS was configured in Mode 1 and provided 62 spectral bands ranging from 400 nm to 1050 nm. Since this study was focused on future Landsat missions that include the SWIR bands, only HyMap data were used. The HyMap radiance data were atmospherically compensated to reflectance and georeferenced by DLR [93].

To keep Landsat mission data continuity, the original OLI spectral band settings were preserved as the baseline and new spectral bands were added on top of it. These HyMap

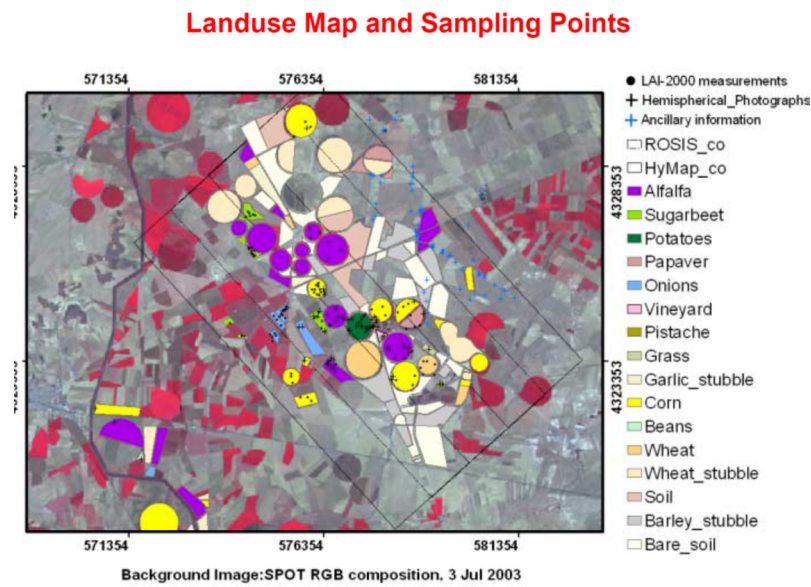


Figure 7.1: SPARC field campaign land use map and sampling points [89].

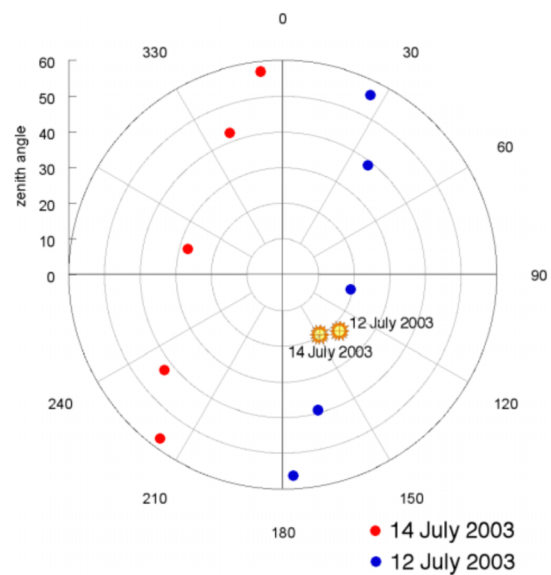


Figure 7.2: The geometry configuration of SPARC '03 campaign data collection [89].

reflectance data were spectrally resampled to Landsat 8 OLI surface sensing bands (blue, green, red, NIR, SWIR1, and SWIR2). And all original HyMap bands within OLI red and OLI NIR bands were preserved as potential new spectral band candidates to be considered for future Landsat instruments. Figure 7.4 plots all spectral bands studied in this study, along with a typical agriculture spectral reflectance.

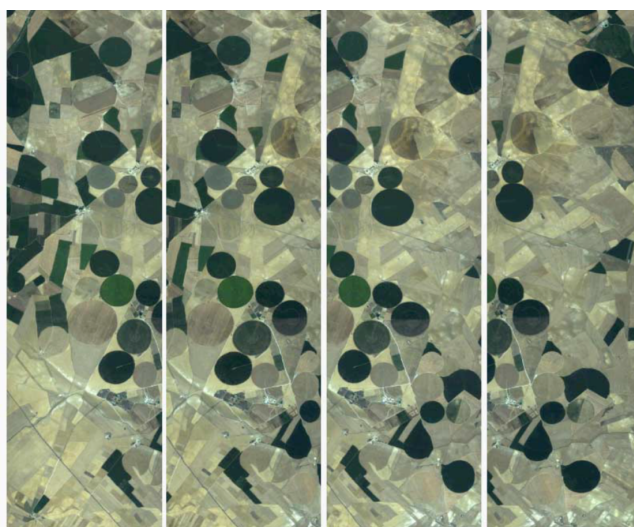


Figure 7.3: Example HyMap RGB images along different flight lines [89].

### 7.1.2 Data Pre-processing

Starting with the 118 ESU samples, first bare soil samples ( $LAI = 0$ ) were removed. Then brown (dry) LAI samples were also excluded by removing all samples with positive green brown vegetation index (GBVI) values as shown in Equation 7.1, where  $R_{2000}$  and  $R_{2100}$  correspond to spectral reflectance at the band centered at 2000 nm and 2100 nm respectively [93]. GBVI is an effective index for identifying the green vegetation samples from others. As shown in Figure 7.5, the green scatters correspond to all green vegetation samples. They all have negative GBVI values. The red scatters with positive GBVI values are brown vegetation samples. Black scatters correspond to the  $LAI=0$  bare soil samples.



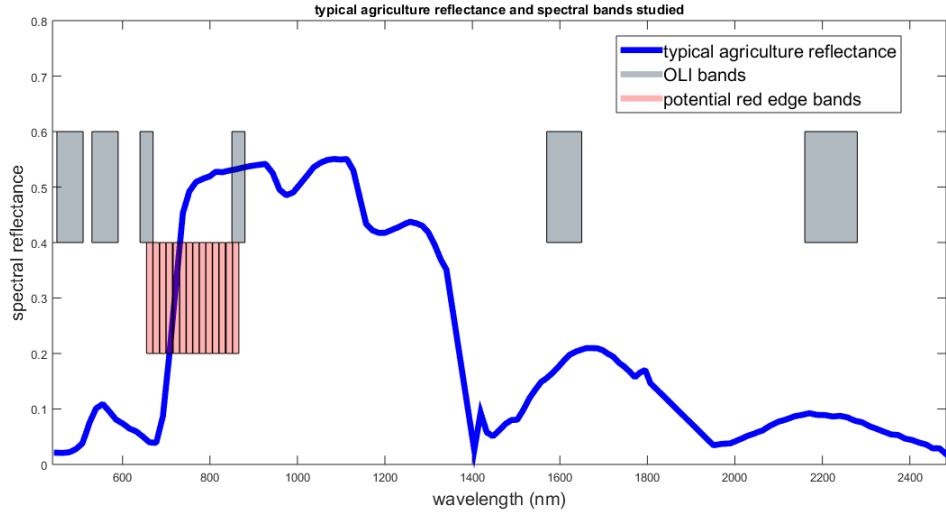


Figure 7.4: Spectral bands studied in this work (OLI bands and potential red edge bands) and typical agriculture spectral reflectance.

The rest blue scatters correspond to the samples without chlorophyll measurements and they were excluded in this study. In the end, 98 samples were preserved for this study. Their spectra are shown in Figure 7.6.

$$GBVI = \frac{R_{2000} - R_{2100}}{R_{2000}} \quad (7.1)$$

## 7.2 Methodology

### 7.2.1 Empirical Vegetation Index Regression Approach

The first retrieval approach tested in this study was the empirical vegetation index (VI) regression approach. Many vegetation indices have been developed for biophysical quantity estimation. Each VI has its specific objective and application scope. Among them, the normalized difference vegetation index (NDVI) has been the most widely used

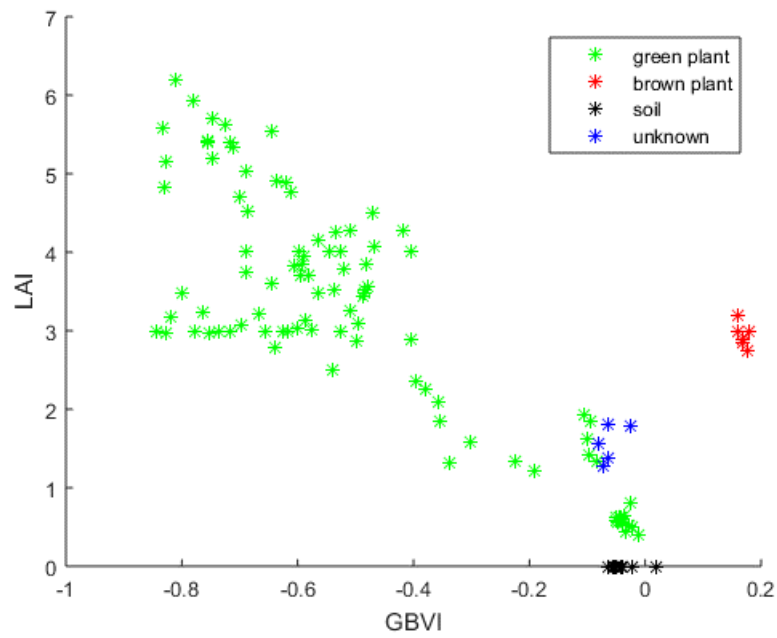


Figure 7.5: The relationship between GBVI and LAI for all 118 SPARC '03 dataset ESU samples.

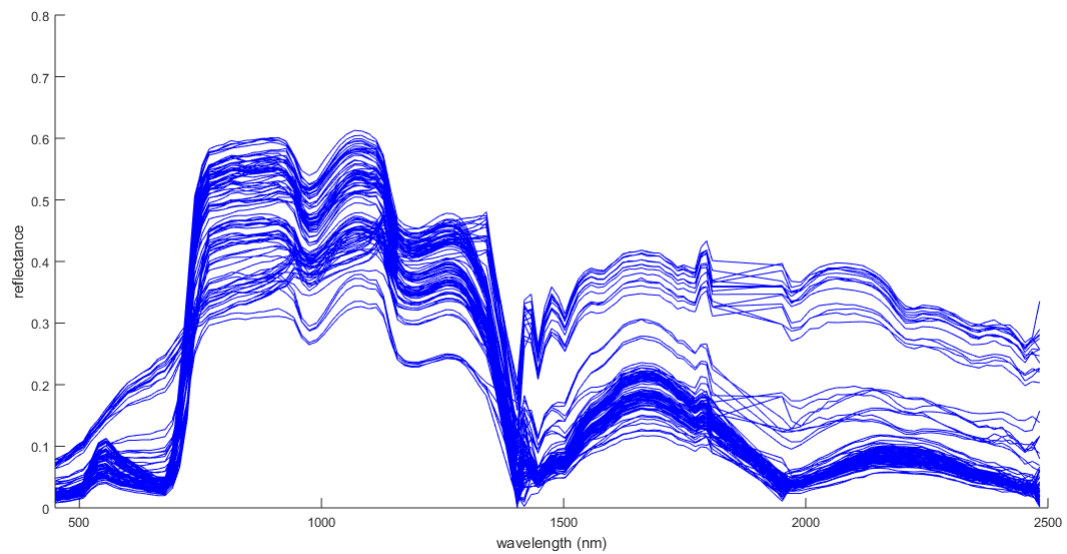


Figure 7.6: The 98 SPARC 03 campaign HyMap spectra used in our study.

due to its simplicity, application to broadband sensors, and compatibility with most operational satellites. The original NDVI was developed to highlight the contrast in spectral reflectance between the red and NIR spectral regions, although the combination of red and NIR bands may not be the optimal index for green vegetation LAI or CCC estimation. In this study, following the approaches in [90] [94] [95], all possible NDVI-like (normalized difference) spectral band combinations, as shown in Equation 7.2, were calculated. Here  $R_a$  and  $R_b$  correspond to the spectral reflectances at bands centered at wavelengths  $a$  and  $b$ . Five-fold cross validation strategy was adopted: each time one fifth samples were used for calibrating the linear relationship between  $NDVI_{a-b}$  and biophysical quantity (LAI or CCC) ground truth, and the rest samples were test dataset for evaluating the retrieval performance. The fitness between the ground truth LAI and predicted LAI were evaluated by  $R^2$ .

$$NDVI_{a-b} = \frac{R_b - R_a}{R_b + R_a} \quad (7.2)$$

Besides  $NDVI_{a-b}$ , chlorophyll index (CI) as shown in Equation 7.3 was also evaluated in this study due to its simplicity and no requirement for soil samples for calculating soil adjustment factors. It was originally developed for chlorophyll concentration estimation by Gitelson et al. [96] [97].

$$CI_{a-b} = \frac{R_b}{R_a} - 1 \quad (7.3)$$

### 7.2.2 Support Vector Regression Approach

In this study, as the second approach, support vector regression (SVR) retrieval was tested to represent a machine learning approach for LAI and chlorophyll retrieval. SVR performs linear regression in the high-dimensional feature space spanned from the original spectral reflectance spectra. It has a good compromise between model complexity and prediction power. Previously, SVR has been successfully used for LAI retrieval [61]. In this study, the radial basis function (RBF) kernel was used. The RBF kernel can

capture the non-linear relationship between input sample dimensions. It has only two free parameters and is easy to tune. During the SVR training process, grid search and cross validation were adopted to estimate the optimal regressor parameters [84].

### 7.2.3 Look-up-table Inversion Approach

The third testing approach was the look-up-table (LUT) inversion approach. Compared to empirical VI approaches or machine learning approaches, the LUT inversion approach does not require training datasets to calibrate the model, which makes it suitable for operational vegetation biophysical variable estimation tasks. The most widely used way to build a LUT is to run radiation transfer model (RTM) simulations. The PROSAIL RTM was used in this study due to its reasonable model assumptions and simplicity. The details of PROSAIL models were introduced in Chapter 4.

In this study, the LUT was generated using MATLAB toolbox ARTMO [98]. The distributions of PROSAIL model input variables were set the same as in [91] as shown in Table 7.1. The input variable distributions covered most ground truth ranges in the SPARC '03 campaign dataset. Also, the soil spectrum required by the SAIL model was represented by the mean of all bare soil sample spectra.

To build the LUT, leaf chlorophyll concentration (LCC) and LAI were randomly sampled 100 times. Each of the other variables was randomly sampled 10 times. All parameter combinations resulted in  $10^{10}$  simulations. To achieve a compromise between good retrieval accuracy and reasonable processing time, as suggested in [83] [26], a random subset of 100,000 sample spectra out of  $10^{10}$  were selected as LUT entries. These spectra were spectrally resampled with respect to the studied bands. Also, as suggested by [91], during the inversion process each SPARC '03 spectra was compared with each entry in the LUT using a Pearson chi-square cost function as shown in Equation 7.4

$$J = \sum_{n=1}^N \frac{(R_n - \widehat{R}_n)^2}{R_n} \quad (7.4)$$

Model Parameters		Units	Range	Distribution
<i>Leaf parameters: PROSPECT-4</i>				
N	Leaf structure index	Unitless	1.3-2.5	Uniform
$C_{ab}$	Leaf chlorophyll content	$\mu g/cm^2$	5-75	Gaussian( $\bar{x}$ : 35, $SD$ : 30)
$C_m$	Leaf dry matter content	$g/cm^2$	0.001-0.03	Uniform
$C_w$	Leaf water content	(cm)	0.002-0.05	Uniform
<i>Canopy variables: 4SAIL</i>				
LAI	Leaf area index	( $m^2/m^2$ )	0.1-7	Gaussian( $\bar{x}$ : 3, $SD$ : 2)
$\alpha_{soil}$	Soil scaling factor	Unitless	0-1	Uniform
ALA	Average leaf angle	Degree	40-70	Uniform
hotS	Hot spot parameter	( $m/m$ )	0.05-0.5	Uniform
skyl	Diffuse incoming solar radiation	(fraction)	0.05	-
$\theta_s$	Sun zenith angle	Degree	22.3	-
$\theta_v$	View zenith angle	Degree	0	-
$\phi$	Sun-sensor azimuth angle	Degree	0	-

Table 7.1: Range and distribution of input parameters used to drive PROSAIL model to generate LUT.

where  $N$  is the number of bands considered,  $R_n$  and  $\widehat{R}_n$  correspond to SPARC sample spectral reflectance and LUT sample spectral reflectance at band  $n$ . The first 500 LUT samples with minimum cost function values were identified as the candidate solutions. Their mean LAI or CCC was selected as the estimated quantity. The mean values of the first 250, 750, and 1000 solutions were also tested and no significant differences from using 500 samples were observed.

## 7.3 Leaf Area Index Retrieval Results

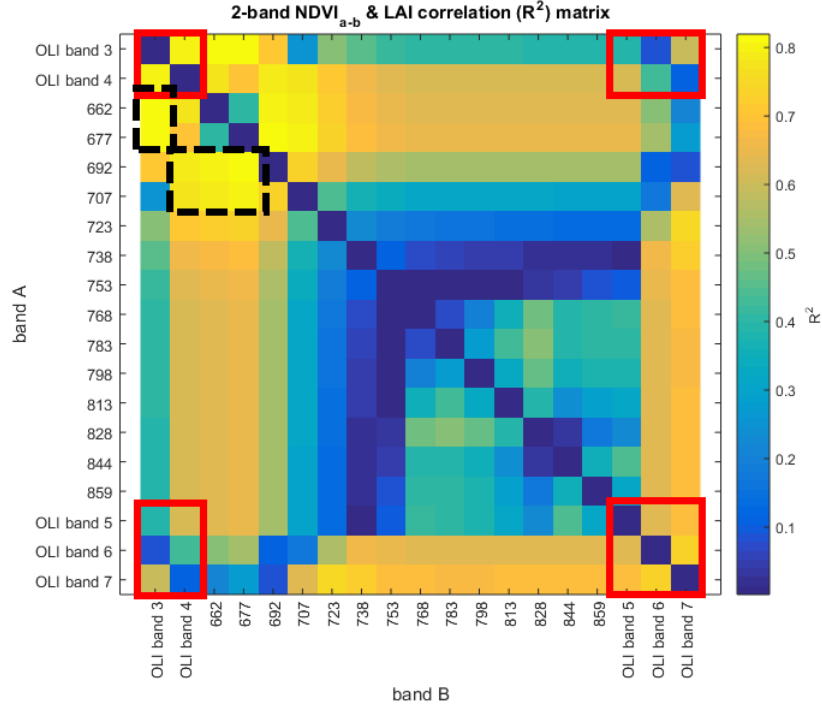
### 7.3.1 Empirical Vegetation Index Regression Approach Result

The LAI retrieval  $R^2$  performance of all possible two-band combination  $NDVI_{a-b}$  are plotted in Figure 7.7. In (a), the red boxes on the corners correspond to the VIs composed with Landsat 8 OLI bands only. The black dashed boxes highlight the spectral band

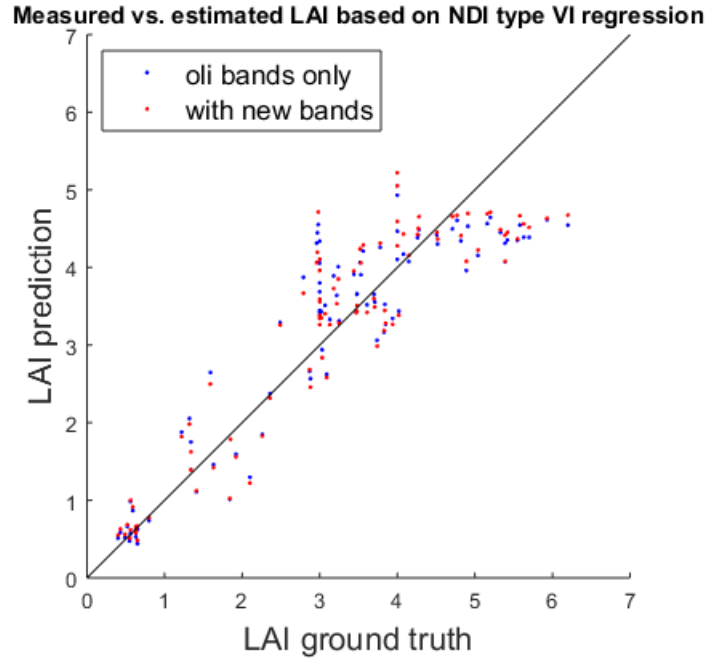
combinations that gave the highest  $R^2$  performance.

The  $R^2$  of  $NDVI_{a-b}$  based on Landsat 8 OLI red and NIR bands ( $NDVI_{655-865}$ ) was  $0.64 \pm 0.05$ . It was not even the optimal band combination when only OLI bands were considered. The  $R^2$  of the combination of OLI SWIR1 and SWIR2 bands was  $0.74 \pm 0.03$ . In [91], Verrelst et al. used the same dataset and tested the relationship between all possible Sentinel-2 band combination VIs and LAI. They found the optimal band combination is Sentinel-2 SWIR1 and SWIR2 bands with  $R^2$  of 0.739. In this study, though similar  $R^2$  was achieved with OLI SWIR1 and SWIR2 bands, the higher  $R^2$  performance was achieved with the combination of OLI green and red bands. One explanation for this could be the difference between Sentinel-2 and Landsat 8 OLI red bands central wavelengths. Even a small central wavelength difference in this sensitive spectral range can cause differences in product retrieval performance.

When potential new bands were considered, two  $R^2$  peaks were observed in Figure 7.7(a). One peak was in the spectral range of 655 – 677 nm and 692 – 707 nm. The optimal band combination in this peak was 677 nm and 707 nm, with an  $R^2$  of  $0.79 \pm 0.07$ . This is very similar to the observation in [90] using the same field campaign data where the optimal  $NDVI_{a-b}$  band combination for LAI retrieval was found to be 674 nm and 712 nm. The only difference is that in [90] the authors used high spectral resolution CHRIS data instead of the HyMap data used in this study and they could study the optimal band combination at a higher spectral resolution. However, they only tested the spectral range between 600 nm and 1000 nm in [90]. In this study, beyond the spectral range studied in [90], a second  $R^2$  peak was found near the green band region containing the overall best performance band combination. The combination of OLI green and 677 nm or 662 nm band resulted in LAI estimation with  $R^2$  of  $0.81 \pm 0.07$ , which was slightly higher than the combination of OLI red and green. This suggests that for agroecosystems, a new spectral band centered near 662 – 677 nm can slightly improve the performance of  $NDVI_{a-b}$  based LAI estimation by a few percent. Figure 7.7(b) shows the scatter plot of LAI estimation based on  $NDVI_{a-b}$ . Blue scatters correspond to the OLI only optimal band combination (bands green and red) and red scatters correspond to the optimal



(a)  $R^2$  between ground truth LAI and  $NDVI_{I_{a-b}}$  for different band combinations



(b) Scatter plot of the predicted LAI versus ground truth LAI. Blue is from the  $NDVI_{655-561}$ , red is from  $NDVI_{561-677}$

Figure 7.7: Result of VI ( $NDVI_{I_{a-b}}$ ) regression approach.

band combination when all potential new bands were considered (bands green and 677 nm). Two observations can be made: (1) the two sets of band combinations performed very similar; (2) similar as reported in previous studies [60] [91], the VI based approach suffered from a saturation effect, which can cause underestimation of high LAI ( $> 5$ ) values.

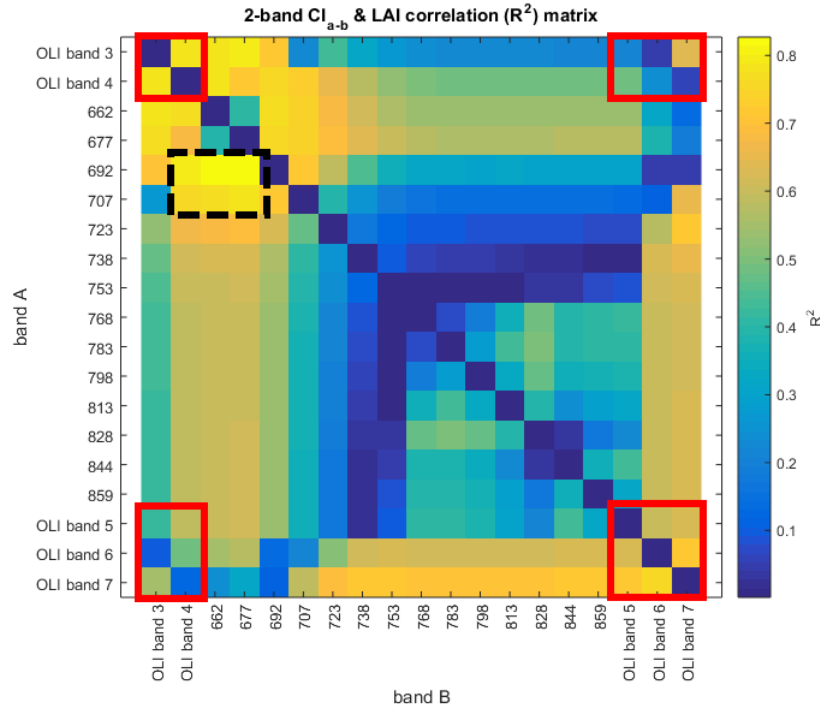
Similarly, the results of all band combinations for  $CI_{a-b}$  are plotted in Figure 7.8(a). When considering OLI bands only, the optimal band combination was OLI green and red bands with  $R^2$  of  $0.77 \pm 0.03$ . When all potential new bands were considered, similar to the  $NDVI_{a-b}$  result, a peak was observed in the 655 – 677 nm and 692 – 707 nm regions. The optimal band combination was found to be 692 nm and 677 nm with  $R^2$  of  $0.81 \pm 0.05$ . The scatter plot of optimal band combination  $CI_{a-b}$  based LAI estimation is shown in Figure 7.8(b). In general, the  $CI_{a-b}$  result was very similar as the  $NDVI_{a-b}$  results: a slight improvement in agroecosystem green LAI estimation was predicted from the addition of a new spectral band between the OLI red and NIR bands in future Landsat instruments.

### 7.3.2 LUT Inversion Approach Result

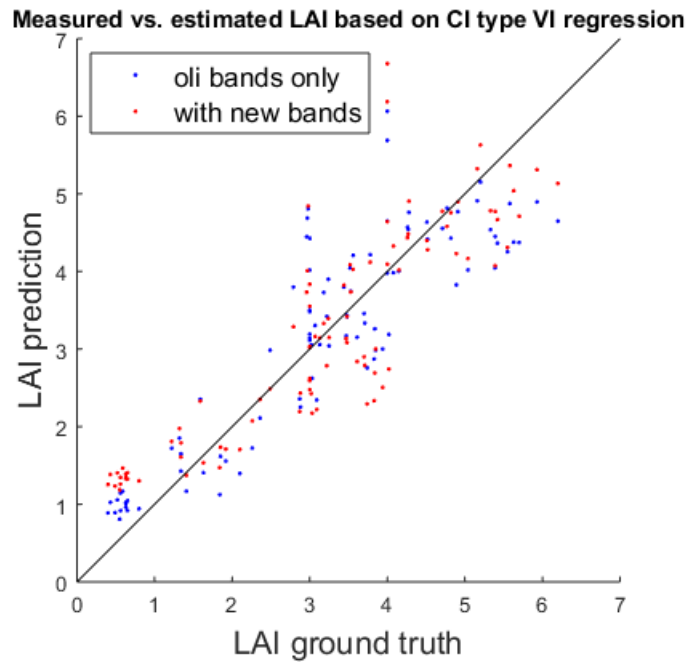
Compared to regression-based approaches which require training data to calibrate the regression model, LUT inversion is more practical for operational level LAI estimation. In this study, first, all possible OLI band combinations ( $C_6^1 + C_6^2 + C_6^3 + C_6^4 + C_6^5 + C_6^6 = 63$  cases) were tested for LUT inversion. Then the band settings involving potential new band(s) were tested. Up to 3 out of 14 new potential bands were considered. The total number of cases of the addition of 0, 1, 2, or 3 new potential bands are listed in Table 7.2.

Figure 7.9 is a summary of the LUT inversion results with no new band or the addition of one new potential band. The leftmost bar corresponds to the statistics of top 10% performing OLI band only combinations, which serves as the baseline. In all cases, each blue box corresponds to the range of the top 10% band combinations when each new potential band was added. For example, the 662 nm box corresponds to the top 10% of the combinations that 662 nm band together with all possible 64 OLI band





(a)  $R^2$  between ground truth LAI and  $CI_{a-b}$  for different band combinations



(b) Scatter plot of the predicted LAI versus ground truth LAI. Blue is from the  $CI_{655-561}$ , red is from  $CI_{561-677}$

Figure 7.8: Result of VI ( $CI_{a-b}$ ) regression approach.

Bands	OLI Band Cases	New Potential Band Cases	Total Cases
OLI only	63	N/A	63
One new band	64	14( $C_{14}^1$ )	896
Two new bands	64	91( $C_{14}^2$ )	5824
Three new bands	64	364( $C_{14}^3$ )	23296

Table 7.2: Number of possible band combinations for adding 0/1/2/3 new potential bands.

combinations. In each box, the red line is the average performance and the lower and upper boundaries of the box are the first and third quartile performance. The red crosses correspond to outliers.

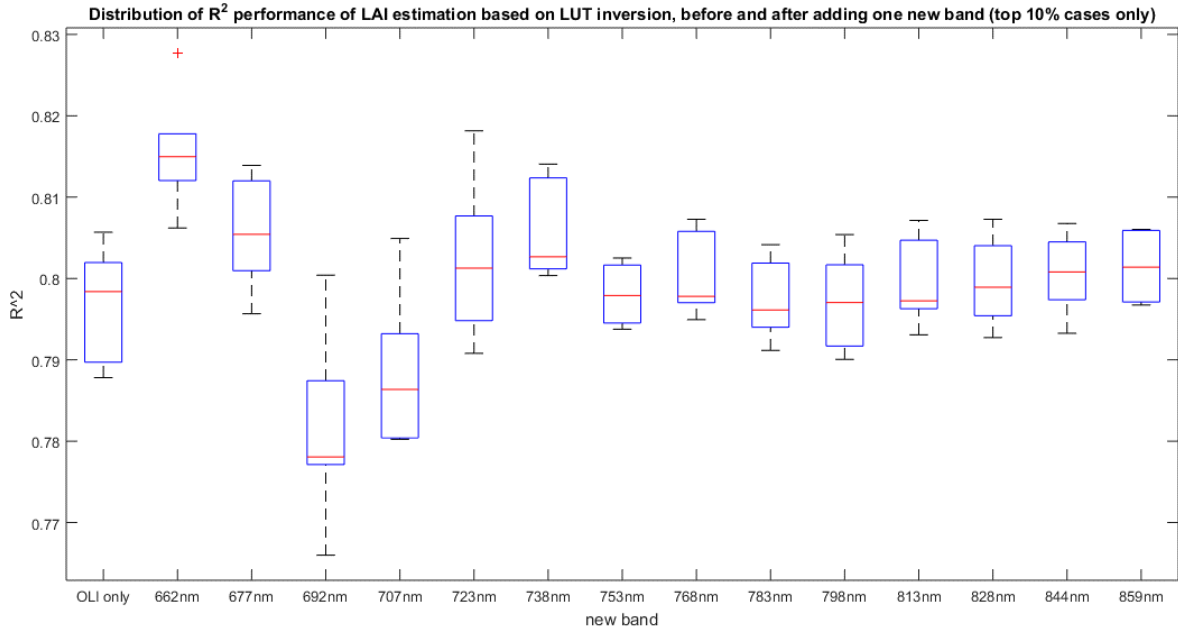


Figure 7.9: Statistics of top 10% performance of adding 0/1 new bands in LUT inversion approach.

For the combination using OLI bands only, the optimal band combination is green, red, NIR, SWIR1, SWIR2 bands with  $R^2$  of 0.806. If we consider the best performing cases

for each new potential band added, two spectral range peaks can be observed: 662 – 677 nm and 723 – 738 nm. The overall best performance was the combination of 662 nm, OLI band 3 (green), NIR, SWIR1, SWIR2 bands with  $R^2$  of 0.828.

The statistics of  $R^2$  of the top 10% cases of adding no (0), 1, 2, or 3 new potential bands were examined and are shown in Figure 7.10. Due to the enormous number of band combinations, the details of adding two or three new bands are not listed. The addition of two or three new bands only slightly improved the LAI retrieval accuracy (less than 0.01 in  $R^2$ ), compared to adding one new band.

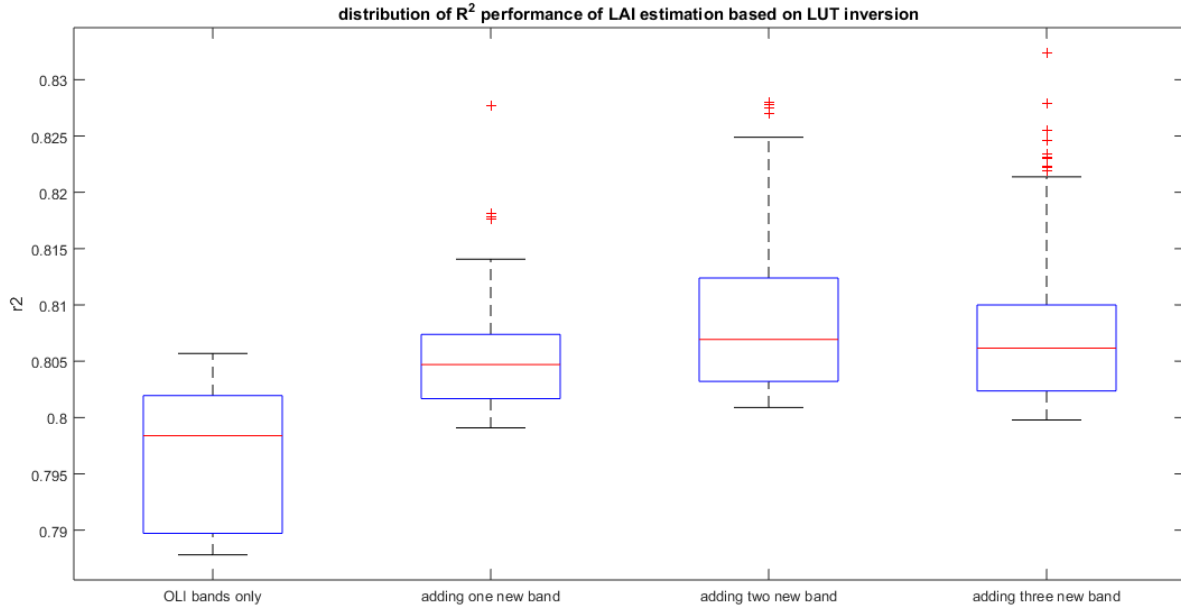


Figure 7.10: Statistics of top 10% performing cases of adding 0/1/2/3 new bands in LUT inversion approach.

### 7.3.3 Support Vector Regression Approach Result

Figure 7.11 is the summary of adding zero or one new potential band using the SVR approach. The way to interpret the plot is similar to the LUT inversion result shown

in Figure 7.9. The  $R^2$  of the cases in Figure 7.11 were in a small range from 0.90 to 0.925. The overall performance was higher than the VI and LUT inversion approaches, which is reasonable because of the power of non-linear regression. However, the limited variation range (less than 0.03) indicated the SVR result may have suffered from over fitting. If we consider the best case for each new band added, almost no improvement was achieved after adding any of these potential new bands. If we consider the average performance of each column, the new bands within the spectral range between 677 nm and 707 nm were seen to improve the LAI retrieval accuracy, although the improvement was minimal. The retrieval results of the addition of two or three new bands are not listed here because no significant improvement was observed.

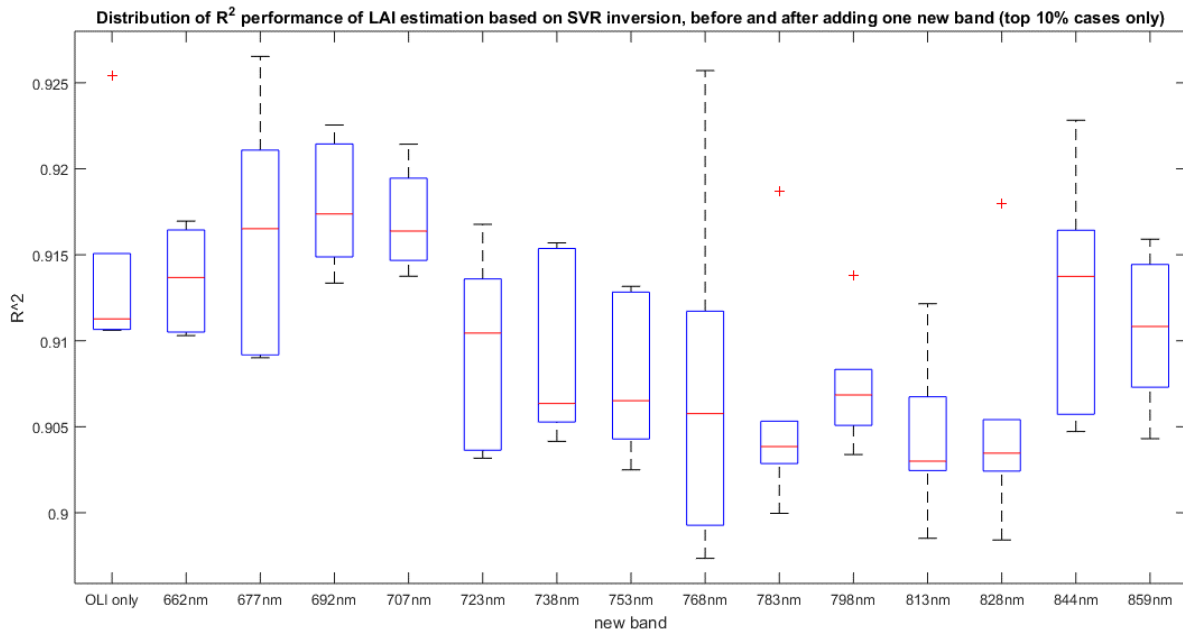


Figure 7.11: Statistics of top 10% performance of adding 0/1 new bands in SVR approach.

### 7.3.4 Discussion

Table 7.3 summarizes the LAI estimation performance before and after the addition of potential new spectral bands using all three retrieval approaches. For each approach, the optimal new band spectral range is listed as well.

	$R^2$	VI( $NDVI_{a-b}$ )	$R^2$	LUT(one new band only)	$R^2$	SVR
		Optimal two bands center range		Optimal new band center range		Optimal new band center range
OLI bands only	0.787	OLI band 3 and OLI band 4	0.806	N/A	0.925	N/A
With new bands	0.810	$670 \pm 8nm$ and $700 \pm 8nm$	0.828	$670 \pm 8nm$ or $730 \pm 8nm$	0.933	$692 \pm 15nm$

Table 7.3: LAI retrieval performance and optimal new band center position range of three retrieval approaches.

All three approaches showed small improvements by adding new potential bands. This is not too surprising and has been seen in previous studies with simulated and real datasets. For the estimation of agroecosystem green LAI, using the same SPARC '03 field campaign data, [32] studied different machine learning algorithms for LAI retrieval based on simulated Sentinel-2 imagery. They found limited improvements with Gaussian process regression (GPR) approach when Sentinel-2 red edge bands were included ( $R^2 = 0.91$  vs.  $R^2 = 0.90$ ). Also, the GPR significance analysis showed that the red edge bands were less important than Sentinel-2 blue, green, and NIR bands. Researchers in [90] used SPARC '03 and '04 CHRIS data to search for optimal two-band combinations for LAI estimation based on VI regression approach. The  $R^2$  of their optimal band settings (674 nm and 712 nm) was 0.824, which was only slight increased from the combination of OLI red and NIR ( $R^2 \approx 0.78$ ). Researchers in [34] studied the LAI estimation in both LUT inversion and artificial neural network approaches with Sentinel-2 band settings. They studied the significance of each Sentinel-2 spectral band by counting the frequency each band appeared in the top 5% band combinations. In their result, the three Sentinel-2 red edge bands did not show dominance over the other spectral bands. For single crop species biophysical quantity retrieval, [38] used real Sentinel-2 data to study the

VI approach based potato crop LAI and canopy chlorophyll content (CCC) estimation. They concluded that Sentinel-2 10 m bands (blue, green, red, NIR) were better than 20 m bands (red edge bands) for LAI and CCC retrieval. In [39] Korhonen et al. compared the boreal forest canopy LAI estimation performances with real Sentinel-2 and Landsat-8 data. Their result with Sentinel-2 data was slightly better than the result with Landsat-8 OLI data ( $R^2 = 0.734$  vs.  $R^2 = 0.725$ ), even though Sentinel-2 has three red edge bands and Landsat-8 OLI does not have one. Researchers in [94] estimated LAI of a cotton canopy through VI regression approach. After going through all possible band combinations, they observed 2.2% improvement in  $R^2$  using their optimal band combination (700 and 800 nm) over the combination of Landsat TM red and NIR bands.

Considering Table 7.3, both VI and LUT approaches had two optimal new band spectral ranges. The common range was 662 – 677 nm. This is not surprising and two possible reasons can explain this. First, the correlation coefficients between the ground truth LAI and spectral reflectance reached the maximum absolute value near 662 – 677 nm. As suggested in [99], it is beneficial to include those spectral bands centered at wavelengths with high correlation coefficients. Second, the bandpass of the OLI red band is from 636 nm to 673 nm, which is wide compared to the studied HyMap bandwidth (15 nm in VIS and NIR). The bandpass of HyMap 662 nm is approximately from 655 nm to 670 nm. This is entirely within the OLI red bandpass. In this wavelength range that is very sensitive to biophysical quantity changes, the narrower HyMap 662 nm band can better capture the spectral reflectance subtle difference caused by LAI difference than the existing OLI red band. This was verified in our results by the observation that the narrow 662 nm band was selected more often than the existing OLI red band in the LUT inversion approach top performing band combinations.

This results were slightly different from the previous studies that focused on single crop species LAI retrieval. In this work, the small improvement observed from the addition of new bands may be due to the fact that we considered a complex agroecosystem with nine crop species at different growth stages. This may overwhelm the spectral features located in the red edge region for a single crop species.

## 7.4 Canopy Chlorophyll Content Retrieval Results

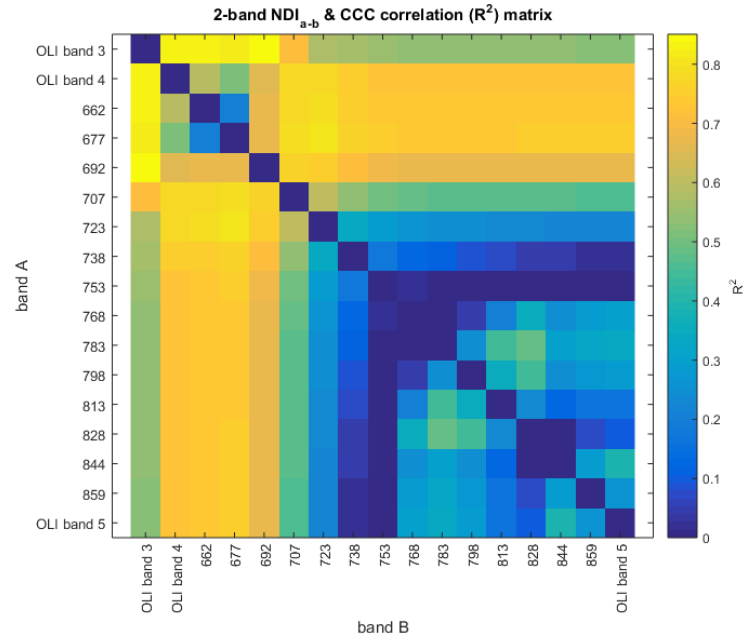
Similar as LAI retrieval, the above mentioned three retrieval approaches were tested for CCC retrieval as well. The only difference was that SWIR 1 and SWIR 2 bands were excluded, since SWIR bands are not related to chlorophyll content. Only visible to NIR bands were considered for CCC retrieval. The results of the three approaches are reported in this section.

### 7.4.1 Empirical Vegetation Index Regression Approach Result

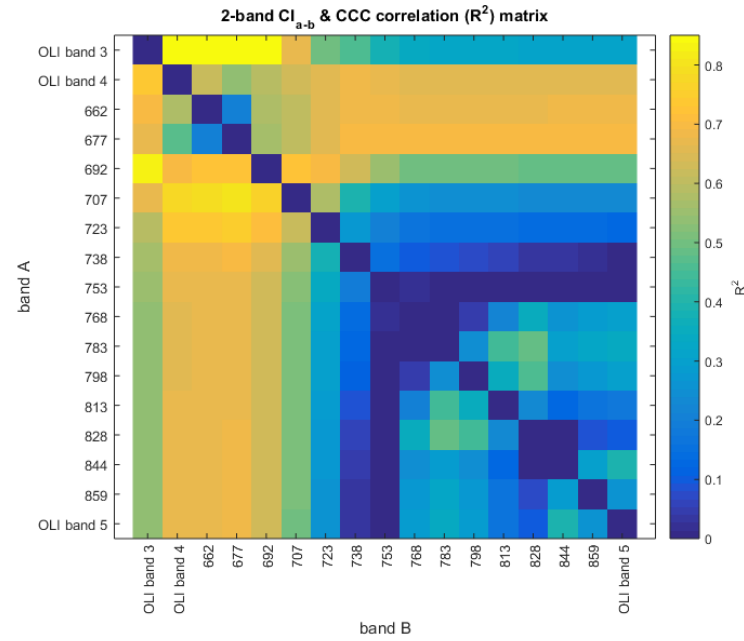
The  $R^2$  of CCC retrieval performance for all possible two-band combination  $NDVI_{a-b}$  are plotted in Figure 7.12 (a). When only original OLI bands were considered, the optimal performance band combination was OLI green band and OLI red band, with  $R^2$  of 0.853. When potential new bands were included, the combination of OLI green band and 692nm band was slightly better with  $R^2$  of 0.875. The  $R^2$  of CCC retrieval performances for all possible two-band combination  $CI_{a-b}$  are plotted in Figure 7.12 (b). When only original OLI bands were considered, the optimal performance band combination was OLI green band and OLI red band, with  $R^2$  of 0.851. When potential new bands were included, the combination of OLI green band and 692nm band was slightly better with  $R^2$  of 0.863. Both the  $R^2$  values and the improvements of CI retrieval results were similar as LAI retrieval results. This is not surprising since CCC is related to LAI.

### 7.4.2 LUT Inversion Approach Result

Figure 7.13 is the summary of the CCC retrieval based on LUT inversion approach with no new bands or the addition of one new potential band. The first observation is that comparing to LAI retrieval, the overall  $R^2$  performance of CCC retrieval was much lower ( $R^2$  around 0.8 vs.  $R^2$  around 0.5). Then, regarding the optimal new potential band, comparing with the left-most bar, which corresponds to the statistics of top 20% band combinations when only OLI bands were considered, a peak was observed when



(a)  $R^2$  between ground truth CCC and  $NDVI_{a-b}$  for different band combinations



(b)  $R^2$  between ground truth CCC and  $CI_{a-b}$  for different band combinations

Figure 7.12: Result of VI ( $CI_{a-b}$ ) regression approach for CCC.



the new potential bands centered at 662nm or 677nm were added. It was interesting to see that the addition of one potential new band centered between 707nm to 753nm decreased the CCC retrieval performance, from the view of mean statistics. Besides, the potential new bands above 753nm had limited influence on the mean performance, but contributed to decrease the standard deviation.

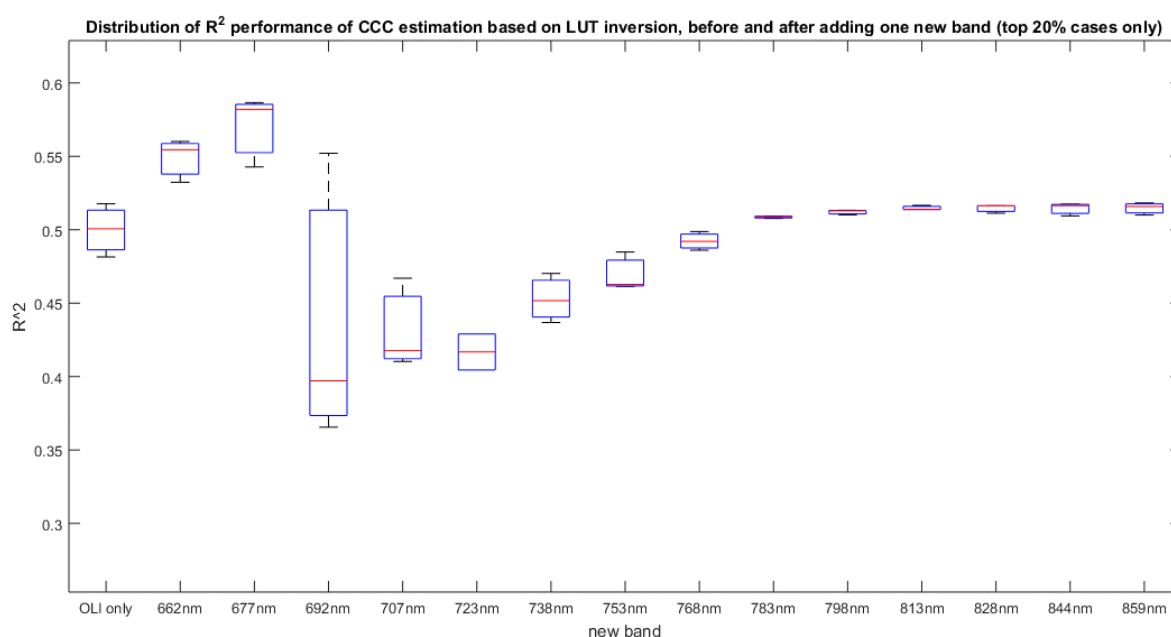


Figure 7.13: Statistics of top 10% performing cases of adding 0/1 new bands in SVR approach.

### 7.4.3 Support Vector Regression Approach Result

Figure 7.14 is the summary of adding zero or one new potential band for CCC retrieval using SVR approach. Similar as the SVR approach for LAI result, the  $R^2$  of all cases were high, ranging from 0.85 to 0.89. And the variation among all cases were low. The addition of new potential band centered from 677nm to 738nm slightly improved the performance, comparing to considering OLI bands only.

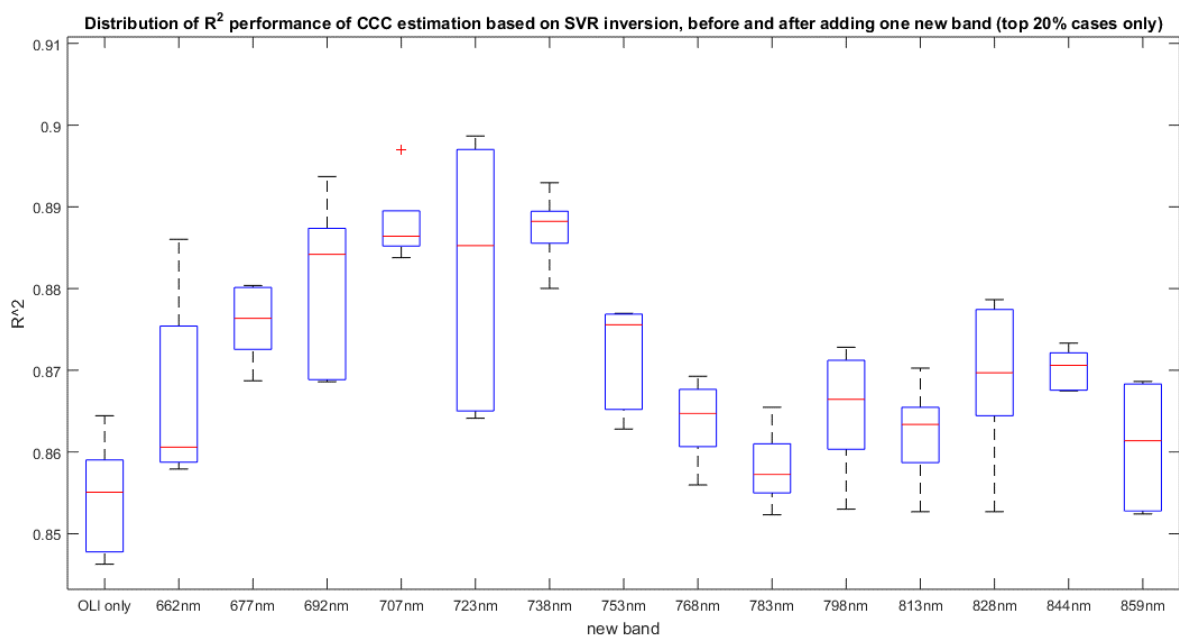


Figure 7.14: Statistics of top 10% performance of adding 0/1 new bands in SVR approach.

#### 7.4.4 Discussion

Table 7.4 summarizes the CCC retrieval performance before and after the addition of potential new spectral bands using the three retrieval approaches. For each approach, the optimal new band spectral range is listed as well. The result of adding two or three new bands were also studied. Since no significant improvement was observed comparing to adding one new band, their results are not listed here.

	$R^2$	VI( $NDVI_{a-b}$ )	LUT(one new band only)		SVR	
		Optimal two bands center range	$R^2$	Optimal new band center range	$R^2$	Optimal new band center range
OLI bands only	0.853	OLI band 3 and OLI band 4	0.500	N/A	0.854	N/A
With new bands	0.875	OLI band 3 and $692 \pm 8nm$	0.570	$677 \pm 8nm$	0.887	$677 - 738nm$

Table 7.4: CCC retrieval performance and optimal new band center position range of three retrieval approaches.

The  $R^2$  performance of VI regression and SVR approaches for CCC retrieval were similar with LAI retrieval. This was reasonable since both VI and SVR approaches are supervised regression and can explore the intrinsic relationship between different spectral band reflectance and interested biophysical quantity. What's more,  $CCC = LAI \times LCC$ , this ensures the performances of LAI retrieval and CCC retrieval are similar, given the same dataset.

However, why in LUT inversion approach the result of LAI retrieval and CCC retrieval were very different in the sense of  $R^2$ ? This can be explained from different perspectives:

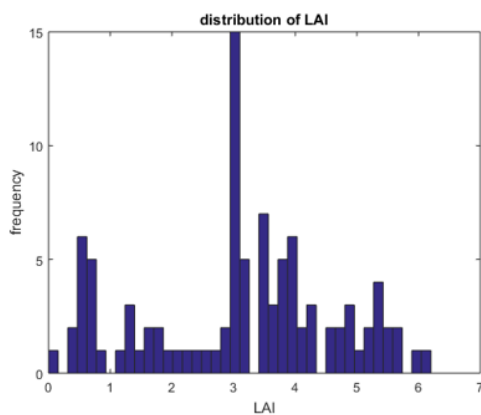
First, from the view of PROSAIL RTM based LUT generation, LAI is a single variable, while CCC is a compound variable. In real scenario, the co-distribution of LAI and LCC is suppose to follow specific patterns. Or at least, some co-distributions of LAI and LCC never appear in the real world. For example, dense green wheat canopies are never associated with low LCC. Actually, some researches [100] have already considered the co-distribution of input variables when they generated the LUT. To reinforce the representativeness of the LUT entries, they assumed the LCC variation range changes linearly with the LAI. This trick improved the performance and robustness of the LUT inversion results. However, in this study, when setting the PROSAIL model input variable distributions for LUT generation, the LAI and LCC distributions were individually set and no co-distribution was reinforced. Besides, though given the co-distribution of input variables for LUT generation, the PROSAIL model itself can not perfectly simulate the complex relationship between spectral reflectance and variables such as LCC and LAI. These factors limited the representativeness of the LUT for CCC retrieval, when comparing with the situation that the same LUT was used for LAI retrieval.

Second, from the view of SPARC '03 dataset. Figure 7.15 plots the distributions of LAI, LCC and CCC of all SPARC '03 dataset samples. As shown in Figure 7.15 (a), LAI approximately followed normal distribution. However, as shown in Figure 7.15 (b), LCC followed an irregularly distribution. Indeed, most LCC values concentrated on several distinct specific values. This was limited by the field campaign crops that

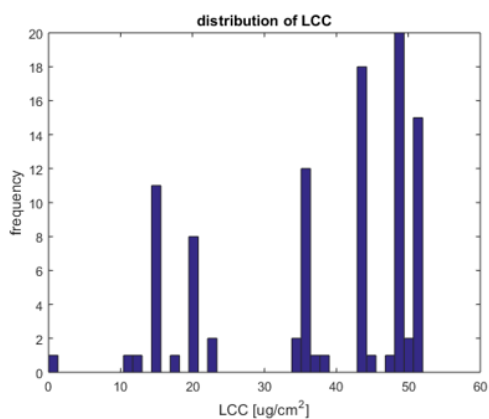
the same crop species samples had nearly the same LCC measurements, while their LAI measurements were more diverse. This resulted in the irregular distribution of CCC, as shown in Figure 7.15 (c). This trend can also be seen in the co-distribution scatter plots as shown in Figure 7.16. Both the co-distributions of LAI-LCC and LAI-CCC fell on several straight lines. This means that these variable values were highly depended on crop species. Though the LCC of SPARC '03 dataset was irregularly distributed, in this study gaussian distribution of LAI and LCC were assumed to generate the LUT. It is not reasonable to use specific shape distribution for specific dataset just for improving the retrieval performance.

In this study, the addition of red-edge band(s) on top of OLI spectral bands only slightly improved the chlorophyll content retrieval performance. This may be against people's intuition. However, recent studies with real data have proven that red-edge bands do not always improve the CCC retrieval performance. For example, in [38] Clevers et al. studied the VI regression approach for CCC retrieval using real Sentinel-2 data. They found the CCC retrieval performances with VI composed of Sentinel-2 10m bands (blue, green, red and NIR bands) were equal or better than the performances with VI when Sentinel-2 20m bands (red-edge bands) were involved.

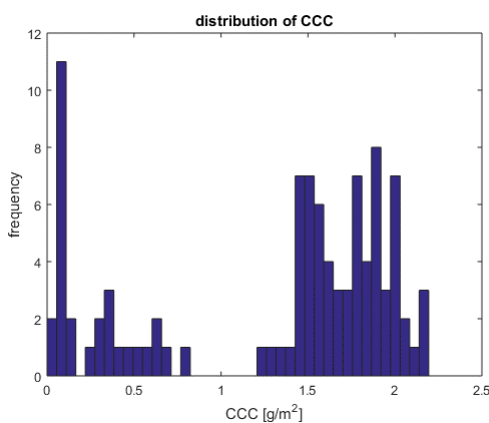
Besides, though some studies found the significance of red-edge bands for chlorophyll retrieval, most of them focused on single crop species only. It was interesting that they also found "equilibrium point" for each crop species. For example, [96] found the spectral reflectance at 730nm showed no clear decrease or increase with varying LAI or LCC. And [38] found the same effect for potato near 705nm. However in this thesis, the SPARC '03 dataset was composed of multiple (9) crop species. Even though the linear relationship between red-edge band spectral reflectance and chlorophyll content may exist for single crop species, this effect was overwhelmed in SPARC '03 dataset and performed like an "equilibrium point" within the red-edge region. That is why it should be emphasized that the results and conclusions of this study are for agroecosystem only.



(a) Leaf Area Index (LAI) distribution

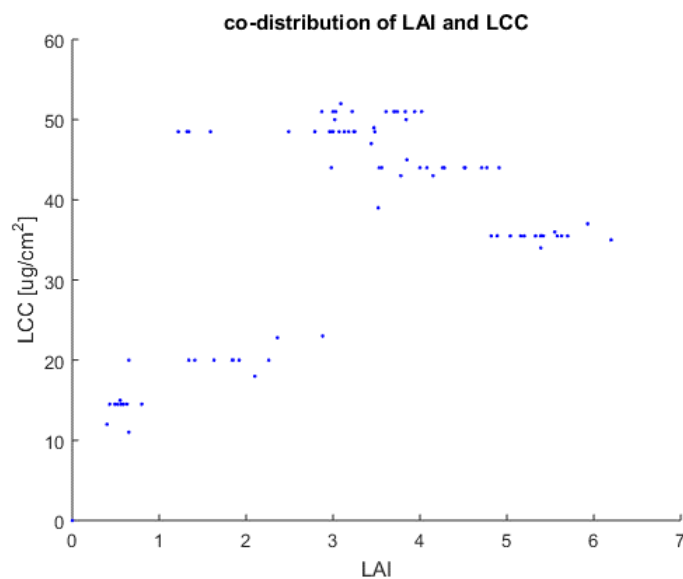


(b) Leaf Chlorophyll Content (LCC) distribution

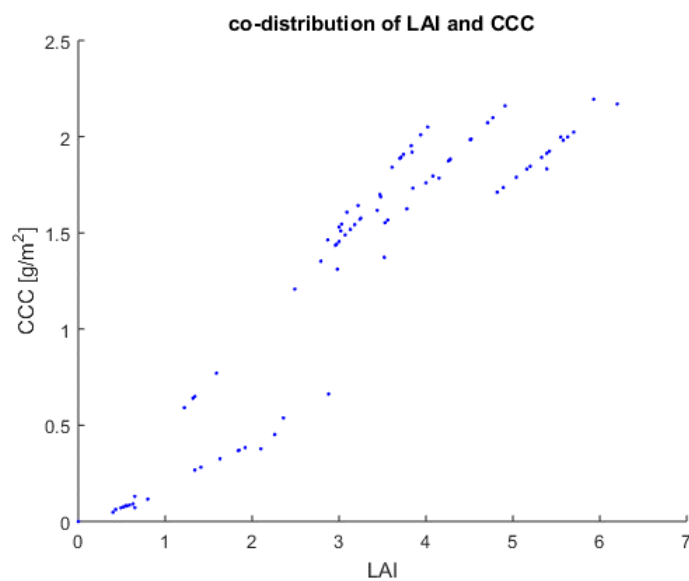


(c) Canopy Chlorophyll Content (CCC) distribution

Figure 7.15: SPARC '03 dataset ground truth variables distribution.



(a) Co-distribution of LAI and LCC



(b) Co-distribution of LAI and CCC

Figure 7.16: SPARC '03 dataset ground truth variables co-distribution.

## 7.5 Summary

In this chapter, the potential of adding new spectral band(s) within OLI red and NIR bands in future Landsat instruments for agroecosystem green leaf area index (LAI) and canopy chlorophyll content (CCC) retrieval was studied. Three categories of retrieval approaches were tested: empirical vegetation index regression ( $NDVI_{a-b}$  and  $CI_{a-b}$ ), physical based LUT inversion, and machine learning (SVR). The results from all three approaches suggested that slight retrieval accuracy increase can be achieved after the addition of at most three new spectral bands located between the OLI red and NIR bands. For LAI retrieval, in both the VI and LUT approaches, a new band centered in the range from 662 nm to 677 nm was observed to provide a small improvement in performance. However, this result may be due to the fact that the new bands studied were narrower than the current OLI red band and closer to the wavelength range more sensitive to LAI change. For CCC retrieval, in LUT inversion approach, a new spectral band centered at 677nm or 662nm improved the performance from  $R^2 = 0.50$  to  $R^2 = 0.57$ . It should be noticed that the SPARC '03 dataset used in this work covers multiple crop species. This species mixture may overwhelm the correlation between specific wavelength spectral reflectance and biophysical quantities.

This work has been published in [101].

# Chapter 8

## Summary and Outlook

### 8.1 Conclusions

In this thesis, a framework was built by integrating models to study the sensitivity of radiance signal and science product to instrument design changes. Specifically, this thesis studied the impacts of two potential design concepts in future Landsat instruments on vegetation monitoring tasks: 1) the wider field-of-view (FOV) instrument design to achieve new angular observations and higher temporal sampling; 2) the addition of the red-edge spectral band design for canopy biophysical quantity retrieval. Three different studies were explored to estimate the potential impacts:

1. The impacts of the RSR shift effect in wider FOV design on measured spectral radiance signal were studied for both Landsat 8 OLI and the potential future Landsat instruments, using DIRSIG image simulation tool. Results indicate that the RSR shift effect has band-dependent significance: in visible and NIR bands the RSR shift interacting with atmospheric path radiance is the main source of at detector radiance signal difference, and in SWIR bands the RSR shift interacting with surface BRF and ground reaching irradiance is more significant. And the impact of the RSR shift will exceed sensor noise in all bands except the SWIR 1 band. It is also noticed that the SWIR2 band



may be sensitive to atmosphere conditions when the angle of incidence (AOI) is as large as 15 degrees. However, due to the limited knowledge of the future Landsat instrument optics design, this study was based on the assumption that the AOI at the detector filter is equal to the AOI at the instrument input aperture. This corresponded to the worst case and can not be applied to all optic designs.

2. The impacts of potential wider FOV instrument design on vegetation monitoring products accuracy were studied. Both crop classification and canopy biophysical quantity retrieval applications were studied using synthetic data generated by DIRSIG and the canopy radiative transfer model PROSAIL. It should be noted that the RSR shift effect was also considered and modeled in this study. Results show that for single scene analyses the higher angular observations have limited influence on both applications. However, for situations where two observations can be obtained from multiple platforms imaging at different view zenith angles, up to 4% improvement for crop classification and 2.9% improvement for leaf chlorophyll content retrieval were found.

3. The impacts of adding red-edge band(s) in future Landsat satellites on agroecosystem canopy leaf area index (LAI) and canopy chlorophyll content (CCC) were studied using SPARC '03 campaign dataset. Results of three tested approaches show that a potential new spectral band located between the Landsat-8 Operational Land Imager (OLI) red and NIR bands slightly improved the retrieval accuracy (LAI:  $R^2$  of 0.787 vs. 0.810 for empirical vegetation index regression approach, 0.806 vs. 0.828 for look-up-table inversion approach, and 0.925 vs. 0.933 for machine learning approach; CCC:  $R^2$  of 0.853 vs. 0.875 for empirical vegetation index regression approach, 0.500 vs. 0.570 for look-up-table inversion approach, and 0.854 vs. 0.887 for machine learning approach). It should be noticed that the SPARC '03 dataset used in this work covers multiple crop species, and the results and conclusions are for agroecosystem scenarios only.

## 8.2 Contributions

In general, this thesis set up a framework by integrating models to study the end-to-end sensitivity between radiance signal or scientific product accuracy and potential satellite instrument design concept changes for the remote sensing community. To answer the questions raised during the instrument concept design phase, the framework integrated the remote sensing satellite instrument model, physics-driven synthetic image generation model, ground surface reflectance characteristics model and different scientific product algorithms.

In detail, this thesis answered the potential impacts of wider FOV and the addition of red-edge spectral band(s) designs on vegetation monitoring tasks for future Landsat instrument. The specific contributions of the studied topics are listed below:

1. This research is unique by quantitatively studying the impact of RSR shift effect on vegetation monitoring radiance signal in simulation approach. The published literature have no studies on the RSR shift effect on pushbroom scanner. In this thesis, the significance of RSR shift on radiance signal variation for each Landsat instrument spectral band of Landsat 8 OLI and potential future Landsat instrument is quantified through factorial analysis.

2. To our knowledge, this is the first work to study the impacts of wider FOV design on vegetation monitoring scientific products for future Landsat instrument. Besides, this work demonstrates the capability of the image simulation tool DIRSIG to be used in connection with angular variant vegetation canopy radiative transfer model PROSAIL. A data simulation pipeline has been built to generate simulated data to support the remote sensing instrument system engineering design and end-to-end analysis.

3. The potential impacts of adding red-edge spectral band(s) on future Landsat instrument on agroecosystem canopy quantity retrieval were estimated. Three different major retrieval approaches were tested and the potential improvements were quantified. To our knowledge, this is the first work to predict the significance of red-edge spectral bands used together with previous Landsat spectral bands for agroecosystem green leaf

area index and canopy chlorophyll content retrieval tasks.

### 8.3 Outlook and future work

In general, since the studied sensitivities are biophysical quantity and algorithm dependent, similar work can be done to study the impacts of potential new design concepts on other interested quantities and algorithms by extending the framework this thesis set up. In detail, for each of the three studies, several potential future directions are introduced in this section:

1. For the RSR shift effect study, in future work additional ground target types can be extended in the simulation, such as soil, sand, snow, or coastal water. Since the impacts of the wavelength shift on measured spectral radiance difference are dependent on the ground target spectrum, these additional ground cover types will help refine the instrument design requirements.

Another future direction is to explore additional methods for compensating the at detector spectral radiance difference due to deterministic RSR shift. So that the angular variation in radiance level could be minimized for further studies. For example, a Spectral Band Adjustment Factor (SBAF) approach may be used to compensate the spectral radiance signal difference due to RSR variation across the focal plane [102].

2. For the wider FOV study, this work only adopted the 2-D canopy PROSAIL radiative transfer model. Since PROSAIL is parameterized with limited number of input variables, it is a potential direction to explore the usage of DIRSIG simulation tool in connection with 3-D canopy geometry model. For example, a 3-D canopy geometry model together with the leaf model PROSPECT. This will break the limitation of PROSAIL model assumptions and increase the simulation flexibility.

Besides, the DIRSIG tool and PROSAIL model was integrated for end-to-end analysis in the wider FOV study. The flexibility of the PROSAIL model and its connection with DIRSIG tool were verified. This is beneficial for future DIRSIG based synthetic vegetation scene image generation. And this integrated framework can be extended in the future

for vegetation related studies.

3. For the red-edge band study, due to the limited availability of field campaign datasets, this study only tested the retrieval performances on agroecosystem dataset. In the future, one direction is to apply the approaches tested in this work on multiple single-species datasets. Another direction is to apply the approaches on multiple datasets over the same field at different times. Both directions are aiming at testing the robustness of the calibrated regression model.

Besides, the spectral bandwidths of HyMap visible and NIR spectral bands are about 15nm, which limited the spectral resolution in the red-edge band study. In the future, either high spectral resolution real field campaign datasets or synthetic datasets could be used to improve the spectral accuracy in similar topic studies.

# Bibliography

- [1] J. R. Schott, *Remote sensing*, Oxford University Press, 2007.
- [2] R. B. Myneni, S. Hoffman, Y. Knyazikhin, J. Privette, J. Glassy, Y. Tian, Y. Wang, X. Song, Y. Zhang, G. Smith, *et al.*, "Global products of vegetation leaf area and fraction absorbed par from year one of modis data," *Remote sensing of environment* **83**(1), pp. 214–231, 2002.
- [3] C. Bacour, F. Baret, D. Béal, M. Weiss, and K. Pavageau, "Neural network estimation of lai, fapar, fcover and lai $\times$  c ab, from top of canopy meris reflectance data: Principles and validation," *Remote sensing of environment* **105**(4), pp. 313–325, 2006.
- [4] "landsat missions." <https://landsat.usgs.gov/>. Accessed: June 2017.
- [5] D. Horler, M. DOCKRAY, and J. Barber, "The red edge of plant leaf reflectance," *International Journal of Remote Sensing* **4**(2), pp. 273–288, 1983.
- [6] P. Teillet, J. Barker, B. Markham, R. Irish, G. Fedosejevs, and J. Storey, "Radiometric cross-calibration of the landsat-7 etm+ and landsat-5 tm sensors based on tandem data sets," *Remote sensing of Environment* **78**(1), pp. 39–54, 2001.
- [7] A. P. Trishchenko, J. Cihlar, and Z. Li, "Effects of spectral response function on surface reflectance and ndvi measured with moderate resolution satellite sensors," *Remote Sensing of Environment* **81**(1), pp. 1–18, 2002.

- 
- [8] A. Gonsamo and J. M. Chen, "Spectral response function comparability among 21 satellite sensors for vegetation monitoring," *IEEE Transactions on Geoscience and Remote Sensing* **51**(3), pp. 1319–1335, 2013.
- [9] W. J. Van Leeuwen, B. J. Orr, S. E. Marsh, and S. M. Herrmann, "Multi-sensor ndvi data continuity: Uncertainties and implications for vegetation monitoring applications," *Remote sensing of environment* **100**(1), pp. 67–81, 2006.
- [10] P. D'Odorico, A. Gonsamo, A. Damm, and M. E. Schaepman, "Experimental evaluation of sentinel-2 spectral response functions for ndvi time-series continuity," *IEEE Transactions on Geoscience and Remote Sensing* **51**(3), pp. 1336–1348, 2013.
- [11] J. A. Barsi, B. L. Markham, and J. A. Pedelty, "The operational land imager: spectral response and spectral uniformity," in *Proc. SPIE*, **8153**, pp. 81530G–81530G, 2011.
- [12] J. A. Barsi, K. Lee, G. Kvaran, B. L. Markham, and J. A. Pedelty, "The spectral response of the landsat-8 operational land imager," *Remote Sensing* **6**(10), pp. 10232–10251, 2014.
- [13] B. L. Markham and D. L. Helder, "Forty-year calibrated record of earth-reflected radiance from landsat: A review," *Remote Sensing of Environment* **122**, pp. 30–40, 2012.
- [14] D. Helder, K. J. Thome, N. Mishra, G. Chander, X. Xiong, A. Angal, and T. Choi, "Absolute radiometric calibration of landsat using a pseudo invariant calibration site," *IEEE Transactions on Geoscience and Remote Sensing* **51**(3), pp. 1360–1369, 2013.
- [15] P. Teillet, K. Staenz, and D. William, "Effects of spectral, spatial, and radiometric characteristics on remote sensing vegetation indices of forested regions," *Remote Sensing of Environment* **61**(1), pp. 139–149, 1997.
- [16] J. Franke, V. Heinzl, and G. Menz, "Assessment of ndvi-differences caused by sensor specific relative spectral response functions," in *Geoscience and Remote Sens-*

- 
- ing Symposium, 2006. IGARSS 2006. IEEE International Conference on*, pp. 1138–1141, IEEE, 2006.
- [17] P. Teillet, G. Fedosejevs, K. Thome, and J. L. Barker, “Impacts of spectral band difference effects on radiometric cross-calibration between satellite sensors in the solar-reflective spectral domain,” *Remote Sensing of Environment* **110**(3), pp. 393–409, 2007.
  - [18] N. Mishra, M. O. Haque, L. Leigh, D. Aaron, D. Helder, and B. Markham, “Radiometric cross calibration of landsat 8 operational land imager (oli) and landsat 7 enhanced thematic mapper plus (etm+),” *Remote Sensing* **6**(12), pp. 12619–12638, 2014.
  - [19] M. Barnsley, P. Lewis, S. O’Dwyer, M. Disney, P. Hobson, M. Cutter, and D. Lobb, “On the potential of chris/proba for estimating vegetation canopy properties from space,” *Remote Sensing Reviews* **19**(1-4), pp. 171–189, 2000.
  - [20] M. Leroy, J. Deuze, F. Bréon, O. Hautecoeur, M. Herman, J. Buriez, D. Tanré, S. Bouffies, P. Chazette, and J. Roujean, “Retrieval of atmospheric properties and surface bidirectional reflectances over land from polder/adeos,” *Journal of Geophysical Research: Atmospheres* **102**(D14), pp. 17023–17037, 1997.
  - [21] W. Lucht, “Expected retrieval accuracies of bidirectional reflectance and albedo from eos-modis and misr angular sampling,” *Journal of Geophysical Research: Atmospheres* **103**(D8), pp. 8763–8778, 1998.
  - [22] J. Verrelst, M. E. Schaepman, B. Koetz, and M. Kneubühler, “Angular sensitivity analysis of vegetation indices derived from chris/proba data,” *Remote Sensing of Environment* **112**(5), pp. 2341–2353, 2008.
  - [23] F. M. Breunig, L. S. Galvão, A. R. Formaggio, and J. C. N. Epiphanyo, “Directional effects on ndvi and lai retrievals from modis: A case study in brazil with soybean,”

---

*International Journal of Applied Earth Observation and Geoinformation* **13**(1), pp. 34–42, 2011.

- [24] L. S. Galvão, D. A. Roberts, A. R. Formaggio, I. Numata, and F. M. Breunig, “View angle effects on the discrimination of soybean varieties and on the relationships between vegetation indices and yield using off-nadir hyperion data,” *Remote Sensing of Environment* **113**(4), pp. 846–856, 2009.
- [25] A. S. Xavier and L. S. Galvão, “View angle effects on the discrimination of selected amazonian land cover types from a principal-component analysis of misr spectra,” *International Journal of Remote Sensing* **26**(17), pp. 3797–3811, 2005.
- [26] M. Weiss, F. Baret, R. Myneni, A. Pragnère, and Y. Knyazikhin, “Investigation of a model inversion technique to estimate canopy biophysical variables from spectral and directional reflectance data,” *Agronomie* **20**(1), pp. 3–22, 2000.
- [27] M. M. Verstraete, B. Pinty, and R. E. Dickinson, “A physical model of the bidirectional reflectance of vegetation canopies: 1. theory,” *Journal of Geophysical Research: Atmospheres* **95**(D8), pp. 11755–11765, 1990.
- [28] X. Li, A. H. Strahler, C. E. Woodcock, *et al.*, “A hybrid geometric optical-radiative transfer approach for modeling albedo and directional reflectance of discontinuous canopies,” *IEEE Transactions on geoscience and remote sensing* **33**(2), pp. 466–480, 1995.
- [29] S. Liang and A. H. Strahler, “Retrieval of surface brdf from multiangle remotely sensed data,” *Remote Sensing of Environment* **50**(1), pp. 18–30, 1994.
- [30] J. G. Clevers, S. M. de Jong, G. F. Epema, F. van der Meer, W. H. Bakker, A. K. Skidmore, and E. A. Addink, “Meris and the red-edge position,” *International Journal of Applied Earth Observation and Geoinformation* **3**(4), pp. 313–320, 2001.
- [31] P. Curran and J. Dash, “Evaluation of the meris terrestrial chlorophyll index,” in *Proceedings of the Airborne Imaging Spectroscopy Workshop-Bruges*, 2004.



- 
- [32] J. Verrelst, J. Muñoz, L. Alonso, J. Delegido, J. P. Rivera, G. Camps-Valls, and J. Moreno, "Machine learning regression algorithms for biophysical parameter retrieval: Opportunities for sentinel-2 and-3," *Remote Sensing of Environment* **118**, pp. 127–139, 2012.
- [33] J. Delegido, J. Verrelst, L. Alonso, and J. Moreno, "Evaluation of sentinel-2 red-edge bands for empirical estimation of green lai and chlorophyll content," *Sensors* **11**(7), pp. 7063–7081, 2011.
- [34] K. Richter, T. B. Hank, F. Vuolo, W. Mauser, and G. D'Urso, "Optimal exploitation of the sentinel-2 spectral capabilities for crop leaf area index mapping," *Remote Sensing* **4**(3), pp. 561–582, 2012.
- [35] I. Herrmann, A. Pimstein, A. Karnieli, Y. Cohen, V. Alchanatis, and D. Bonfil, "Lai assessment of wheat and potato crops by venus and sentinel-2 bands," *Remote Sensing of Environment* **115**(8), pp. 2141–2151, 2011.
- [36] R. Fernandes, M. Weiss, F. Camacho, B. Berthelot, F. Baret, and R. Duca, "Development and assessment of leaf area index algorithms for the sentinel-2 multispectral imager," in *Geoscience and Remote Sensing Symposium (IGARSS), 2014 IEEE International*, pp. 3922–3925, IEEE, 2014.
- [37] "comparison of landsat 7 and 8 bands with sentinel-2." <https://landsat.gsfc.nasa.gov/sentinel-2a-launches-our-compliments-our-complements/>. Accessed: January 2019.
- [38] J. G. Clevers, L. Kooistra, and M. M. van den Brande, "Using sentinel-2 data for retrieving lai and leaf and canopy chlorophyll content of a potato crop," *Remote Sensing* **9**(5), p. 405, 2017.
- [39] L. Korhonen, P. Packalen, M. Rautiainen, *et al.*, "Comparison of sentinel-2 and landsat 8 in the estimation of boreal forest canopy cover and leaf area index," *Remote sensing of environment* **195**, pp. 259–274, 2017.

- 
- [40] R. Rengarajan, *Evaluation of sensor, environment and operational factors impacting the use of multiple sensor constellations for long term resource monitoring*, Rochester Institute of Technology, 2016.
- [41] R. Rengarajan and J. Schott, "Evaluation of sensor and environmental factors impacting the use of multiple sensor data for time-series applications," *Remote Sensing* **10**(11), p. 1678, 2018.
- [42] A. Gerace, *Demonstrating Landsat's new potential to monitor coastal and inland waters*, Rochester Institute of Technology, 2010.
- [43] D. J. Diner, J. C. Beckert, T. H. Reilly, C. J. Bruegge, J. E. Conel, R. A. Kahn, J. V. Martonchik, T. P. Ackerman, R. Davies, S. A. Gerstl, *et al.*, "Multi-angle imaging spectroradiometer (misr) instrument description and experiment overview," *IEEE Transactions on Geoscience and Remote Sensing* **36**(4), pp. 1072–1087, 1998.
- [44] G. Schaepman-Strub, M. Schaepman, T. Painter, S. Dangel, and J. Martonchik, "Reflectance quantities in optical remote sensing definitions and case studies," *Remote sensing of environment* **103**(1), pp. 27–42, 2006.
- [45] W. Lucht, C. B. Schaaf, and A. H. Strahler, "An algorithm for the retrieval of albedo from space using semiempirical brdf models," *IEEE Transactions on Geoscience and Remote Sensing* **38**(2), pp. 977–998, 2000.
- [46] J.-L. Roujean, M. Leroy, and P.-Y. Deschamps, "A bidirectional reflectance model of the earth's surface for the correction of remote sensing data," *Journal of Geophysical Research: Atmospheres* **97**(D18), pp. 20455–20468, 1992.
- [47] X. Li and A. H. Strahler, "Geometric-optical bidirectional reflectance modeling of the discrete crown vegetation canopy: Effect of crown shape and mutual shadowing," *IEEE transactions on Geoscience and Remote Sensing* **30**(2), pp. 276–292, 1992.

- 
- [48] A. H. Strahler, J. Muller, W. Lucht, C. Schaaf, T. Tsang, F. Gao, X. Li, P. Lewis, and M. J. Barnsley, "Modis brdf/albedo product: algorithm theoretical basis document version 5.0," *MODIS documentation* **23**(4), pp. 42–47, 1999.
- [49] "semrock." <https://www.semrock.com/filter-spectra-at-non-normal-angles-of-incidence.aspx>. Accessed: July 2017.
- [50] D. P. Roy, M. Wulder, T. Loveland, C. Woodcock, R. Allen, M. Anderson, D. Helder, J. Irons, D. Johnson, R. Kennedy, *et al.*, "Landsat-8: Science and product vision for terrestrial global change research," *Remote Sensing of Environment* **145**, pp. 154–172, 2014.
- [51] J. Friedman, T. Hastie, and R. Tibshirani, *The elements of statistical learning*, vol. 1, Springer series in statistics New York, 2001.
- [52] M. A. Friedl and C. E. Brodley, "Decision tree classification of land cover from remotely sensed data," *Remote sensing of environment* **61**(3), pp. 399–409, 1997.
- [53] J. R. Quinlan, *C4. 5: programs for machine learning*, Elsevier, 2014.
- [54] P. Bajorski, *Statistics for imaging, optics, and photonics*, vol. 808, John Wiley & Sons, 2011.
- [55] S. Ganguly, R. R. Nemani, G. Zhang, H. Hashimoto, C. Milesi, A. Michaelis, W. Wang, P. Votava, A. Samanta, F. Melton, *et al.*, "Generating global leaf area index from landsat: Algorithm formulation and demonstration," *Remote Sensing of Environment* **122**, pp. 185–202, 2012.
- [56] F. Baret and S. Buis, "Estimating canopy characteristics from remote sensing observations. review of methods and associated problems," *Advances in land remote sensing: System, modeling, inversion and application*, pp. 173–201, 2008.

- 
- [57] C. Wu, L. Wang, Z. Niu, S. Gao, and M. Wu, "Nondestructive estimation of canopy chlorophyll content using hyperion and landsat/tm images," *International Journal of Remote Sensing* **31**(8), pp. 2159–2167, 2010.
- [58] H. Fang, S. Liang, and A. Kuusk, "Retrieving leaf area index using a genetic algorithm with a canopy radiative transfer model," *Remote sensing of environment* **85**(3), pp. 257–270, 2003.
- [59] C. Walthall, W. Dulaney, M. Anderson, J. Norman, H. Fang, and S. Liang, "A comparison of empirical and neural network approaches for estimating corn and soybean leaf area index from landsat etm+ imagery," *Remote Sensing of Environment* **92**(4), pp. 465–474, 2004.
- [60] M. González-Sanpedro, T. Le Toan, J. Moreno, L. Kergoat, and E. Rubio, "Seasonal variations of leaf area index of agricultural fields retrieved from landsat data," *Remote Sensing of Environment* **112**(3), pp. 810–824, 2008.
- [61] S. S. Durbha, R. L. King, and N. H. Younan, "Support vector machines regression for retrieval of leaf area index from multiangle imaging spectroradiometer," *Remote Sensing of Environment* **107**(1), pp. 348–361, 2007.
- [62] V. Vapnik, *Statistical learning theory*. 1998, Wiley, New York, 1998.
- [63] "dirsig." <http://dirsig.org/>. Accessed: July 2017.
- [64] E. J. Ientilucci and S. D. Brown, "Advances in wide area hyperspectral image simulation," in *Proc. of SPIE Vol*, **5075**, p. 111, 2003.
- [65] P. Romanczyk, *Extraction of Vegetation Biophysical Structure from Small-Footprint Full-Waveform Lidar Signals*, Rochester Institute of Technology, 2015.
- [66] A. Berk, L. S. Bernstein, and D. C. Robertson, "Modtran: A moderate resolution model for lowtran," tech. rep., SPECTRAL SCIENCES INC BURLINGTON MA, 1987.

- 
- [67] Z. Cui, J. Kerekes, and J. Schott, "Validation of landsat-8 oli image simulation," in *Geoscience and Remote Sensing Symposium (IGARSS), 2017 IEEE International*, **0**, pp. 3186–3189, 2017.
- [68] K. Bloechl, C. De Angelis, M. Gartley, J. Kerekes, and C. E. Nance, "A comparison of real and simulated airborne multisensor imagery," in *Algorithms and Technologies for Multispectral, Hyperspectral, and Ultraspectral Imagery XX*, **9088**, p. 90880G, International Society for Optics and Photonics, 2014.
- [69] Z. Cui, J. Kerekes, C. DeAngelis, S. Brown, and C. Nance, "A comparison of real and simulated airborne hyperspectral imagery," in *2014 IEEE Western New York Image and Signal Processing Workshop (WNYISPW)*, pp. 19–22, IEEE, 2014.
- [70] S. Jacquemoud, W. Verhoef, F. Baret, C. Bacour, P. J. Zarco-Tejada, G. P. Asner, C. François, and S. L. Ustin, "Prospect+ sail models: A review of use for vegetation characterization," *Remote sensing of environment* **113**, pp. S56–S66, 2009.
- [71] W. Verhoef and H. Bach, "Coupled soil-leaf-canopy and atmosphere radiative transfer modeling to simulate hyperspectral multi-angular surface reflectance and toa radiance data," *Remote Sensing of Environment* **109**(2), pp. 166–182, 2007.
- [72] S. Jacquemoud, F. Baret, B. Andrieu, F. Danson, and K. Jaggard, "Extraction of vegetation biophysical parameters by inversion of the prospect+ sail models on sugar beet canopy reflectance data. application to tm and aviris sensors," *Remote sensing of environment* **52**(3), pp. 163–172, 1995.
- [73] J.-B. Feret, C. François, G. P. Asner, A. A. Gitelson, R. E. Martin, L. P. Bidel, S. L. Ustin, G. Le Maire, and S. Jacquemoud, "Prospect-4 and 5: Advances in the leaf optical properties model separating photosynthetic pigments," *Remote sensing of environment* **112**(6), pp. 3030–3043, 2008.
- [74] D. C. Montgomery, *Design and analysis of experiments*, John Wiley & Sons, 2017.

- 
- [75] R. J. Boain, "Ab-cs of sun-synchronous orbit mission design," 2004.
- [76] A. Baldridge, S. Hook, C. Grove, and G. Rivera, "The aster spectral library version 2.0," *Remote Sensing of Environment* **113**(4), pp. 711–715, 2009.
- [77] "land processes distributed active archive center, united states geological survey." [https://lpdaac.usgs.gov/dataset\\_discovery/modis/modis\\_products\\_table/mcd43a1](https://lpdaac.usgs.gov/dataset_discovery/modis/modis_products_table/mcd43a1). Accessed: July 2017.
- [78] J. P. Kerekes and D. A. Landgrebe, "Simulation of optical remote sensing systems," *IEEE Transactions on Geoscience and Remote Sensing* **27**(6), pp. 762–771, 1989.
- [79] N. G. S. F. Center, "Ldcm science and mission requirements document," tech. rep., NASA, 2013.
- [80] A. A. Goodenough and S. D. Brown, "Development of land surface reflectance models based on multiscale simulation," in *SPIE Defense+ Security*, pp. 94720D–94720D, International Society for Optics and Photonics, 2015.
- [81] Z. Cui and J. P. Kerekes, "Impact of wavelength shift in relative spectral response at high angles of incidence in landsat-8 operational land imager and future landsat design concepts," *IEEE Transactions on Geoscience and Remote Sensing* (99), pp. 1–11, 2018.
- [82] E. Vermote, C. Justice, M. Claverie, and B. Franch, "Preliminary analysis of the performance of the landsat 8/oli land surface reflectance product," *Remote Sensing of Environment* **185**, pp. 46–56, 2016.
- [83] R. Darvishzadeh, A. A. Matkan, and A. D. Ahangar, "Inversion of a radiative transfer model for estimation of rice canopy chlorophyll content using a lookup-table approach," *IEEE Journal of selected topics in applied earth observations and remote sensing* **5**(4), pp. 1222–1230, 2012.

- 
- [84] C.-W. Hsu, C.-C. Chang, C.-J. Lin, *et al.*, "A practical guide to support vector classification," 2003.
- [85] A. A. Abuelgasim, S. Gopal, J. R. Irons, and A. H. Strahler, "Classification of asms multiangle and multispectral measurements using artificial neural networks," *Remote Sensing of Environment* **57**(2), pp. 79–87, 1996.
- [86] A. Mahtab, V. Sridhar, and R. R. Naval Gund, "Impact of surface anisotropy on classification accuracy of selected vegetation classes: An evaluation using multitemporal multiangular misr data over parts of madhya pradesh, india," *IEEE Transactions on Geoscience and Remote Sensing* **46**(1), pp. 250–258, 2008.
- [87] E. C. B. de Colstoun and C. L. Walthall, "Improving global scale land cover classifications with multi-directional polder data and a decision tree classifier," *Remote Sensing of Environment* **100**(4), pp. 474–485, 2006.
- [88] W. A. Dorigo, "Improving the robustness of cotton status characterisation by radiative transfer model inversion of multi-angular chris/proba data," *IEEE Journal of Selected Topics in Applied Earth Observations and Remote Sensing* **5**(1), pp. 18–29, 2012.
- [89] J. Moreno, L. Alonso, G. Fernández, J. Fortea, S. Gandía, L. Guanter, J. García, J. Martí, J. Melia, F. De Coca, *et al.*, "The spectra barrax campaign (sparc): Overview and first results from chris data," *European Space Agency, (Special Publication) ESA SP* (578), pp. 30–39, 2004.
- [90] J. Delegido, J. Verrelst, C. Meza, J. Rivera, L. Alonso, and J. Moreno, "A red-edge spectral index for remote sensing estimation of green lai over agroecosystems," *European Journal of Agronomy* **46**, pp. 42–52, 2013.
- [91] J. Verrelst, J. P. Rivera, F. Veroustraete, J. Muñoz-Marí, J. G. Clevers, G. Camps-Valls, and J. Moreno, "Experimental sentinel-2 lai estimation using parametric,

- non-parametric and physical retrieval methods—a comparison,” *ISPRS Journal of Photogrammetry and Remote Sensing* **108**, pp. 260–272, 2015.
- [92] T. Cocks, R. Jenssen, A. Stewart, I. Wilson, and T. Shields, “The hymaptm airborne hyperspectral sensor: The system, calibration and performance,” in *Proceedings of the 1st EARSeL workshop on Imaging Spectroscopy*, pp. 37–42, EARSeL, 1998.
- [93] J. Delegido, J. Verrelst, J. P. Rivera, A. Ruiz-Verdú, and J. Moreno, “Brown and green lai mapping through spectral indices,” *International Journal of Applied Earth Observation and Geoinformation* **35**, pp. 350–358, 2015.
- [94] D. Zhao, L. Huang, J. Li, and J. Qi, “A comparative analysis of broadband and narrowband derived vegetation indices in predicting lai and ccd of a cotton canopy,” *ISPRS Journal of Photogrammetry and Remote Sensing* **62**(1), pp. 25–33, 2007.
- [95] R. Darvishzadeh, C. Atzberger, A. Skidmore, and M. Schlerf, “Mapping grassland leaf area index with airborne hyperspectral imagery: A comparison study of statistical approaches and inversion of radiative transfer models,” *ISPRS Journal of Photogrammetry and Remote Sensing* **66**(6), pp. 894–906, 2011.
- [96] A. A. Gitelson, A. Vina, V. Ciganda, D. C. Rundquist, and T. J. Arkebauer, “Remote estimation of canopy chlorophyll content in crops,” *Geophysical Research Letters* **32**(8), 2005.
- [97] J. G. Clevers and A. A. Gitelson, “Remote estimation of crop and grass chlorophyll and nitrogen content using red-edge bands on sentinel-2 and-3,” *International Journal of Applied Earth Observation and Geoinformation* **23**, pp. 344–351, 2013.
- [98] J. Verrelst, E. Romijn, and L. Kooistra, “Mapping vegetation density in a heterogeneous river floodplain ecosystem using pointable chris/proba data,” *Remote Sensing* **4**(9), pp. 2866–2889, 2012.



- [99] W.J. Frampton, J. Dash, G. Watmough, and E. J. Milton, "Evaluating the capabilities of sentinel-2 for quantitative estimation of biophysical variables in vegetation," *ISPRS journal of photogrammetry and remote sensing* **82**, pp. 83–92, 2013.
- [100] C. Delloye, M. Weiss, and P. Defourny, "Retrieval of the canopy chlorophyll content from sentinel-2 spectral bands to estimate nitrogen uptake in intensive winter wheat cropping systems," *Remote Sensing of Environment* **216**, pp. 245–261, 2018.
- [101] Z. Cui and J. Kerekes, "Potential of red edge spectral bands in future landsat satellites on agroecosystem canopy green leaf area index retrieval," *Remote Sensing* **10**(9), p. 1458, 2018.
- [102] P. Teillet, B. Markham, and R. R. Irish, "Landsat cross-calibration based on near simultaneous imaging of common ground targets," *Remote sensing of environment* **102**(3), pp. 264–270, 2006.